

1-1-1982

# Laser induced hydroxyl radical fluorescence at atmospheric pressure

Cornelius Yuk-kwan Chan  
*Portland State University*

Follow this and additional works at: [https://pdxscholar.library.pdx.edu/open\\_access\\_etds](https://pdxscholar.library.pdx.edu/open_access_etds)

**Let us know how access to this document benefits you.**

---

## Recommended Citation

Chan, Cornelius Yuk-kwan, "Laser induced hydroxyl radical fluorescence at atmospheric pressure" (1982).  
*Dissertations and Theses*. Paper 69.  
<https://doi.org/10.15760/etd.69>

This Dissertation is brought to you for free and open access. It has been accepted for inclusion in Dissertations and Theses by an authorized administrator of PDXScholar. Please contact us if we can make this document more accessible: [pdxscholar@pdx.edu](mailto:pdxscholar@pdx.edu).

LASER INDUCED HYDROXYL RADICAL FLUORESCENCE  
AT ATMOSPHERIC PRESSURE

by  
CORNELIUS YUK-KWAN CHAN

A dissertation submitted in partial fulfillment of the  
requirements for the degree of

DOCTOR OF PHILOSOPHY  
in  
ENVIRONMENTAL SCIENCES AND RESOURCES-CHEMISTRY

Portland State University

1982

AN ABSTRACT OF THE DISSERTATION OF Cornelius Yuk-kwan Chan  
for the Doctor of Philosophy in Environmental Sciences  
and Resources presented November 9, 1982.

Title: Laser Induced Hydroxyl Radical Fluorescence  
at Atmospheric Pressure

APPROVED BY MEMBERS OF THE DISSERTATION COMMITTEE:

  
Robert J. O'Brien, Chairman

  
Carole R. Gatz

  
David K. Roe

  
Stanley S. Hillman

  
Raymond W. Sommerfeldt

  
William W. Paudler

Laser Induced Fluorescence (LIF) is one of the chief  
methods for detecting ambient hydroxyl radicals. To  
measure the absolute concentration of this important  
atmospheric chemical species, accurately known quenching

rate constants due to the dominant gases in the air are of paramount importance. Unfortunately, these rate constants have only been measured under conditions remote from those of ambient air. This dissertation reports the measurement of the rate constants of water, argon, nitrogen and oxygen under ambient conditions.

As the LIF is carried out at atmospheric pressure, the OH fluorescence life-time becomes extremely short (about 1 ns). Time Correlated Photon Counting was used to study this short fluorescence phenomenon. The unique feature of this study was that the deactivation processes of the excited OH could be described completely by a kinetic model. Detailed theoretical treatments of the LIF processes are presented. The data obtained are consistent with the accepted model, thereby demonstrating the usefulness and validity of the experimental approach.

The rate constants ( $\text{cc molecule}^{-1} \text{ sec}^{-1}$ ) for quenching by water and argon were accurately measured. The vibrational relaxation rate constant by water ( $3.4 \pm 0.6 \times 10^{-10}$ ) is the first value ever reported, while the electronic quenching rate constants for water ( $k_{Q0} = 7.9 \pm 0.47 \times 10^{-10}$ ,  $k_{Q1} = 1.48 \pm 0.74 \times 10^{-10}$ ) are the first measured at atmospheric pressure. The electronic quenching rate constants of the  $^2\Sigma(v'=1)$  state ( $k_{Q1}$ ) and the  $^2\Sigma(v'=0)$  state ( $k_{Q0}$ ) by argon are  $k_{Q0} = 0.48 \pm 0.14 \times 10^{-12}$  and  $k_{Q1} = 0.24 \pm 0.06 \times 10^{-11}$ . The vibrational relaxation rate

constant by argon is  $k_{10} = 0.34 \pm 0.06 \times 10^{-11}$ . The rate constants for oxygen ( $k_{01} + k_{10} = 1.83 \pm 0.43 \times 10^{-9}$  and  $k_{00} = 2.6 \pm 0.6 \times 10^{-10}$ ) are significantly higher than the limited measurements available at low pressure. The rate constants for nitrogen are  $k_{00} = 0.71 \pm 0.08 \times 10^{-11}$  and  $k_{10} = 8.07 \pm 0.65 \times 10^{-11}$ . All these values are the first obtained at atmospheric pressure and although shown to be consistent with the widely scattered low pressure values, they allow more reliable analysis of ambient OH measurements, and result in a 31.2% increase in the published values.


TO THE OFFICE OF GRADUATE STUDIES AND RESEARCH:

The members of the committee approve the dissertation  
of Cornelius Yuk-kwan Chan presented November 9, 1982.

  
Robert J. O'Brien, Chairman

  
Carole R. Gatz

  
David K. Roe

  
Stanley S. Hillman

  
Raymond W. Sommerfeldt

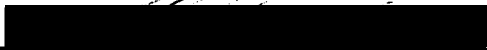
  
William W. Paudler

APPROVED:

  
David W. McClure, Head, Department of Chemistry

  
Robert O. Tinnin, Director, Environmental Sciences and Resources

  
William W. Paudler, Dean, College of Liberal Arts and Sciences

  
Stanley E. Rauch, Dean of Graduate Studies and Research

## ACKNOWLEDGEMENT

Without the help from many, this project would not have been possible. My special gratitude is due to Dr. T.M. Hard for the support out of the grant for OH measurement and my thesis advisor Dr. R.J. O'Brien.

## TABLE OF CONTENTS

	PAGE
ACKNOWLEDGEMENT.....	iii
LIST OF TABLES.....	vi
LIST OF FIGURES.....	ix
CHAPTER	
I BACKGROUND.....	1
Importance of Hydroxyl Radical.....	1
Methods of Detection - LIF.....	2
Rate Constants.....	3
Time Correlated Photon Counting - Principle...	7
Coates Correction and Constant Fraction Discriminator.....	11
Suitability of the Counting Method for OH Measurement.....	15
II THEORY.....	17
The Rate Equations.....	17
The Real Laser Pulse.....	21
Methods of Deconvolution.....	25



	PAGE
A Simulation.....	28
Discrete Convolution.....	35
Minor Details.....	38
III EXPERIMENTAL.....	42
IV RESULTS.....	48
Data.....	48
Analysis of Data.....	69
Final Results and Literature Values.....	80
V ERROR ASSESSMENT.....	98
Systematic and Random Errors.....	98
Convergence Test.....	101
Timing Errors.....	103
VI DISCUSSION.....	114
REFERENCES.....	123
APPENDICES.....	127
A SIMPLEX SEARCH.....	128
B MCA TO AIM 65 INTERFACE.....	136
C LASER POWER MONITOR.....	144

## LIST OF TABLES

TABLE	PAGE
I Rate constants used in the simulation exercise...	29
II Discrete convolution algorithm.....	37
III Experimental results of A's and B's in argon at dew point 19.0C.....	59
IV Experimental results of A's and B's in argon at dew point 16.0C.....	60
V Experimental results of A's and B's in argon at dew point 9.0C.....	60
VI Experimental results of A's and B's in argon at dew point 4.0C.....	61
VII Experimental results of A's and B's in argon at dew point -7.0C.....	61
VIII Experimental results of A's and B's in argon at dew point -16.0C.....	62
IX Experimental results of A's and B's in nitrogen at dew point -16.0C.....	63
X Experimental results of A's and B's in nitrogen and 2% oxygen at dew point -16.0C.....	63
XI Experimental results of A's and B's in nitrogen and 5% oxygen at dew point -16.0C.....	64

TABLE	PAGE
XII Results of linear least squares fits showing the slopes and intercepts.....	72
XIII Final results and literature values of argon....	81
XIV Final results and literature values of water....	83
XV Final results and literature values of nitrogen.	85
XVI Final results and literature values of oxygen...	87
XVII Effects of channel resolution on the accuracy of equation 26.....	100
XVIII Effects of signal/noise ratio on the accuracy of equation 26.....	100
XIX Errors due to 0.3 ns shift of the laser profile.	113
XX Effects on A and B by the spurious fluorescence signals of various amplitudes.....	121
XXI Simplex program with the convolution subroutine.	133
XXII Logic sequences for executing commands to control the MCA through the interface adaptor by the AIM-65.....	138
XXIII Assembly codes for executing the commands to control the MCA.....	139
XXIV Commands for controlling the MCA in BASIC statements.....	142
XXV Memory map of the copied MCA contents.....	143

## TABLE

## PAGE

XXVI Assembly codes for the laser power monitor.....	148
--	-----

## LIST OF FIGURES

FIGURE	PAGE
1 Model representing the energy transfers of excited hydroxyl radical (OH).....	4
2 Principle of time correlated photon counting.....	9
3 Schematics of time correlated photon counting experimental setup.....	10
4 Errors due to difference in pulse heights.....	14
5 Derivation of the convolution - A.....	22
6 Derivation of the convolution - B.....	23
7 Input function, $f(t)$ , for the simulation exercise.....	31
8 Simulated fluorescence -- low pressure.....	33
9 Semilog plot of simulated fluorescence at low pressure.....	34
10 Simulated fluorescence -- atmospheric pressure....	36
11 Schematics of experimental setup.....	43
12 OH fluorescence cell.....	44
13 Fluorescence decay of OH in argon plus water (D.P. -16.0C): x-laser profile; .-fluorescence; solid line-least squares fit. Time scale is 0.4 ns per channel.....	49

- 14 Fluorescence decay of OH in argon plus water  
(D.P. -7.0C): x-laser profile; .-fluorescence;  
solid line-least squares fit. Time scale is  
0.4 ns per channel.....50
- 15 Fluorescence decay of OH in argon plus water  
(D.P. 4.0C). Laser profile is not shown.  
Time scale is 0.2 ns per channel.....51
- 16 Fluorescence decay of OH in argon plus water  
(D.P. 9.0C). Time scale is 0.2 ns per channel.....52
- 17 Fluorescence decay of OH in argon plus water  
(D.P. 16.0C). Time scale is 0.1 ns per channel....53
- 18 Fluorescence decay of OH in argon plus water  
(D.P. 19.0C). Time scale is 0.1 ns per channel....54
- 19 Fluorescence decays of OH in argon plus water.  
. - fluorescence at different water  
concentrations. x - laser profile. The graph  
shows the drastic difference in the decay curves  
due to the change in water concentration.....55
- 20 Fluorescence decay of OH in nitrogen  
(D.P. -16.0C). Time scale is 0.2 ns per channel...56
- 21 Fluorescence decay of OH in nitrogen plus 2%  
oxygen. Time scale is 0.1 ns per channel.....57
- 22 Fluorescence decay of OH in nitrogen plus 5%  
oxygen. Time scale is 0.1 ns per channel.....58
- 23 Linear least squares fit of C/AB versus  
cumulative count (x0.1) tabulated in Table XI.....66
- 24 Linear least squares fit to A's and B's  
in argon as a function of water concentration.....70

## FIGURE

## PAGE

25	Linear least squares fit to A's and B's in nitrogen as a function of oxygen concentration....	71
26	Ratio of fluorescence intensity at 309 nm to 314 nm in Helium as a function of water concentration.....	76
27	Plot of $\log(k_{\text{QON}_2}[\text{N}_2])$ against $\log[\text{N}_2]$ .....	91
28	Plot of $\log(k_{\text{QOAr}}[\text{Ar}])$ against $\log[\text{Ar}]$ .....	92
29	Plot of $\log(k_{\text{QOO}_2}[\text{M}])$ against $\log[\text{M}]$ .....	93
30	Plot of $\log(k_{\text{QOH}_2\text{O}}[\text{M}])$ against $\log[\text{M}]$ .....	94
31	Linear least squares fit to the literature values of $k_{\text{QON}_2}[\text{N}_2]$ as a function of experimental pressure.....	96
32	Values of A's and B's as a function of cumulative count in nitrogen/5% oxygen and argon/water at dew point -16.0C.....	102
33	Plot of $\log(\text{error})$ versus $\log(\text{count})$ of the experiment on OH fluorescence in nitrogen.....	104
34	Uncertainty check of the MCA. Time scale is 0.1 ns per channel.....	106
35	Uncertainty check of the high-speed photodiode. Time scale is 0.1 ns per channel.....	107
36	Misalignment of the laser profiles showing the drift of the detection system.....	109
37	Misalignment of the laser profiles showing the rising portions of the profiles.....	110

## FIGURE

## PAGE

38 Plot of the half height times and half-width of the laser profiles as a function of days of operation.....	111
39 Fluorescence of OH in nitrogen due to the excitation by a laser of 10 ns half-width.....	116
40 Spurious OH concentration profile produced by the photolysis of ozone.....	119
41 Flow chart of the simplex iteration procedure.....	132
42 Schematics of the MCA to AIM-65 interface adaptor.....	137
43 Laser power monitor.....	145
44 Schematics of the peak detector.....	146



## CHAPTER I

### BACKGROUND

The purpose of this investigation is to investigate the possibility of studying the high pressure energy transfers of electronically excited hydroxyl radical (OH) with the Time Correlated Photon Counting technique. The history leading to this undertaking will be dealt with in this chapter.

#### Importance of The OH Radical

The importance of the OH radical as a key intermediate in a wide variety of chemical, atmospheric and astrophysical systems has been appreciated for many years and accounts, in part, for numerous undertakings to characterize its fundamental physical properties. However, the long-standing interest in OH, as pointed out by Lengel and Crosley(1), is the attempt of a basic understanding of a small molecule theoretically tractable. As in spectroscopy, the interest is due to the challenge of developing model Hamiltonians, which can accurately represent the experimental rotational-vibrational structures(2). The kinetic interest is mainly on the energy transfers involving the electronically excited OH, especially the  $A^2\Sigma$  states produced by photodecomposition

of water as typified by the studies of Carrington(3), Kondrat'ev(4), Bunnett et al.(5) and Hooymayers et al.(6).

The reason for this undertaking, besides the kinetics interest, stems from the attempts to measure ambient OH concentration by Laser Induced Fluorescence (LIF) (7,8). The OH radical itself has attracted considerable attention from atmospheric chemists (Crutzen(9), Levy(10), Wofsy et al.(11), Chameides et al.(12) and Davis et al.(8)). The major roles of the OH radical in tropospheric chemistry have been summarized by Logan et al.(13).

#### Methods of Detecting OH

Due to the crucial importance of OH to our understanding of the chemistry in the atmosphere, many attempts have been made to measure the ambient OH concentration. Anderson used a molecular resonance method to measure the OH in the upper atmosphere(14). Burnett measured the OH concentration by monitoring the absorption of sunlight by terrestrial OH(15). Perner et al. used long path absorption (7.8 km) at 309.995 nm to monitor OH concentration(16). Campbell et al. utilized radioactive carbon monoxide as a tracer to measure ambient OH concentration(17). The LIF method promoted by Baardsen and Terhune(18), Wang et al.(19) and Davis et al.(20) is central to this dissertation.

The LIF technique involves exciting the OH radical

using one of the rotational-vibronic lines in the  ${}^2\Pi(v''=0) \rightarrow {}^2\Sigma(v'=1)$  transitions and observing the fluorescence emission associated with the  ${}^2\Sigma(v'=1) \rightarrow {}^2\Pi(v''=1)$  transition near 314.5 nm or the  ${}^2\Sigma(v'=0) \rightarrow {}^2\Pi(v''=0)$  transition near 309.0 nm. The processes involved are pictured in Figure 1. The k's in the Figure are the second order rate constants associated with the various energy transfers. These processes will be described in detail in chapter II.

#### The Importance of OH Quenching and Relaxation Rate Constants

Generally, the LIF method requires a calibration standard. The resulting fluorescence signal of the sample of interest has to be matched against the fluorescence intensity of a known OH source subjected to the same irradiance and same conditions in order to deduce the absolute OH concentration of the unknown sample.

According to the method used by Davis et al.(20), the calibration correlates the fluorescence signal and the absolute OH concentration via a cell containing a known amount of OH produced by 184.9 nm photolysis of a water, nitrogen and hydrogen mixture. However, when the medium is changed, the fluorescence efficiency of the OH is also changed. Hence, as indicated by the investigators, the known values of  $k_{O_2}/k_{N_2}$  and  $k_{H_2O}/k_{O_2}$  are essential to the calculation of the absolute OH concentration. Here,  $k_{O_2}$ ,

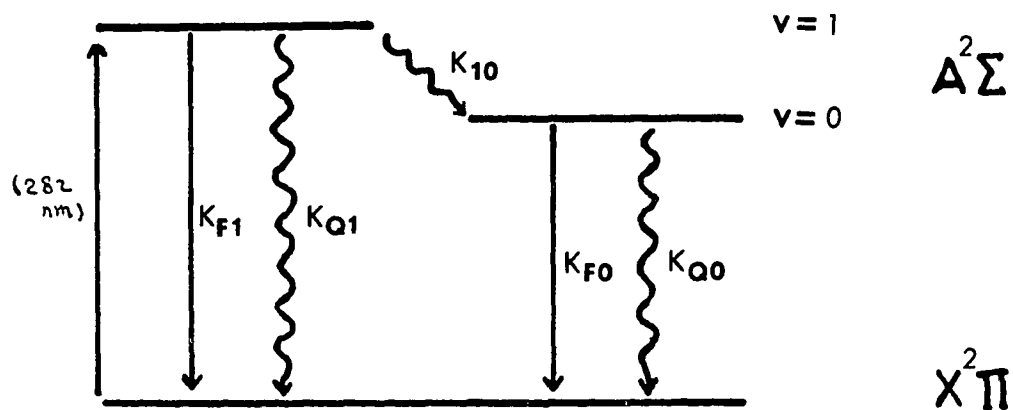


Figure 1 Model representing the energy transfers of excited hydroxyl radical (OH).

$k_{N_2}$  and  $k_{H_2O}$  are the electronic quenching rate constants of oxygen, nitrogen, and water respectively.

The other method of calibration as applied by Wang et al.(19) abandons the known source of OH all together, and relies on the intrinsic physical constants such as the absorption cross section of OH and the quenching and relaxation rate constants of nitrogen, oxygen and water. The investigators calculate the absolute OH concentration using the laser intensity (via nitrogen Raman scattering), the absorption coefficient and the fluorescence efficiency calculated from various rate constants.

As pointed out by Wang et al.(22), the values of fluorescence efficiency (i.e. various rate constants) were scattered over an order of magnitude. Although efforts were made to narrow the range of uncertainty, according to their report, the errors were still in the range of 15% to 20%. In fact, their later result on the ratio of  $k_{H_2O}$  to  $k_{N_2}$  (10:1 at low pressure) contradicted their own earlier result (44:1; measured by relative fluorescence intensity as a function of water concentration in nitrogen at atmospheric pressure).

According to the review by Schofield(24), the  $A^2\Sigma$  states are the most important and best characterized of the electronically excited states of OH and give rise to the strong  $A^2\Sigma \rightarrow X^2\Pi$  allowed transitions. This fact has been used by the LIF method. The review article tabulates

most of the measured electronic quenching, vibrational relaxation and rotational transfer rate constants. However, these reported values are mostly obtained from experiments carried out either at low pressure or at flame temperature, quite different from LIF measurements carried out under ambient conditions.

The reason that most of the earlier experiments are not carried out under ambient conditions has to do with the intention of the experiments and the experimental methods. For example, the usual way of producing high concentrations of OH is by the fast reaction of  $\text{H} + \text{NO}_2$  to produce OH and NO. However, the H atoms are produced by a microwave discharge which has to be operated at low pressure. As a consequence, most of these measurements are made at low pressure. At high pressure (about one atmosphere), the fluorescence life-time is too short and the signal is too weak to be measured with ordinary instruments.

This undertaking is designed to overcome the difficulties of short fluorescence life-time and weak fluorescence signals. It is the first attempt to measure the fluorescence decay of OH  $\text{A}^2\Sigma$  states at atmospheric pressure directly. The excitation scheme duplicates that of the actual LIF used by Wang et al. and Davis et al., that is, to excite OH at 282 nm and to monitor the fluorescence at 309 nm.

### Principle of Time Correlated Photon Counting

In the time correlated photon counting technique(25), the sample under investigation is repetitively excited with short pulses of light and the resulting fluorescence pulses are detected with a photomultiplier tube (PMT). In contrast to the ordinary method of light detection, the fluorescence signal is highly attenuated with an aperture before reaching the PMT. The light attenuation is adjusted so that the probability of detecting a photoelectron per fluorescence pulse is much less than one. Under this condition of low photoelectron arrival rate, a small number of excitation pulses produce one PMT pulse and a still smaller number of excitation pulses produce two or more pulses. For sufficiently high attenuation, each excitation pulse essentially produces zero or one PMT pulse. The detection system is then in the single photon mode. In this mode, the probability that a photoelectron is detected by the PMT at the time,  $t$ , after the firing of an excitation pulse is proportional to the fluorescence intensity at the same time,  $t$ . After many excitation pulses, a plot of the number of counts which arrive in time interval  $t$  and  $t+\Delta t$  versus time gives the time-intensity profile of the fluorescence or scattering pulses.

Two pieces of equipment are fundamental to the implementation of this kind of counting: a

Time-to-Amplitude Converter (TAC) and a Multichannel Pulse Height Analyser (MCA). The excitation light source (a laser pulse in some cases) triggers a high-speed photodiode which in turn starts the TAC. The photoelectron pulse from the PMT triggers the Constant Fraction Discriminator which then stops the TAC. The TAC produces a pulse of amplitude proportional to the length of time between the start and stop pulses. The MCA measures the amplitude of the TAC output and adds a count to the corresponding channel. If no PMT pulse is detected, the TAC automatically stops without producing an output to the MCA. In any event, the TAC resets itself after several microseconds and awaits a new start pulse. After many laser pulses, a plot of counts versus channel number gives the time-intensity profile of the fluorescence or scattering pulses. The relation between channel numbers and time is established with calibrated delay lines or is factory calibrated. Figures 2 and 3 illustrate the principle.

Time correlated photon counting has been applied to nanosecond fluorescence measurements since the mid-1960's(26). Since that time there have been significant improvements in both the electronic measuring instruments and the excitation light sources. The traditional light sources have been gaseous gap-discharge arcs. Now high repetition laser sources, especially



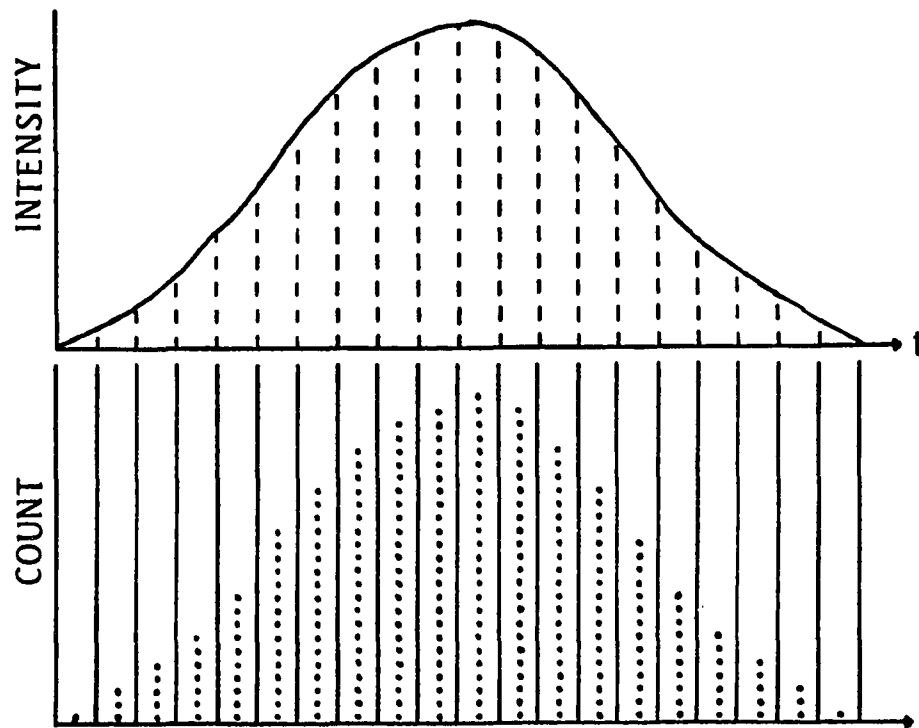


Figure 2 Principle of time correlated photon counting. The upper curve shows the intensity profile divided into time slots. The lower curve shows the distribution of counts which resembles the intensity profile.

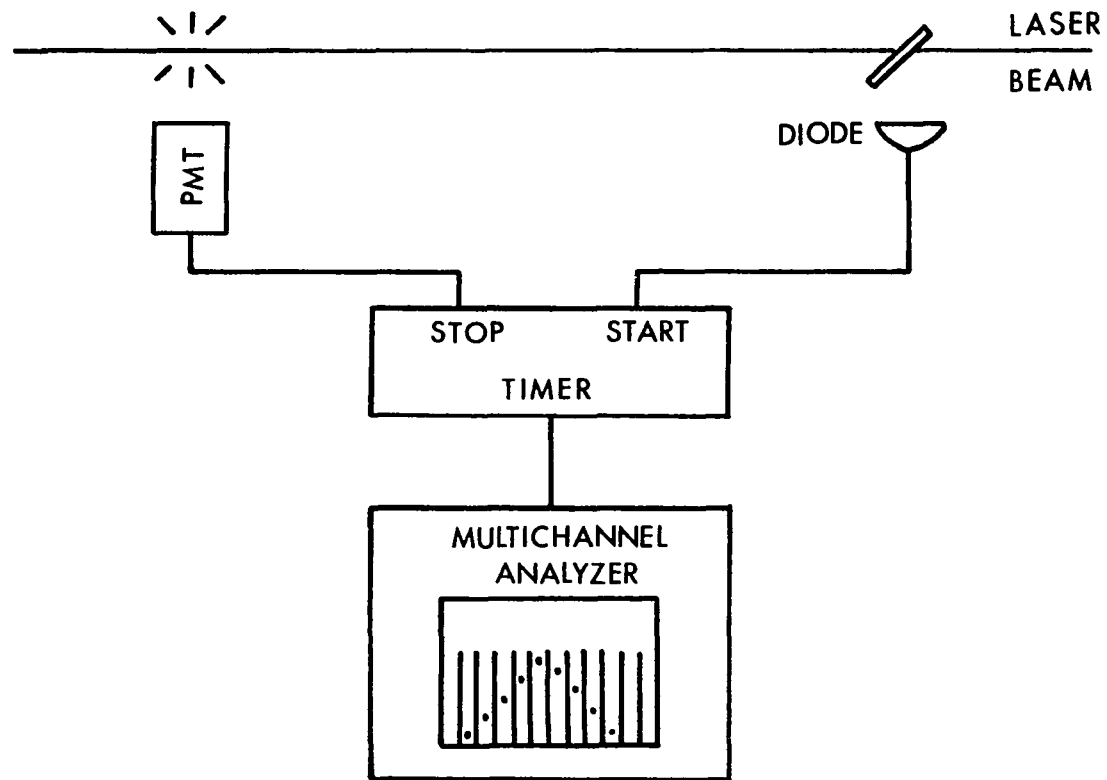


Figure 3 Schematics of time correlated photon counting experimental setup.

tunable dye lasers, have almost replaced the gaseous-discharge arcs(26). The advantages of lasers over the discharge arcs were outlined by Koester(26) as:

1. Capable of very short ( $<35$  ps) excitation pulses.
2. High excitation pulse power.
3. Capable of high repetition rate.
4. Comparatively constant pulse profile over short and long time ranges.
5. Monochromatic and polarized source.
6. Tunable excitation wavelength.

The advances in microcircuitry and hybrid circuits allow the detection system, essentially the TAC and the MCA, to be incorporated into a single piece of equipment. One example is the LeCroy QVT3001 which incorporates many functions into a single double width NIM module. The LeCroy QVT3001 operates on a slightly different principle from that of a TAC but its achieved results are the same.

#### Coates Correction and Constant Fraction Discriminator

The time correlated photon counting technique requires that zero or one fluorescence photoelectron per excitation pulse is detected. Statistically there are always a few laser pulses for which more than one photoelectron is generated. The effects of these multiple photon events result from the fact that the TAC and the MCA require several microseconds to process and recycle themselves after a PMT pulse has been detected. During

this time, the recording system is incapable of registering a second PMT pulse. When two or more photoelectrons are detected by the PMT during one excitation, only the first photoelectron is recorded. This causes a loss of count in the later channels and a subsequent distortion of the fluorescence decay curve.

Several methods are available for circumventing this difficulty. One is to run the experiment at such a low intensity ( $<0.02$  count per cycle) that it becomes highly improbable that more than one PMT pulse is produced. Another is the "live timer"(27,28) method in which the circuits begin to process the first PMT pulse, but if another pulse arrives during the processing both the first and second pulses are discarded and the entire cycle is aborted. Therefore only cycles in which only one photoelectron is detected are accepted by the MCA. This electronic solution allows a somewhat higher arrival rate, but it does have an upper limit. The third approach is to deduce a mathematical algorithm which takes the recorded profile and derives the true spectrum of all arrivals. It turned out to be a rather simple statistical problem (29,30). The Coates correction is one such algorithm. Although the Coates correction requires that the actual number of laser pulses be known, this is only a small price to pay for a shorter experimental time.

The PMT pulses are not always of the same height.

This causes uncertainty in the timing of the TAC. The origin of this uncertainty (walk) is demonstrated in Figure 4. The Figure shows two PMT pulses of different heights reaching the discriminator at the same time. The timing error results from the use of the crossing of a certain voltage level as the arrival time of the pulse. This uncertainty can be serious for pulses of large height variation, especially in the case of scintillation counting. However, for single photon counting, the range of pulse heights is comparatively small. Modern PMT have risetimes of the order of 2 nanoseconds. This limits the walks somewhat. The uncertainty can be narrowed down further by a constant fraction discriminator (31).

The constant fraction discriminator does not use a fixed voltage level as the threshold. Instead it takes a fixed fraction of the maximum PMT pulse height as the threshold. This new threshold allows the arrival time to adjust itself to the PMT pulse height. In principle, the voltage rise of a short PMT pulse reaches the threshold earlier, because the threshold of a short pulse is relatively small as compared to a tall pulse. By the same token, the voltage rise of a tall PMT pulse will reach the threshold later, because the threshold is relatively higher. The effect is that the error, "walk", of the arrival time is reduced. For more details, see reference 31.

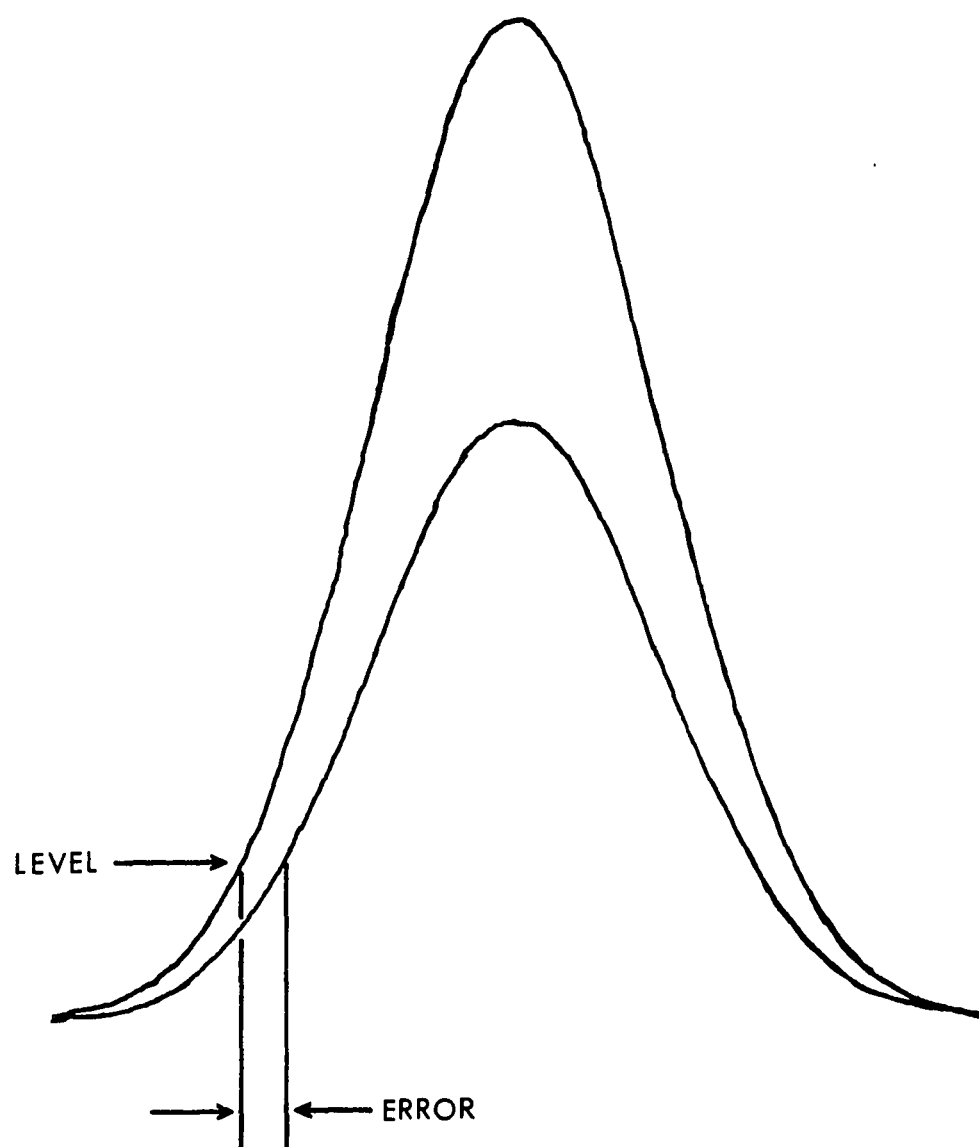


Figure 4 Errors due to difference in pulse heights.

Timing accuracy is not just a problem of the discriminator alone. The instruments down-stream of the constant fraction discriminator are just as crucial in determining the overall uncertainty of the detection system. The TAC, the MCA and the high-speed photodiode combined have an overall uncertainty of about 0.2 ns as compared to the 0.12 ns(32) of the constant fraction discriminator.

#### Suitability of the Method for OH Measurement

The time correlated photon counting method is especially suitable for measuring OH fluorescence decay at atmospheric pressure due to its inherent principle of operation.

The method requires that the photoelectron arrival rate be low. An arrival rate as high as 0.2 per laser pulse is still acceptable provided that the result is corrected by the Coates algorithm. Laser induced OH fluorescence at atmospheric pressure is very weak due to the overwhelmingly fast nonradiative quenching by inert species. This counting technique uses the weak fluorescence signal very well. Other methods such as the Boxcar integrator, which are based on integrated signal, will require very slow scan rate or are unable to separate the background and the signal at all.

Since the method performs well even with a weak fluorescence signal, low OH concentration can still

sustain a good signal to noise ratio for the experiment. In fact, photolysis of water vapor by mercury lamps with quartz jackets produces enough OH to sustain the experiments. This simplifies the experimental setup a lot. No messy and complicated chemical flow systems are needed. This is the advantage that allows the direct measurement of OH fluorescence at atmospheric pressure, because no microwave discharge is required. The experimental setup consists simply of an enclosed cell with a pair of mercury lamps inside and a quartz window for the monochromator to see the fluorescence.

The resolution of the TAC and the MCA can be as short as 0.1 ns per channel over 1000 channels. This means high resolution. In other words, we can get about 100 points for a 10 ns long fluorescence phenomenon. This high resolution is made possible by recent advances in technology.

It is hard to compare the performances of methods such as the transient recorder, the waveform digitizer and other methods relying on integrated signals. Each method has its own advantages under certain circumstances. However, the time correlated photon counting method is clearly and unmistakably suitable for the measurement of OH fluorescence decay at atmospheric pressure.



## CHAPTER II

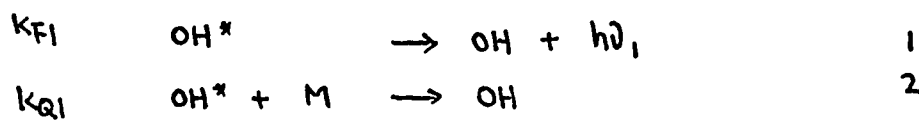
### THEORY

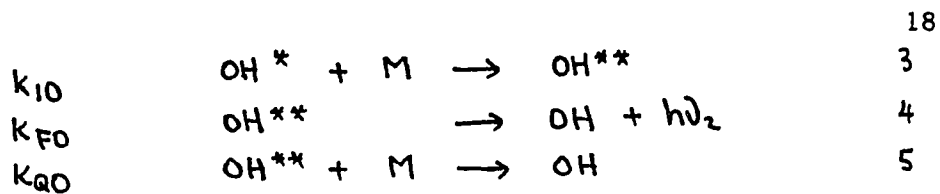
The excitation scheme used by the LIF detection method does not produce a simple exponential fluorescence decay. This chapter will elucidate the processes involved, derive mathematical formulae to describe the processes and establish grounds for experimental strategy.

#### The Rate Equations

The processes involved in the LIF detection scheme are pictured in Figure 1. Since the repopulation of ( $v'=1$ ) states from ( $v'=0$ ) states is not favored,  $k_{01}$  may be ignored without jeopardizing the applicability of the result to the real situation.

The energy transfer processes are represented by equations 1 to 5. Equations 1 and 4 show the spontaneous emissions with natural decay constants  $k_{F1}$  and  $k_{F0}$  of the ( $v'=1$ ) and ( $v'=0$ ) states respectively. Equations 2 and 5 represent non-radiative quenching by inert species M into any states of the lower electronic energy level. Equation 3 is the vibrational relaxation from ( $v'=1$ ) state into ( $v'=0$ ) state through collisions with some inert species M.





We consider excitation of OH radicals by a Dirac delta function or an impulse function at time  $t=0$ . The impulse function can be viewed as a laser pulse with infinitely narrow temporal width. This impulse function produces  $[OH^*]_0$  excited hydroxyl radicals in the upper vibrational state  $A^2\Sigma(v'=1)$ . We denote the number of hydroxyl radicals at a subsequent time  $t$ , in the  $(v'=1)$  state by  $[OH^*]$  and  $(v'=0)$  state by  $[OH^{**}]$ . The rates of change of  $[OH^*]$  and  $[OH^{**}]$  with respect to time are given by

$$\frac{d[OH^*]}{dt} = -k_{F1}[OH^*] - k_{Q1}[OH^*][M] - k_{10}[OH^*][M], \quad 6$$

$$\frac{d[OH^{**}]}{dt} = k_{10}[OH^*][M] - k_{F0}[OH^{**}] - k_{Q0}[OH^{**}][M]. \quad 7$$

Since  $[M]$  can be considered constant as the time progresses, we denote

$$k_{Q1}[M] = k'_{Q1}, \quad 8$$

$$k_{Q0}[M] = k'_{Q0}, \quad 9$$

$$k_{10}[M] = k'_{10}. \quad 10$$

$[M]$  is the pressure at which the experiment is carried out. We do the simplifications:

$$A = k_{F1} + k'_{Q1} + k'_{i0}, \quad 11$$

$$B = k_{F0} + k'_{Q0}. \quad 12$$

The rate expressions become

$$\frac{d[OH^*]}{dt} = -A[OH^*] \quad 13$$

and

$$\frac{d[OH^{**}]}{dt} = k'_{i0}[OH^*] - B[OH^{**}]. \quad 14$$

Equation 13 can be solved readily. Applying the initial condition,  $[OH^*]_0$ , we get

$$[OH^*] = [OH^*]_0 \exp(-At). \quad 15$$

Substituting equation 15 into equation 14, we have

$$\frac{d[OH^{**}]}{dt} + B[OH^{**}] = k'_{i0}[OH^*]_0 \exp(-At). \quad 16$$

Multiplying both sides of equation 16 by  $\exp(Bt)$  and using

$$\left( \frac{d[OH^{**}]}{dt} + B[OH^{**}] \right) \exp(Bt) = \frac{d}{dt}([OH^{**}] \exp(Bt)), \quad 17$$

we have

$$\frac{d}{dt}([OH^{**}] \exp(Bt)) = k'_{i0}[OH^*]_0 \exp[(B-A)t]. \quad 18$$

Integrating and applying the initial condition that  $[OH^{**}] = 0$  at time  $t = 0$ , we have

$$[OH^{**}] = \frac{K'_{10} [OH^*]_0}{B - A} (\exp(-At) - \exp(-Bt)). \quad 19$$

Lengel and Crosley(1) and German(33) arrived at similar equations relating the probability  $P_v(t)$  of a molecule being in a given vibrational state  $v$ . In the notations used by German, the two equations are:

$$P_1(t) = \exp(-t/\tau), \quad 20$$

$$P_0(t) = \frac{n\sigma_{10}V}{\tau_1^{-1} - \tau_0^{-1}} (\exp(-t/\tau_0) - \exp(-t/\tau_1)). \quad 21$$

Where  $\tau_v^{-1}$  is the sum of the decay constants of vibrational state  $v$ . The corresponding equations are exactly the same if we set

$$K'_{10} = n\sigma_{10}V.$$

Finally, equations 15 and 19 are the desired relations. Since they are responses due to impulse functions, we call them impulse response functions. Since they are characteristic of the system (model), we also call them characteristic response functions.

### The Real Laser Pulse

Up to this point, all discussion has been based on the assumption that the laser pulse is an impulse function; it has an infinitely narrow temporal width. In reality, the laser pulse has a finite width. When the decay constant of the impulse response function is small (long life-time) compared to the temporal half-width of the laser pulse, the assumption is valid. However, when the reciprocal of the decay constant and the laser temporal half-width are comparable, the above assumption does not stand. For example, here the half-life of the excited OH radicals at relatively high pressure (one atmosphere) is about one nanosecond and the laser temporal half-width is about 7ns. One definitely will not expect the assumption to hold true.

Since we are considering measurement at atmospheric pressure the assumption can not be of too much help. Nevertheless, equation 19 is our starting point. We consider Figures 5 and 6, where  $I_0 f'(t)$  is the laser time-intensity profile;  $g$  is the response function due to an impulse function;  $h$  is the fluorescence output or the output function due to a laser pulse of finite temporal width. Assuming that Beer's law holds or, in other words, that we are dealing with a linear system, the concentration of the excited OH,  $[OH^*]_{\tau}$  (initial concentration due to an impulse function at time  $\tau$ ), is

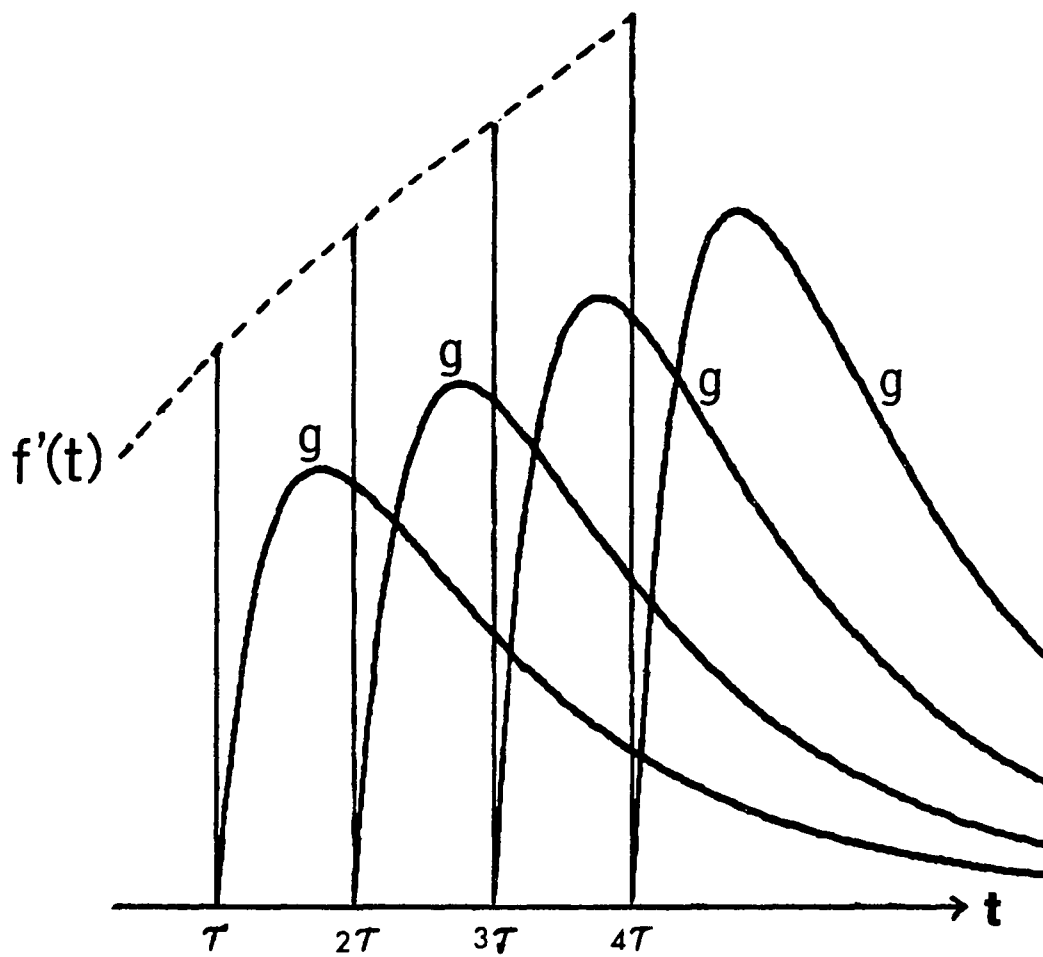


Figure 5 Derivation of the convolution - A.

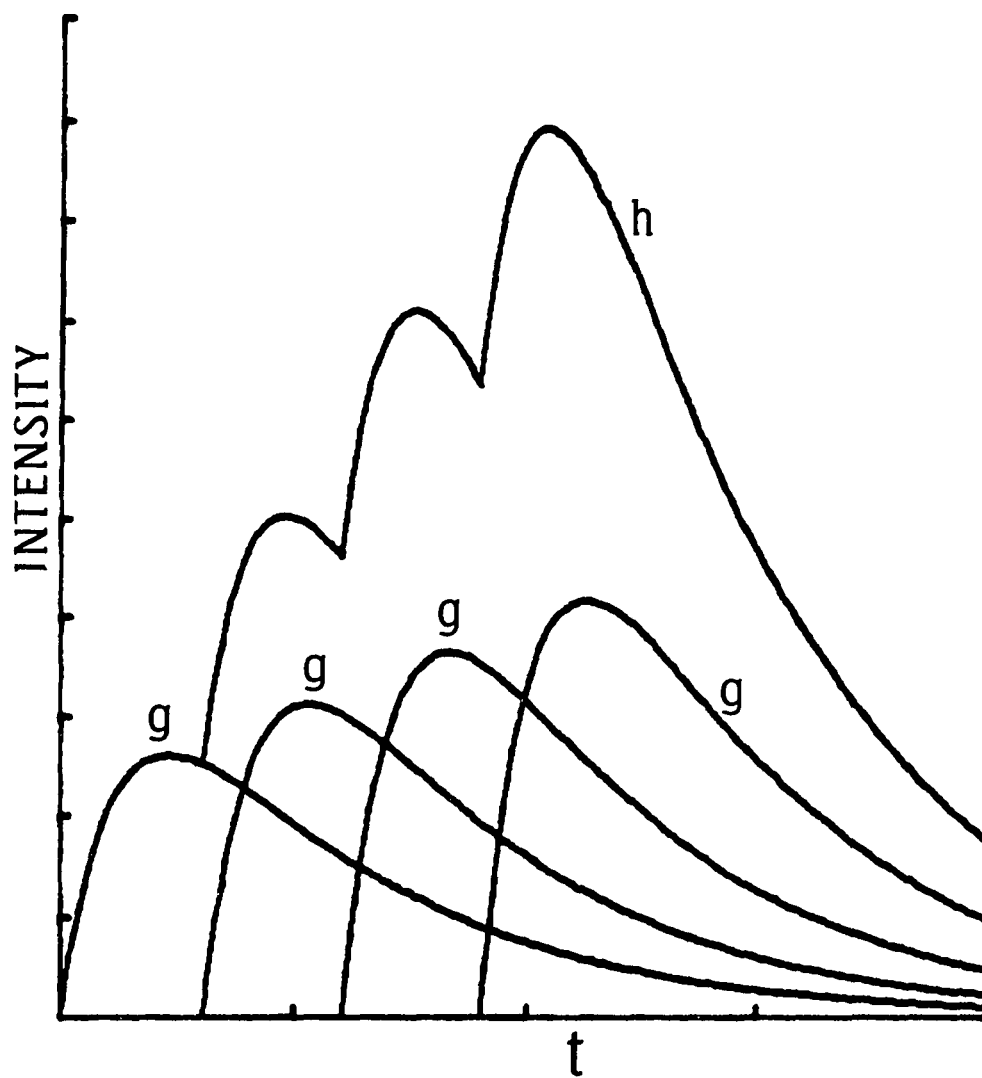


Figure 6 Derivation of the convolution - B.

proportional to the concentration of the ground state OH, [OH], and the laser intensity,  $f(\tau)$ , at time  $\tau$ . We define

$$f(\tau) = I_0 \epsilon [\text{OH}] f'(\tau) = c \cdot f'(\tau). \quad 23$$

Where  $\epsilon$  is the absorption coefficient of OH radical and  $I_0 f'(\tau)$  is the laser flux at time  $\tau$ . Essentially,  $f(\tau)$  is the instantaneous production rate of [OH\*] in molecule  $\text{cc}^{-1} \text{s}^{-1}$ . We call  $f(\tau)$  the input function.

If we view the finite laser pulse as a succession of impulse functions spaced at intervals of  $\tau$ , then the output,  $h(t)$ , due to the impulse function at  $\tau$  is

$$h(t) = f(\tau) g(t - \tau). \quad 24$$

After  $t=2\tau$ , we have

$$h(t) = f(\tau) g(t - \tau) + f(2\tau) g(t - 2\tau). \quad 25$$

Equation 25 has the  $f(\tau) \cdot g(t - \tau)$  term, because after  $2\tau$ , the output is the sum of the response due to the impulse function at  $2\tau$  and whatever remains from the previous response at  $\tau$ . If we proceed in this manner, we get

$$h(t) = \sum_{n=0}^N f(n\tau) g(t - n\tau). \quad 26$$

In the limit as the intervals between successive pulses



approach zero, the summation can be replaced by an integration to become an exact solution:

$$h(t) = \int_0^t f(\tau) g(t-\tau) d\tau. \quad 27$$

Equation 27 is the well known convolution integral. It says that the fluorescence decay one measures, at 309 nm, with a laser pulse of finite width is the convolution of the input function,  $f(t)$ , and the response function,  $g(t)$ . Of course, the response function contains all the relevant rate constants. Although equation 27 is the normal way of denoting convolution, equation 26 provides more insights when we are dealing with real discrete data with a digital computer.

#### Deconvolution Method

In the actual experimental procedure,  $h(t)$  and  $f(t)$  are measured by the time correlated photon counting technique, then  $g(t)$  is extracted according to the relationship shown in equation 26. It is no simple matter to solve for  $g(t)$ , although it has been worked out. Fortunately, the functional form of  $g(t)$  is known in our case. We are more interested in the parameters A and B than the function  $g(t)$  itself. Nevertheless, it is enlightening to see different ways of solving equation 27.

General methods of resolving equation 27 are the method of moments(34,35) and the methods of Fourier and

Laplace transform(36). The method of moments requires that the impulse response function be a simple exponential function or a sum of exponential functions. Fourier and Laplace transforms are not constrained by such requirements.

The method of moments was first used in the study of radioactive decays. Isenberg and Dyson(37) and Schuyler and Isenberg(38) applied the method to multiexponential analysis. The general equations for the method of moments were derived by Bay(34). Suppose that  $g(t)$  is a sum of  $N$  exponentials,

$$g(t) = \sum_{i=1}^N \alpha_i \exp(-\kappa_i t). \quad 28$$

The  $k^{\text{th}}$  moments of  $h(t)$  and  $f(t)$  are defined by the equations:

$$M_k(h) = \int_0^{\infty} t^k h(t) dt ; \quad k=0,1,\dots$$

$$M_k(f) = \int_0^{\infty} t^k f(t) dt ; \quad k=0,1,\dots$$

It can be shown that

$$M_k(h) = \kappa_i \sum_{s=1}^{k+1} \frac{G_s M_{k+1-s}(f)}{k+1-s},$$

where simplification

$$G_s = \sum_{i=1}^N a_i / k_i s$$

is made. These equations allow  $a_i$  and  $k_i$  to be evaluated from the moments of the experimental data, namely  $h(t)$  and  $g(t)$ , by constructing  $2N$  equations.

Laplace and Fourier transforms are very similar, so we group both together as integral transforms. We denote the integral transform of a function  $l(t)$  as  $I\{l(t)\}$ . Then, based on the theorem of integral transform, if  $h(t)$  is the convolution of  $g(t)$  and  $f(t)$ , we have

$$I\{h(t)\} = I\{g(t)\} \cdot I\{f(t)\}. \quad 29$$

The previous expression can be put in a more obvious form,

$$I\{g(t)\} = \frac{I\{h(t)\}}{I\{f(t)\}}. \quad 30$$

Thus, one obtains the transformed form of the response function,  $I\{g(t)\}$ , by dividing the transformed forms of the experimental data,  $I\{f(t)\}$  and  $I\{h(t)\}$ .

The advantage of Fourier transform is the Fast Fourier Transform (FFT) algorithm which saves a

considerable amount of computer time.

In this case, the functional form of  $g(t)$  is known. The interest is in the parameters A and B. The method we will adopt is to use equation 26 directly. The equation will be summed for finite  $\tau$  by a digital computer with A and B that give the lowest least squares errors to the data obtained. The trial and error search for optimum A and B is done using the method of simplex. Appendix A contains details of the simplex method.

#### A Simulation

Simulation was the first step of checking the tenability of the theory before actual experimental work was begun. This kind of exercise provides information on what to expect in the actual experiments and predicts whether or not the results are practically observable. This section describes the simulation of the fluorescence decay of OH in nitrogen atmosphere using the published experimental values of rate constants. Table I shows the rate constants and their corresponding references.

For excitation of OH at the  $v''=0 \rightarrow v'=1$  transitions and detection at 309 nm ( $v'=0 \rightarrow v''=0$  transition) equation 27 becomes

$$h(t) = \int_0^t f'(\tau) \frac{Q}{B-A} (\exp[-A(t-\tau)] - \exp[-B(t-\tau)]) d\tau, \quad 31$$

TABLE I  
RATE CONSTANTS USED IN THE SIMULATION

Rate Constant	Value	Reference
$k_{F1}$	$1.10 \times 10^6 \text{ sec}^{-1}$	39
$k_{F0}$	$1.40 \times 10^6 \text{ sec}^{-1}$	33
$k_{Q1}$	$0.765 \times 10^{-10} \text{ cm}^3 \text{ molecule}^{-1} \text{ sec}^{-1}$	33
$k_{Q0}$	$0.29 \times 10^{-10} \text{ cm}^3 \text{ molecule}^{-1} \text{ sec}^{-1}$	33
$k_{I0}$	$1.61 \times 10^{-10} \text{ cm}^3 \text{ molecule}^{-1} \text{ sec}^{-1}$	33

where we define

$$a = C K_{F0} K'_{10}. \quad 32$$

A and B are the same as defined in equations 11 and 12 while c is defined in equation 23. The laser profile (the input function) is simulated by

$$f(t) = \alpha t^2 \text{Exp}(-\beta t) \quad 33$$

with

$$\alpha = 1.18 \times 10^{18} \text{ photon / cm}^3 \text{s}^3 \quad 34$$

$$\beta = 8.0 \times 10^8 \text{ s}^{-1} \quad 35$$

The term  $\alpha$  is chosen to make  $f(t)=1$  at its maximum. The  $f(t)$  is plotted out in Figure 7. Its half-width is about 6 ns. The output,  $h(t)$ , according to equation 31 is

$$h(t) = \int_0^t \alpha \tau^2 \text{Exp}(-\beta \tau) \frac{a}{B-A} [\text{Exp}(A)(t-\tau) - \text{Exp}(-B)(t-\tau)] d\tau \quad 36$$

or

$$h(t) = \frac{\alpha a}{B-A} [\text{Exp}(-At) \int_0^t \tau^2 \text{Exp}(A-\beta)\tau d\tau - \text{Exp}(-Bt) \int_0^t \tau^2 \text{Exp}(B-\beta)\tau d\tau]. \quad 37$$

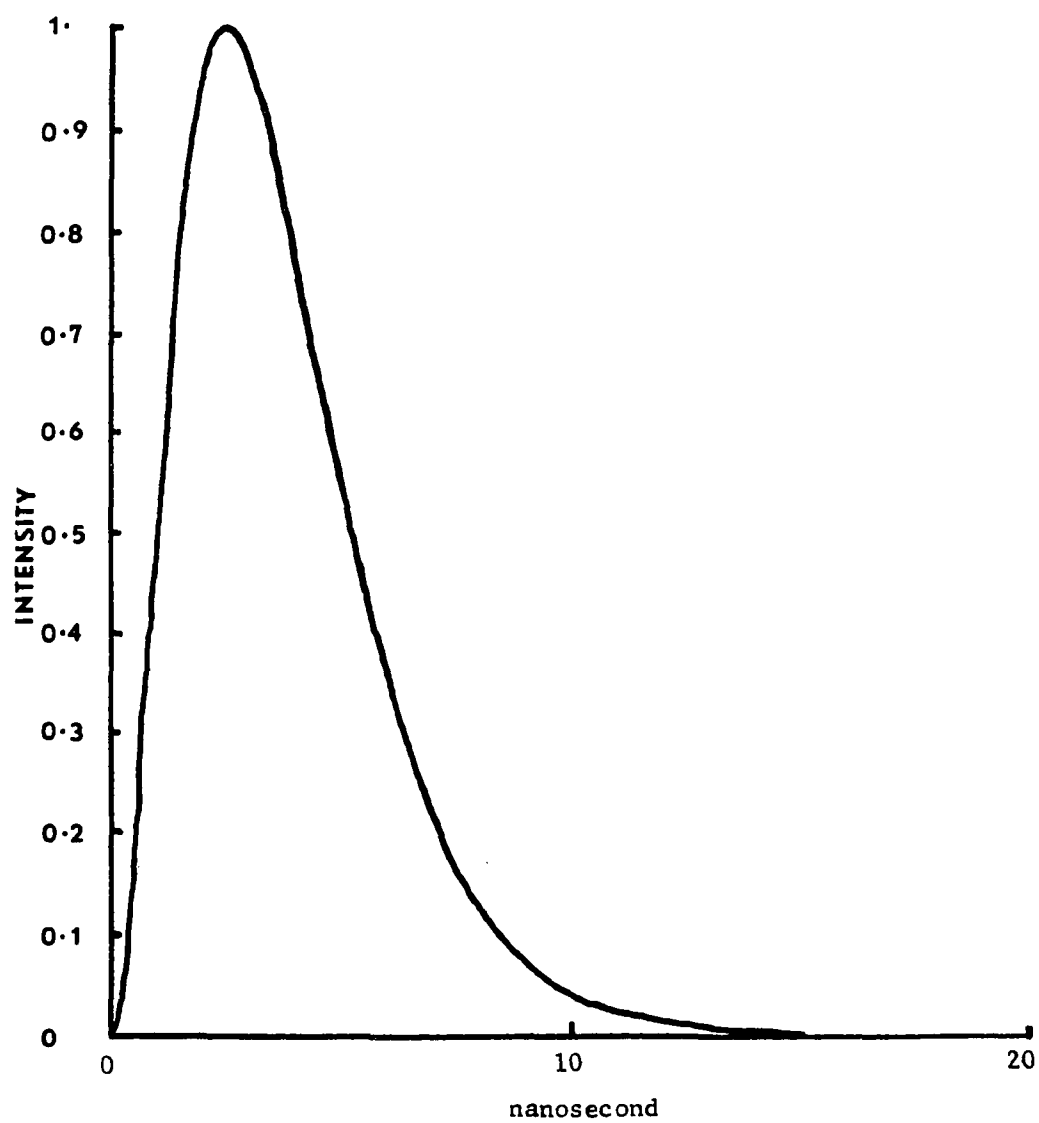


Figure 7    Input function , $f(t)$ , for the simulation exercise.

Integrating, we get

$$P = \frac{\text{EXP}(A-\beta)t}{A-\beta} \left( t^2 - \frac{2t}{A-\beta} + \frac{2}{(A-\beta)^2} \right) - \frac{2}{(A-\beta)^3}, \quad 38$$

$$Q = \frac{\text{EXP}(B-\beta)t}{B-\beta} \left( t^2 - \frac{2t}{B-\beta} + \frac{2}{(B-\beta)^2} \right) - \frac{2}{(B-\beta)^3}, \quad 39$$

$$h(t) = \frac{Q\alpha}{B-A} (P \text{EXP}(-At) - Q \text{EXP}(-Bt)). \quad 40$$

Under a pressure of one torr,  $[M]$  is  $3.32 \times 10^{16}$  molecules/cc. Using values in Table I, we get  $A = 8.99 \times 10^6 \text{ sec}^{-1}$  and  $B = 2.36 \times 10^6 \text{ sec}^{-1}$ . Substituting  $\alpha, \beta, A$  and  $B$  into equations 38, 39 and 40 and plotting out, one gets the graph shown in Figure 8. Figure 9 is a semilog plot of the same result. The slope in Figure 9 results from a linear least squares fit to the tail of the curve. It is equal to  $B$ ! This indicates that when the decay time is long compared to the laser half-width, a simple exponential fit to the tail of the fluorescence curve will give  $B$  as the slope. These two plots have the same general features of the data collected in reference 23. Thus the theory agrees with the experiment data obtained in reference 23 in general terms.

To investigate the feasibility of measuring fluorescence decay at one atmosphere, equations 38, 39 and



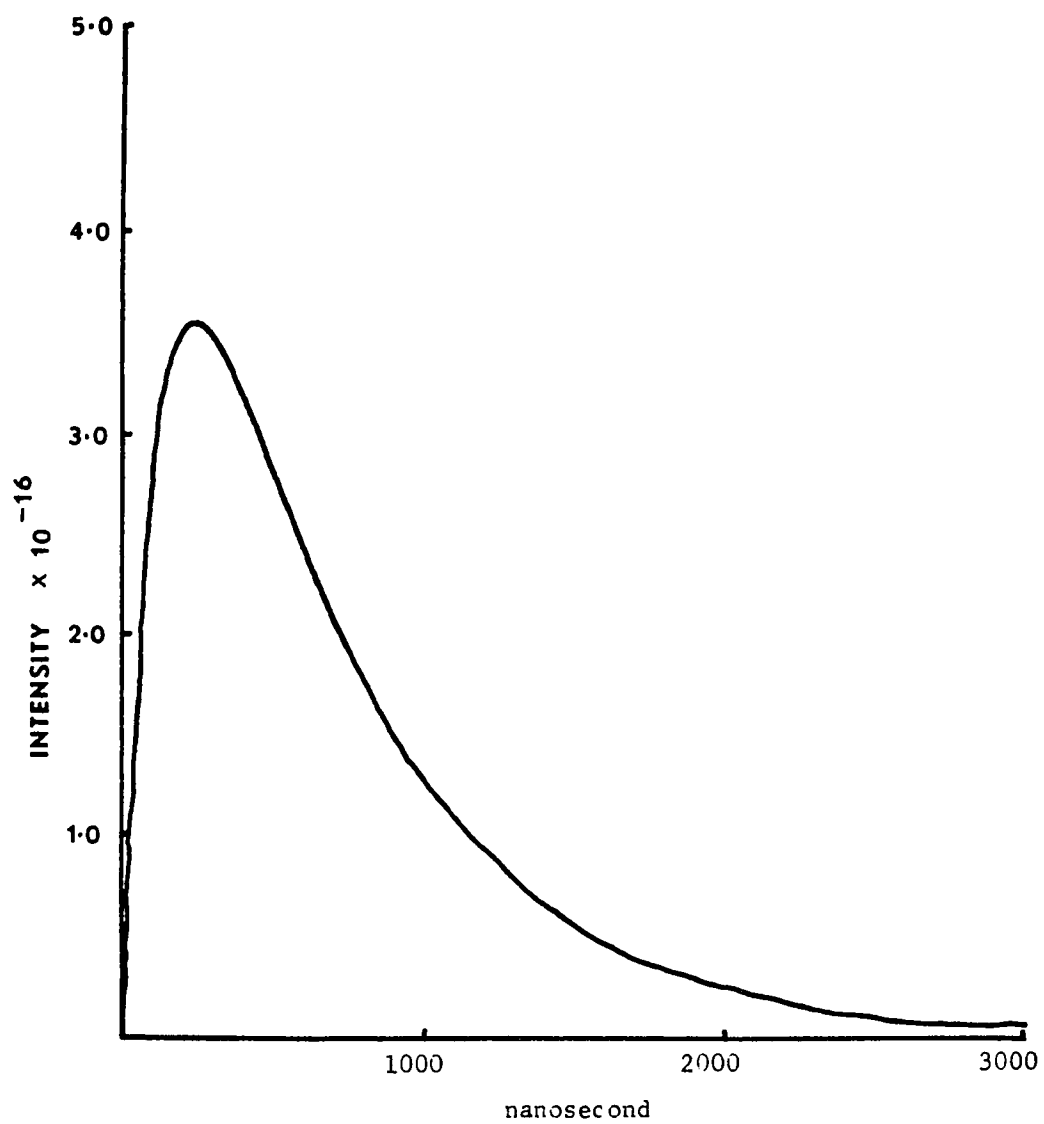


Figure 8 Simulated fluorescence - low pressure.

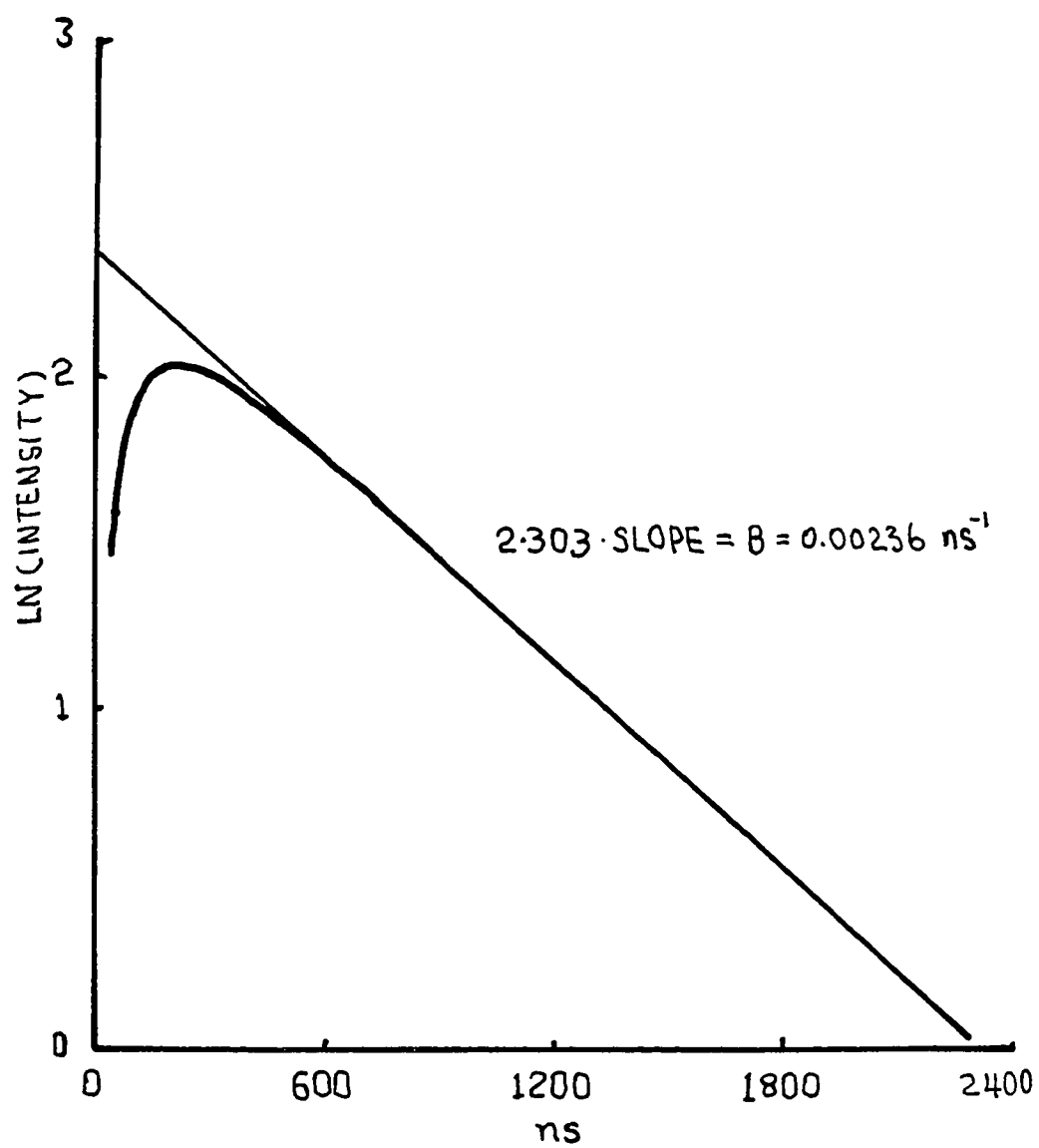


Figure 9 Semilog plot of simulated fluorescence at low pressure.

40 are used again with  $[M]=2.46 \times 10^{19}$  molecules/cc which manifests into  $A=5.78 \times 10^9$  and  $B=7.1 \times 10^8 \text{ sec}^{-1}$ . Substituting in A, B,  $\alpha$  and  $\beta$ , one gets the plot shown in Figure 10. A similar linear least squares fit to the tail of the semilog plot gives a slope much smaller than B. This indicates that in high pressure fluorescence, convolution is required. For comparison purposes, the laser profile is plotted on the same graph. Notice that the output function is slightly broader and displaced a little to the right.

The convolution integral does not impose any limits on how large A and B can be. However, the noise in the actual data determines the practical limits. In general, the narrower the laser temporal half-width, the larger the A and B which can be resolved.

#### Discrete Convolution

Although the convolution integral, equation 27, describes exactly what is going on, this equation has little practical value in our application because the mathematical form of the input function i.e. the laser profile is not known. On the other hand, the discrete form, equation 26, is suitable for implementing on a digital computer. This equation only requires the input function be represented by a set of discrete values. This very same equation is translated into a computer algorithm (in BASIC) shown in Table II. To use this algorithm, the

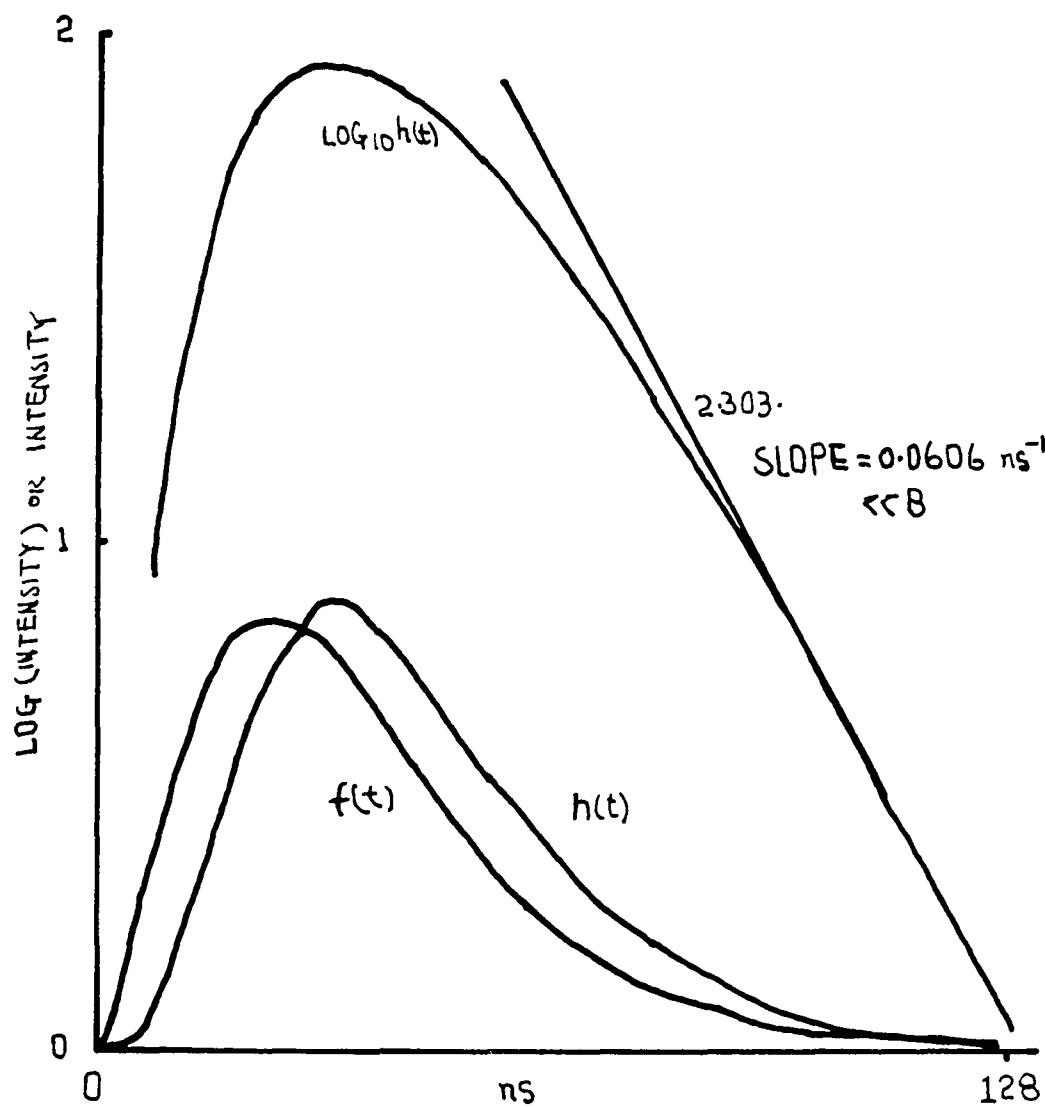


Figure 10 Simulated fluorescence - atmospheric pressure of nitrogen.

TABLE II  
DISCRETE CONVOLUTION ALGORITHM

```
LIST 12380,12620
12380 DIM H(256)
12390 DIM L(256)
12420 H=0
12440 FOR I=1 TO 256
12450     J=I-1
12460     IF J*A*0.1>60 THEN 12500
12470     IF J*B*0.1>60 THEN 12520
12480     L(I)=EXP(-A*J*0.1)-EXP(-B*J*0.1)
12490     GO TO 12530
12500     L(I)=-EXP(-B*J*0.1)
12510     GO TO 12530
12520     L(I)=EXP(-A*J*0.1)
12530 NEXT I
12540 R1=1/(B-A)
12550 FOR I=1 TO 256
12560     Q1=D(I)*R1
12570     K=1-I
12580     FOR J=I TO 256
12590         H(J)=H(J)+Q1*L(J+K)
12600     NEXT J
12610 NEXT I
12620 END
```

input function has to be stored in the one dimension array D. Matrix L is a temporary storage and the resulting convolution is saved in array H. The time resolution is 0.1 ns and can be changed when required. Further discussion on the accuracy of equation 26 can be found in Chapter V.

### Minor Details

So far, various rate constants have been lumped into two terms, namely A and B. This section reviews what we can extract from them, so that we can plan the experiments accordingly.

The composition of A and B depends on the constituents of the gaseous medium which in turn is prepared according to the desired rate constants in which we are interested. Two cases are considered. The natural decay rates ( $k_{FO}[OH^{**}]$  and  $k_{FI}[OH^*]$ ) are dropped out of our expressions, because fluorescence is very slow compared to the quenching rates.

#### A. Argon and Water

When the medium consists of argon and water only, the term A is

$$A = k_{a1H_2O}[H_2O] + k_{a1O_2}[O_2] + k_{a1Ar}[Ar] + k_{a10Ar}[Ar]. \quad 41$$

If we differentiate A with respect to  $[H_2O]$ , we have

$$\frac{dA}{d[H_2O]} = k_{Q1H_2O} + k_{I1OH_2O}. \quad 42$$

The term B is

$$B = k_{Q0OH_2O} [H_2O] + k_{Q0Ar} [Ar]. \quad 43$$

Differentiating, we get

$$\frac{dB}{d[H_2O]} = k_{Q0OH_2O}. \quad 44$$

In other words, if we measure A and B at various water concentrations, plots of A and B versus water concentration result in straight lines. These straight lines have their slopes equal to  $k_{I1OH_2O} + k_{Q1H_2O}$  for A and  $k_{Q0OH_2O}$  for B. The intercepts at  $[H_2O]=0$  give  $(k_{Q1Ar} + k_{I1Ar})[Ar]$  for A and  $k_{Q0Ar}[Ar]$  for B.

#### B. Nitrogen, Oxygen and Water

Water is not of interest in this case. Its presence is needed only to produce a small number of OH radicals. The water concentration will be kept as low as possible. The term A is

$$A = k_{Q1H_2O} [H_2O] + k_{I1OH_2O} [H_2O] + k_{Q1N_2} [N_2] + k_{I1ON_2} [N_2] \\ + k_{Q1O_2} [O_2] + k_{I1OO_2} [O_2]. \quad 45$$

When A is differentiated with respect to  $[O_2]$ , we get

$$\frac{dA}{d[O_2]} = K_{Q1O_2} + K_{10O_2}. \quad 46$$

The term B is

$$B = K_{Q0O_2}[O_2] + K_{Q0H_2O}[H_2O] + K_{Q0N_2}[N_2] \quad 47$$

and when it is differentiated with respect to  $[O_2]$ , we have

$$\frac{dB}{d[O_2]} = K_{Q0O_2}. \quad 48$$

Therefore, when A and B are measured at various oxygen concentrations, plots of A and B against the concentration of oxygen will result in straight lines with slopes equal to  $K_{Q1O_2} + K_{10O_2}$  for A and  $K_{Q0O_2}$  for B. The intercept at zero  $[O_2]$  for A is equal to

$$K_{Q1H_2O}[H_2O] + K_{10H_2O}[H_2O] + K_{Q1N_2}[N_2] + K_{10N_2}[N_2] \quad 49$$

and B is equal to

$$K_{Q0H_2O}[H_2O] + K_{Q0N_2}[N_2]. \quad 50$$

Finally, the convolution calls for the measurement



of the laser profile and the fluorescence profile. The laser profile will be approximated by either the nitrogen Raman scattering at 302 nm or the Rayleigh scattering at 282 nm. The fluorescence will be obtained at 309 nm. For all the measurements, photoelectron arrival rate will be maintained around 0.05 per laser pulse whenever the signal is strong enough.

The ideal way to carry out the experiments is to alternate the measurements between the laser profile and the fluorescence profile to minimize the effect of drifting of the detection system. In reality, practical experimental difficulties necessitate measurement of the laser profile at the beginning and the end of an experiment. As many laser profiles as possible will be measured between fluorescence measurements. Then the sum of all these measured laser profiles will be considered as the input function.

Finally, since the theory assumes that the system is linear, we have to avoid saturation. Thus, the laser power will be kept low and the laser beam diameter will be made correspondingly large.

## CHAPTER III

### EXPERIMENTAL

The experimental setup is illustrated in Figures 11 and 12. OH radicals were generated by 185 nm photolysis of water by two mercury lamps at atmospheric pressure in the fluorescence cell. The laser beam was directed across the center of the OH cell. The 6 ns half-width laser pulses at 282 nm were obtained from a frequency-doubled Rh6G dye laser pumped by a frequency doubled Nd-YAG laser. The 282 nm pulses had an energy of about 0.1 mJ and a spectral FWHM of about  $0.5\text{ cm}^{-1}$ . Fluorescence in the detection zone was collected by a silica lens and unwanted Rayleigh and Raman scattering were filtered by a cellulose triacetate film and a 2.8 nm bandpass 1/4-m monochromator.

The fluorescence signal was detected by a RCA 8575 photomultiplier attached to an ORTEC 270 constant fraction discriminator adjusted according to the specifications in the manufacturer's manual. The discriminator output was passed to the stop input of a LeCroy QVT3001 MCA used in the time mode. The start pulse was generated by a reverse-biased photodiode (Motorola MRD 500) looking at a portion of the undoubled 564 nm output of the frequency-doubling crystal and delayed for about 40 ns to compensate for the transit time of the PMT and the

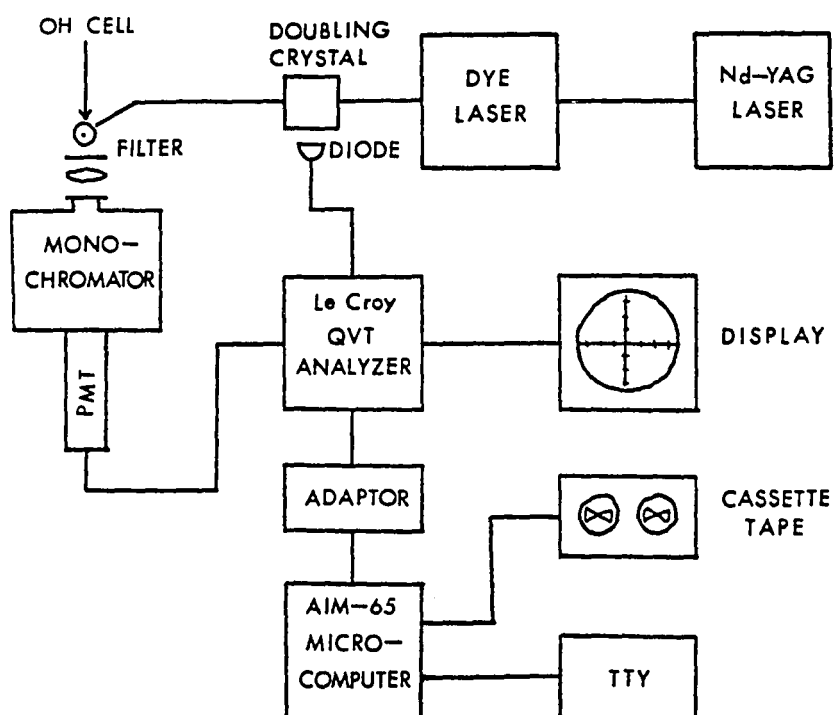


Figure 11 Schematics of experimental setup.

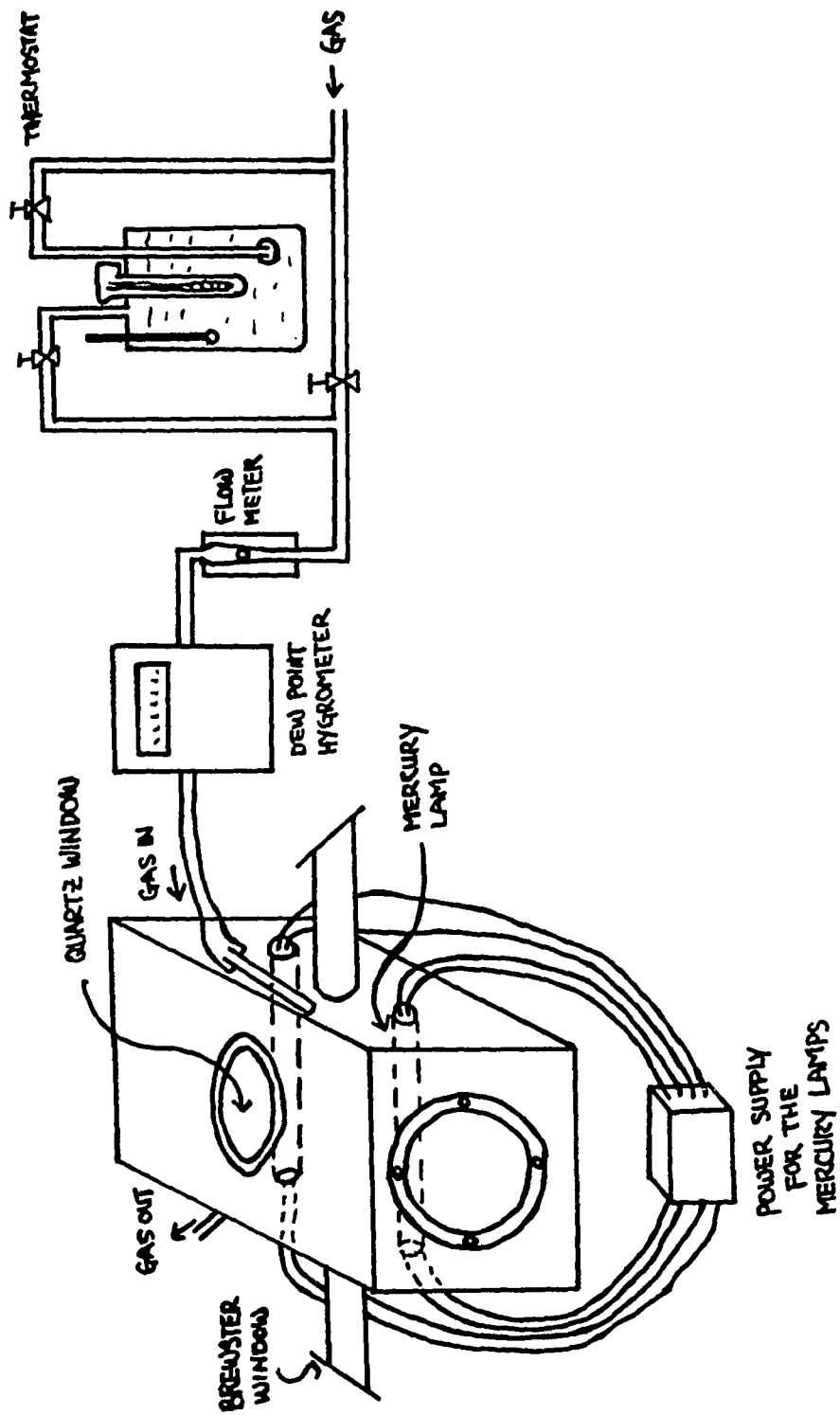


Figure 12 OH fluorescence cell.

discriminator. The number of laser pulses fired since the beginning of the experiment was obtained by adding the no-event channel of the MCA and the total number of counts stored. This total number of cycles was used for Coates correction at the end of an experiment. The result recorded by the MCA could be displayed on an oscilloscope or read out, on command, into a Rockwell AIM-65 microcomputer through a home-made interface adaptor. The final result was stored on cassette tape and analyzed either on a Tektronix 4051 desk-top graphic microcomputer or on the Honeywell 66/40 computer. The resolution of the MCA was set to 0.1 ns per channel or 0.4 ns per channel depending on the fluorescence decay rate.

The OH fluorescence cell was made of aluminum and both the inside and outside surfaces were black anodized. Openings, sealed off by removable lids, were made so that the inside could be reached for optical alignments. The cell was capable of being evacuated. To reduce the background from the two mercury lamps, both lamps were masked-off, leaving only two slots parallel to the detection zone exposed. The volume of the cell was about one liter. All the inside surfaces were roughened to reduce reflections of light.

Tygon tubing was used to deliver gas into the cell. The water content of the gas was monitored before it entered the cell by either a EG&G 911 Dew-All or General

Eastern 1100DP dew point hygrometer. Gas flow rate was maintained at about 200 cc per minute to prevent contaminants from building up and to cool the contents of the cell. The lowest dew point which could be reached was between  $-14.5^{\circ}\text{C}$  and  $-18.0^{\circ}\text{C}$  and was dependent upon the room temperature and the purity of the gas source.

Signal attenuation was achieved by putting masks with various size holes in front of the quartz window. The cellulose triacetate film was moved from the entrance slit to the exit slit of the monochromator during the later experiments, to reduce the fluorescence of the acetate film induced by the light from the mercury lamps.

Further technical details on the electronics of the instruments which were designed and built in the laboratory can be found in appendices B and C.

Some remarks on the practical side of the experiments are in order. The most distressing of all the problems encountered was that the computing time for evaluating equation 26 was tremendous. It took over 20 minutes to do one calculation of equation 26 by a Tektronix 4051 desk-top microcomputer. Each simplex search required evaluating equation 26 several hundred times. This long computing time made it impractical to do the computation on a small computer. The Honeywell 66/40 could handle the job fairly well but computer time was costly, about 100 dollars per simplex analysis.

The photon counting technique entailed a low arrival rate. This required many laser shots. Adding to the problem, the laser pulsed at 6 shots per second. Thus it took a very long time to complete one curve. The arrival rate was kept around 0.05 per laser pulse. In general, each gas mixture required from 40 to 80 hours of experimental time.

In some experiments, a background persisted when the laser was tuned off resonance. This compounded the problem, for it required extra experiments to characterize the background in order to subtract the background from the fluorescence curves.

At first, the background was due to stray light at 282 nm sneaking through the monochromator. This problem was corrected with the cellulose triacetate film. Then another problem crept up after the dye oscillator was modified from a grating to a mirror. The new background had a certain long decay time. This again compounded the problem of lengthy experimental time.

The laser itself was a huge and complex system. Components had limited operational life-time, so down times were inevitable after continuous operation. In conclusion, these experiments were not as easy as they looked!

## CHAPTER IV

### RESULTS

#### Data and Comments

The experimental results of OH fluorescence in both the argon plus water and the nitrogen/oxygen/water cases are summarized in Figures 13 to 22. Each graph represents the cumulative data collected for one gas mixture. The data are corrected according to the Coates algorithm and smoothed by a five point running average. The laser profiles are shown in Figures 13 and 14 to illustrate the drastic difference between the laser and the fluorescence curves. The solid lines are the least squares fits of equation 26 to the data found via the simplex method.

Tables III to XI summarize the experimental results. The A, B and C in the Tables are the results of the simplex searches. The error column in the Tables are calculated according to the definition:

$$\sigma = \frac{1}{N} \sqrt{\sum_{i=1}^N \frac{(f(i) - f_c(i))^2}{f_c(i)}} \quad 51$$

Where  $f(i)$  is the datum and  $f_c(i)$  is the calculated value of the least squares fit.

The unweighed least squares fits are the results of a three parameter search. The third parameter, besides A



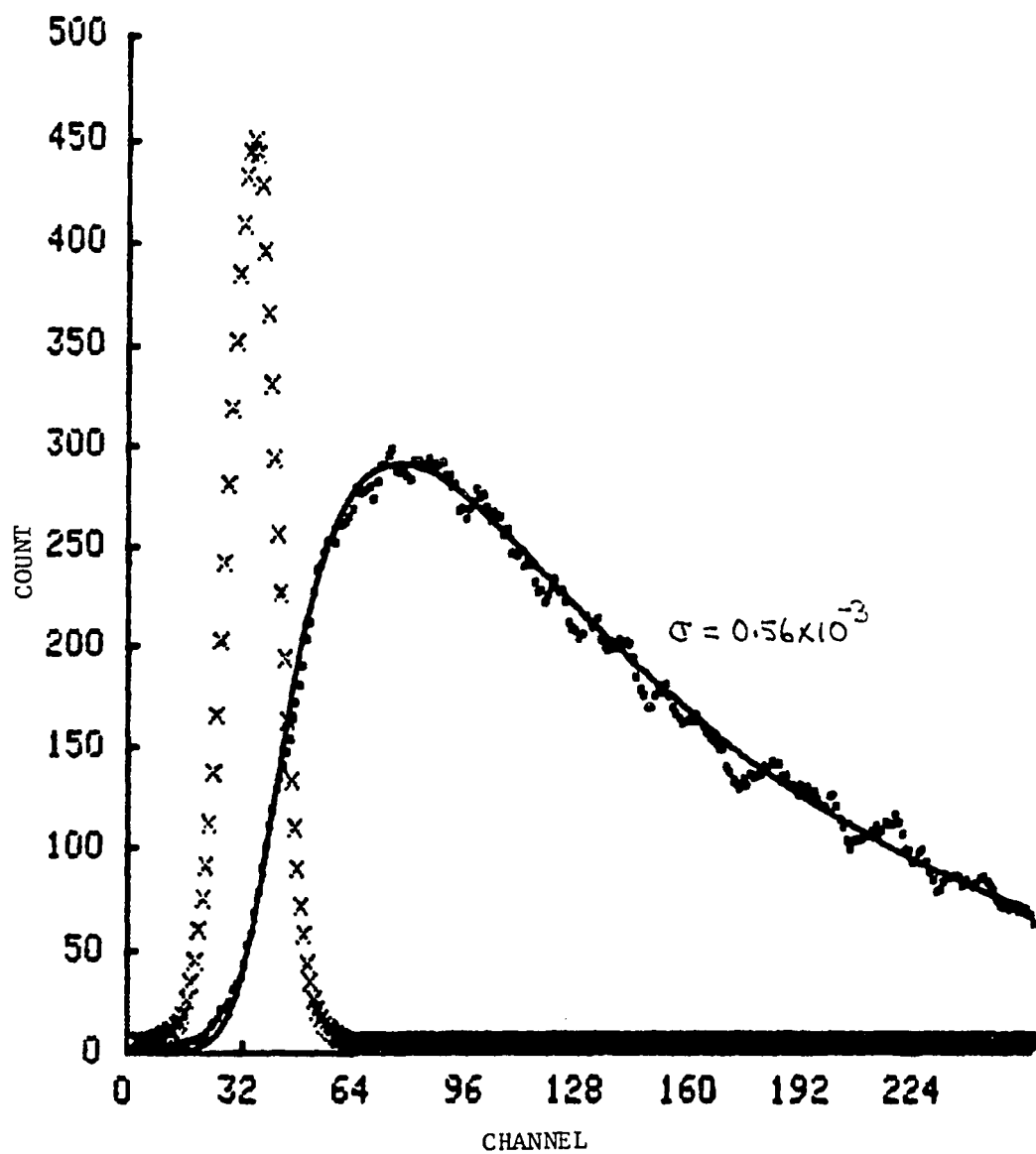


Figure 13 Fluorescence decay of OH in argon plus water (D.P. -16.0C): x-laser profile; .-fluorescence; solid line-least squares fit. Time scale is 0.4 ns per channel.

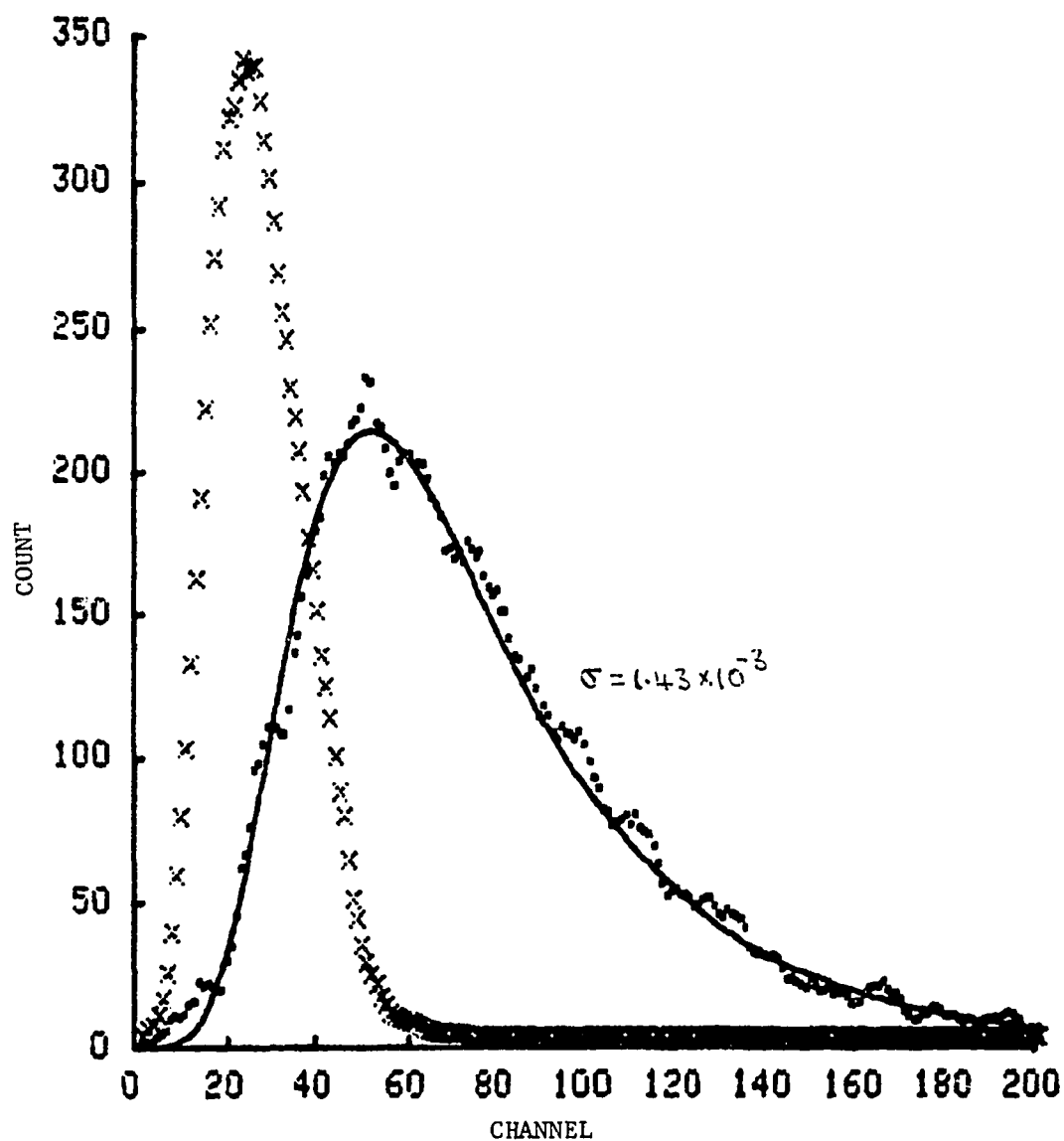


Figure 14 Fluorescence decay of OH in argon plus water (D.P. -7.0C): x-laser profile; .-fluorescence; solid line-least squares fit. Time scale is 0.4 ns per channel.

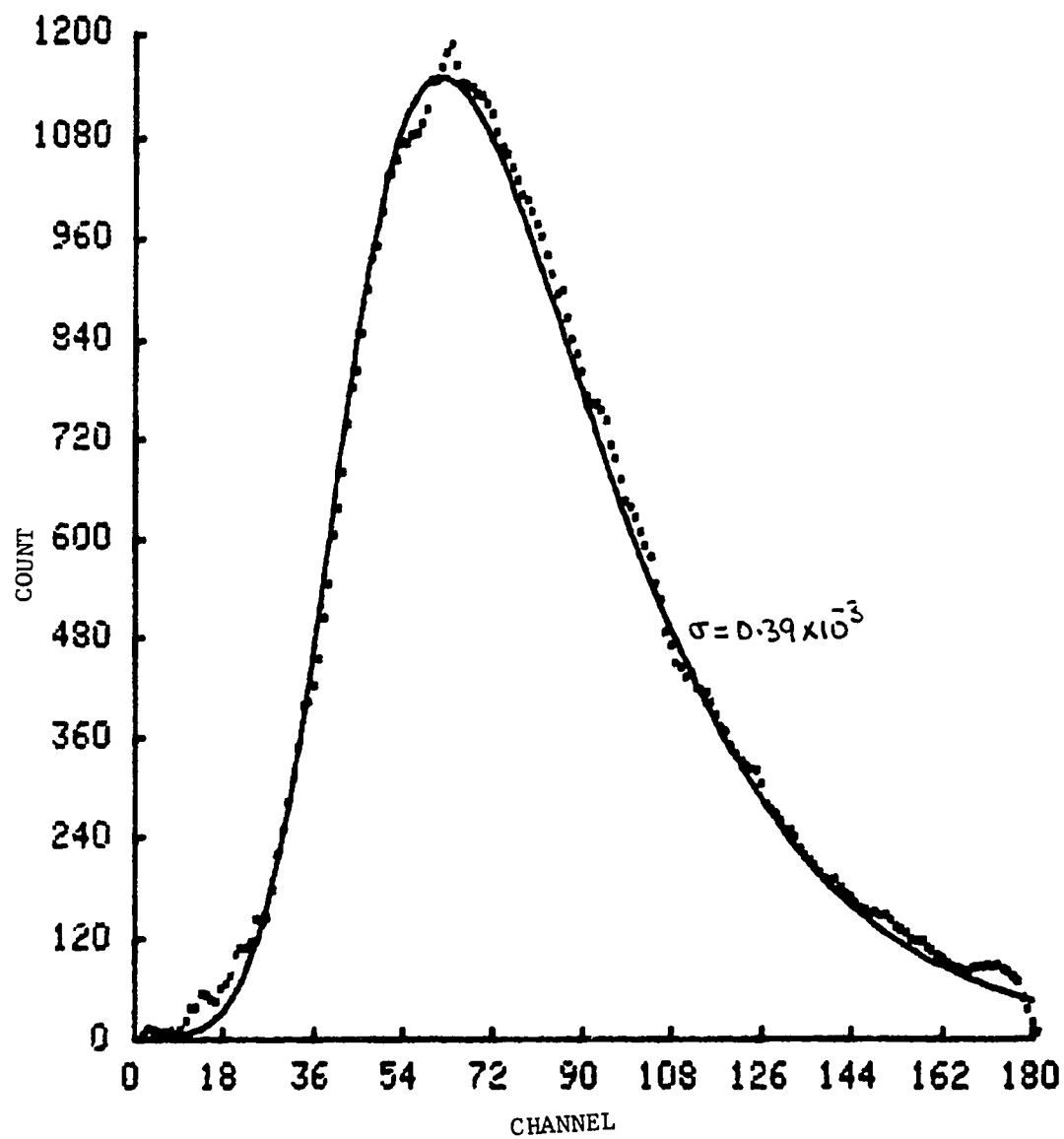


Figure 15 Fluorescence decay of OH in argon plus water (D.P. 4.0C). Laser profile is not shown. Time scale is 0.2 ns per channel.

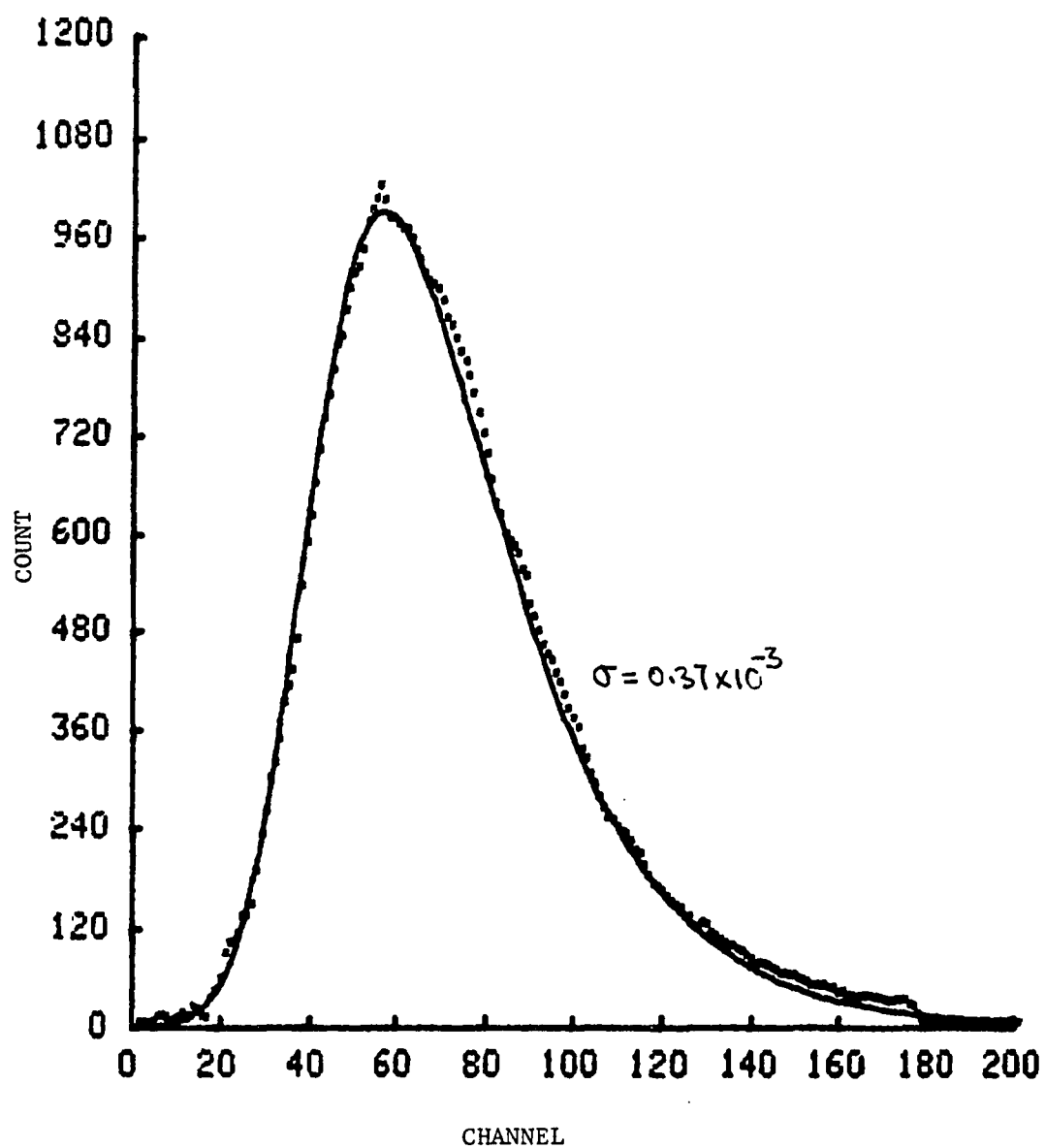


Figure 16 Fluorescence decay of OH in argon plus water (D.P. 9.0C). Time scale is 0.2 ns per channel.

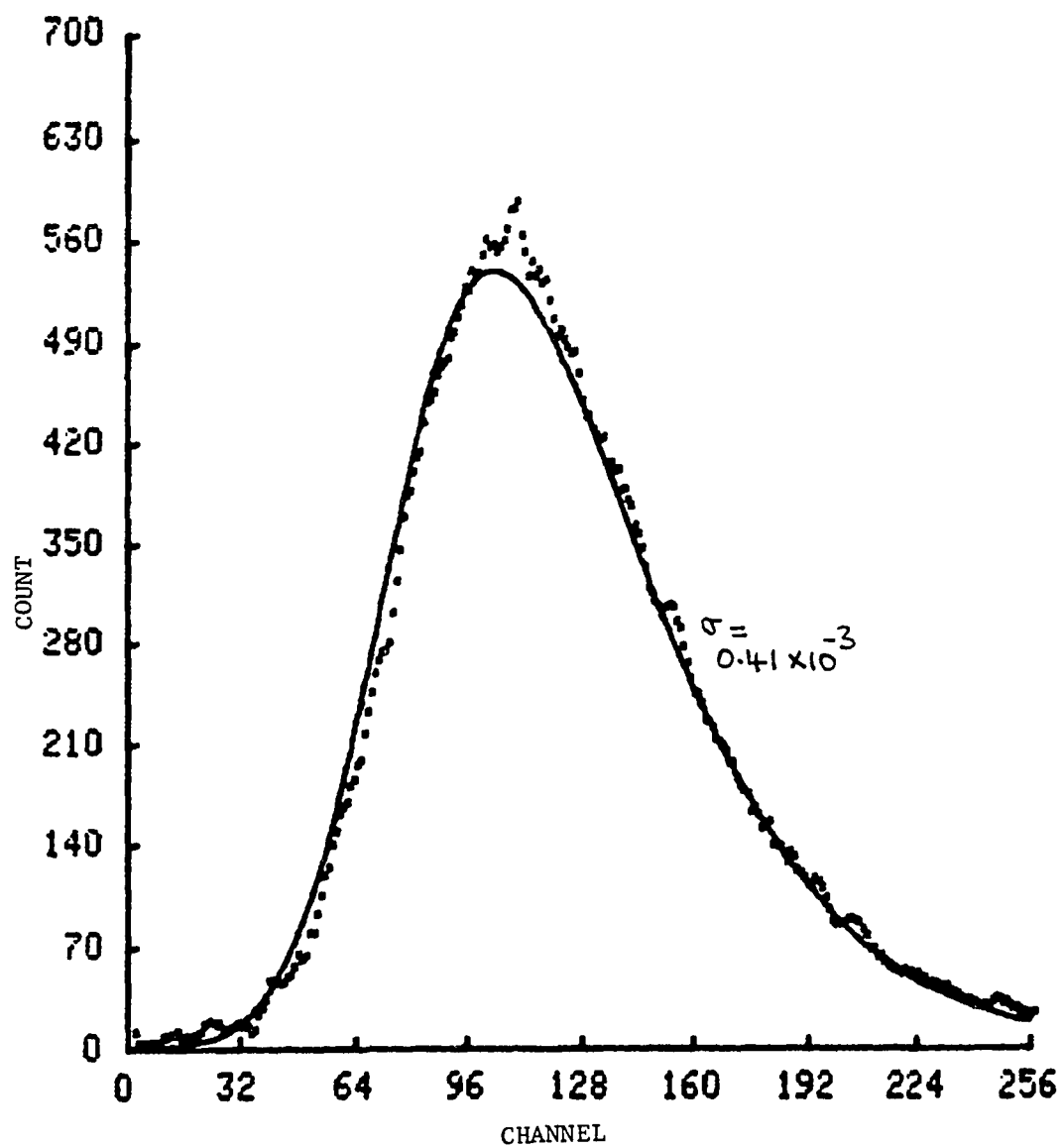


Figure 17 Fluorescence decay of OH in argon plus water (D.P. 16.0C). Time scale is 0.1 ns per channel.

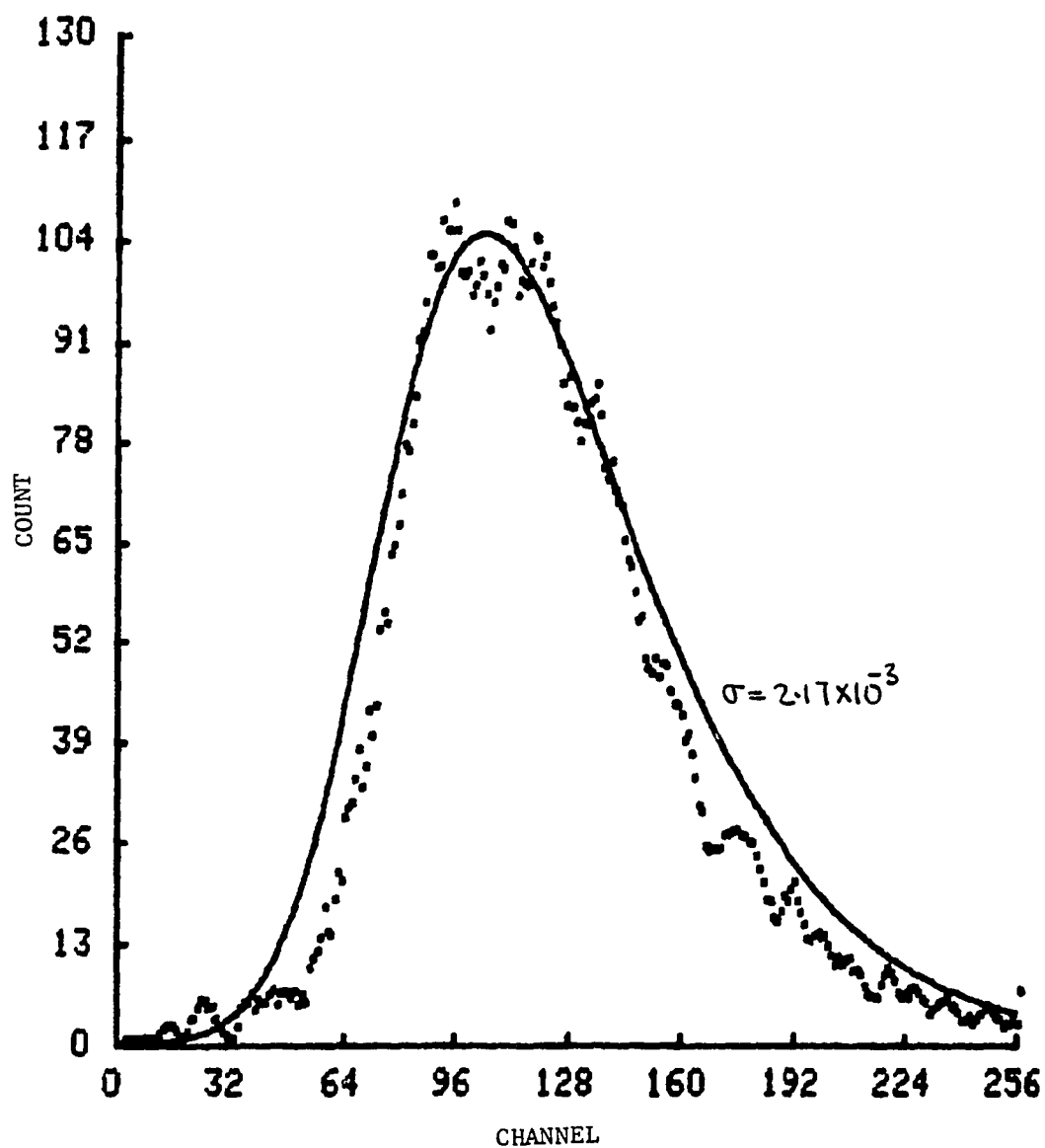


Figure 18 Fluorescence decay of OH in argon plus water (D.P. 19.0C). Time scale is 0.1 ns per channel. It is a bad result; see text for discussion.

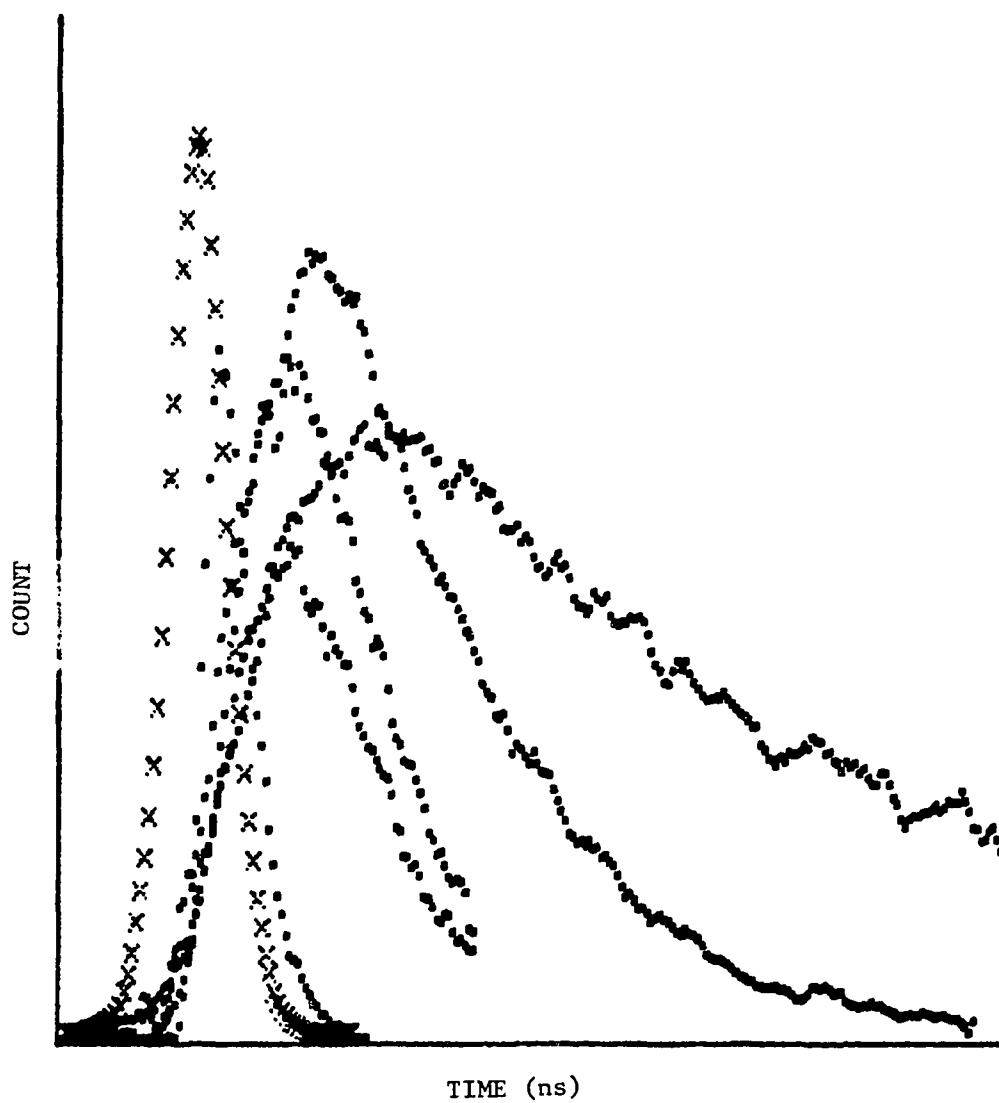


Figure 19 Fluorescence decays of OH in argon plus water  
. - fluorescence at different water  
concentrations. x - laser profile. The graph  
shows the drastic difference in the decay curves  
due to the change in water concentration.

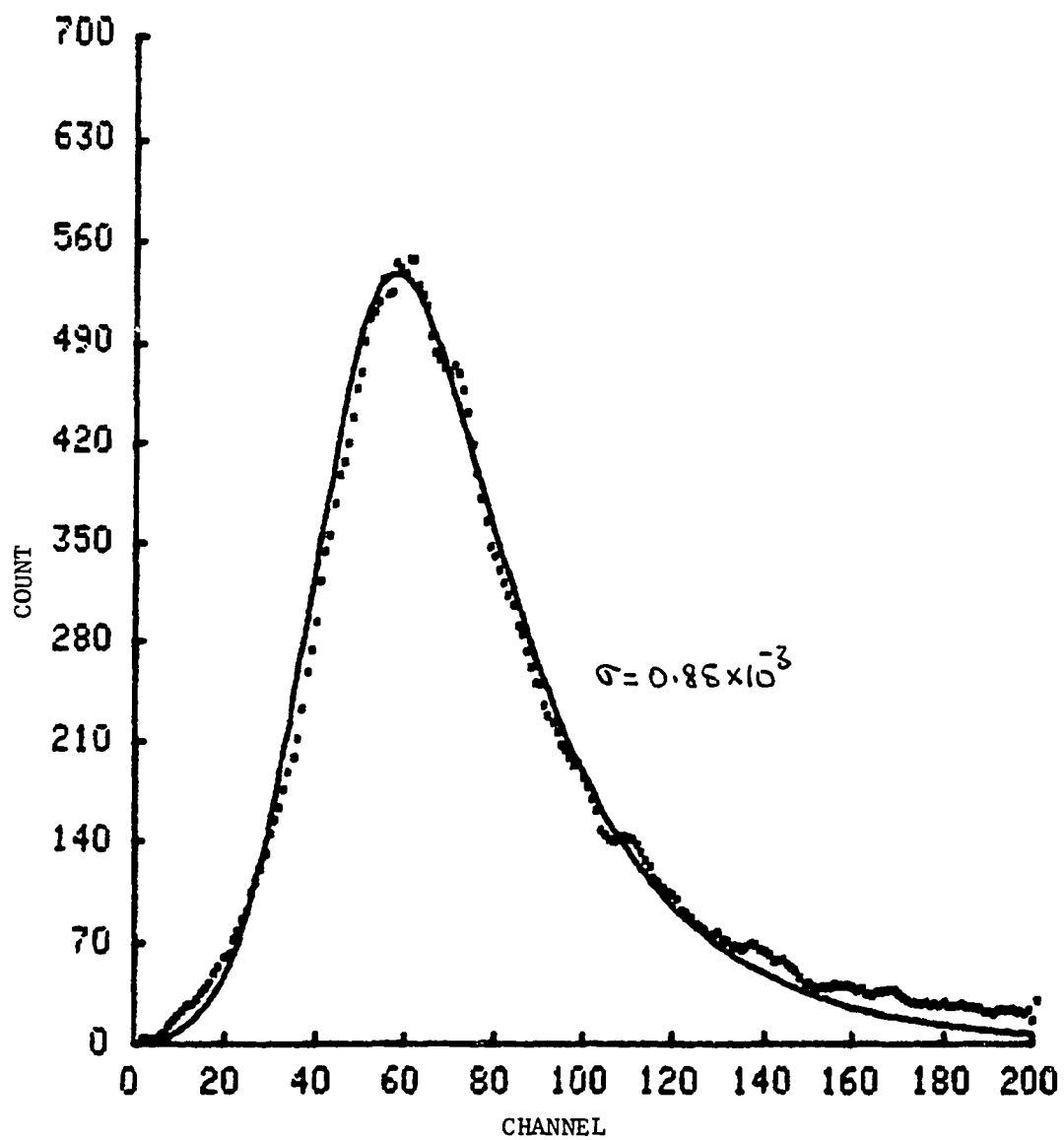


Figure 20 Fluorescence decay of OH in nitrogen  
(D.P. -16.0C). Time scale is 0.2 ns per channel.



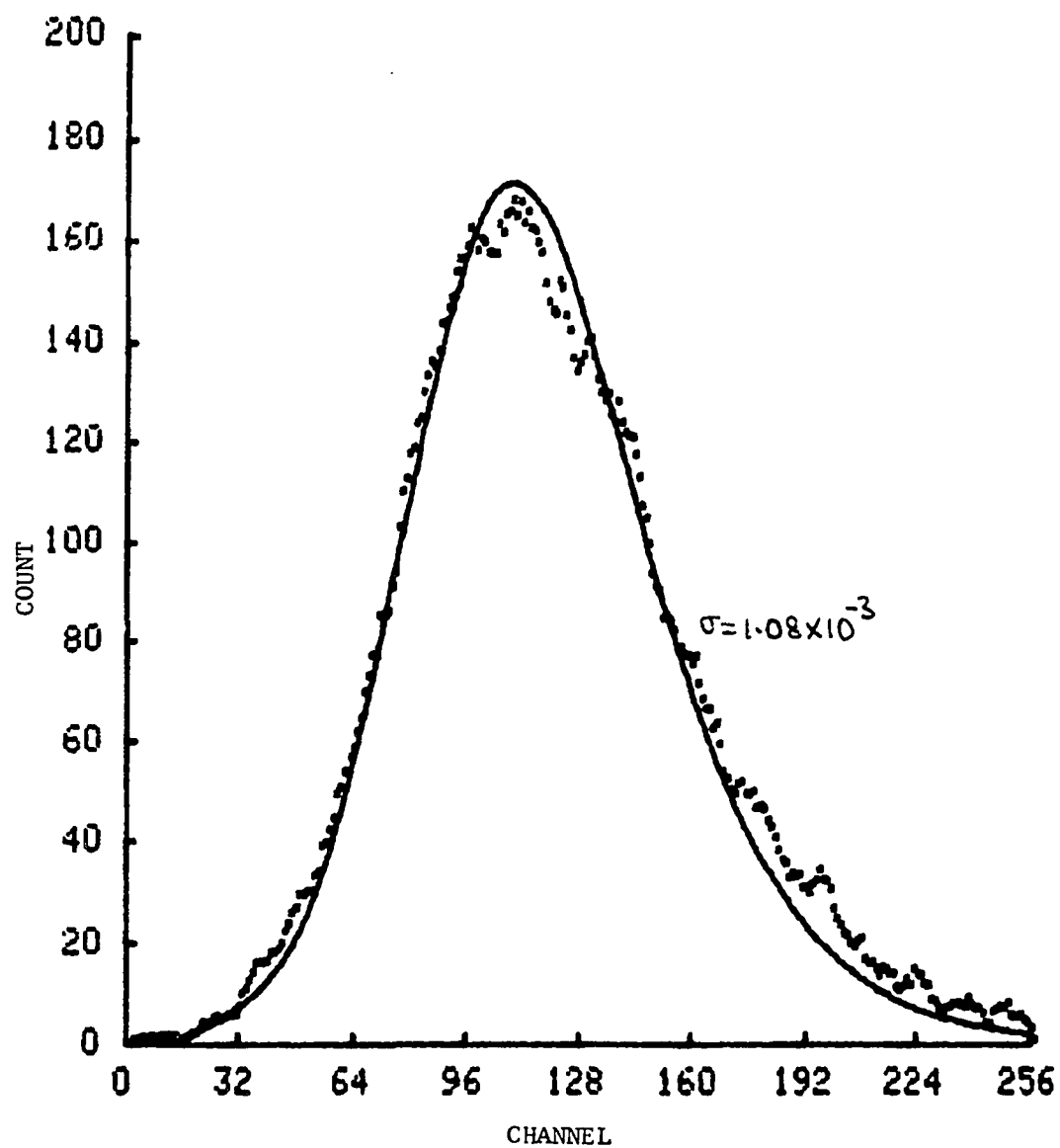


Figure 21 Fluorescence decay of OH in nitrogen plus 2% oxygen. Time scale is 0.1 ns per channel.

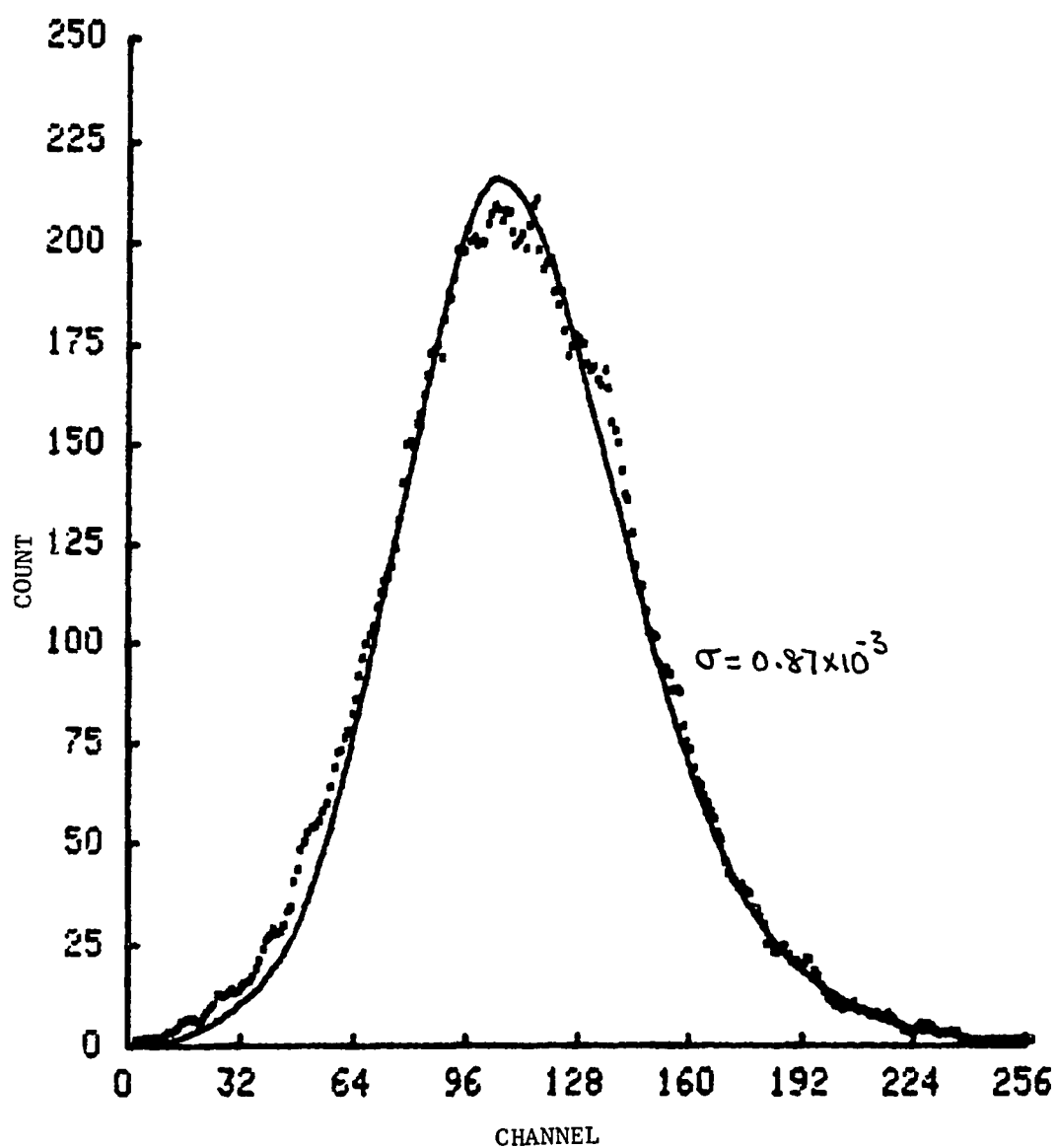


Figure 22 Fluorescence decay of OH in nitrogen plus 5% oxygen. Time scale is 0.1 ns per channel.

TABLE III  
RESULTS OF SIMPLEX SEARCH

Argon/water (dew point 19.0C).

Water concentration;  $(5.33 \pm 0.5) \times 10^{17}$  molecule/cc.

Units of A and B are  $\text{ns}^{-1}$ .

	Count	B	A	C	$\sigma$ ( $\times 10^{-3}$ )
	8933	0.42	0.35	0.0029	2.17
Uncertainty	--	0.1	0.1	--	--

TABLE IV  
RESULTS OF SIMPLEX SEARCH

Argon/water (dew point 16.0C).

Water concentration;  $(4.53 \pm 0.15) \times 10^{17}$  molecule/cc.

Units of A and B are  $\text{ns}^{-1}$ .

	Count	B	A	C	$\sigma$ ( $\times 10^{-3}$ )
	14199	0.334	0.335	0.0038	1.43
	10048	0.338	0.337	0.0027	2.47
	10559	0.419	0.413	0.0038	2.82
	15052	0.396	0.355	0.0043	1.75
Cumulative	51576	0.371	0.367	0.0154	0.41
Average	--	0.371	0.361	--	--
Uncertainty	--	0.037	0.032	--	--

TABLE V  
RESULTS OF SIMPLEX SEARCH

Argon/water (dew point 9.0C).

Water concentration;  $(2.78 \pm 0.08) \times 10^{17}$  molecule/cc.

Units of A and B are  $\text{ns}^{-1}$ .

	Count	B	A	C	$\sigma$ ( $\times 10^{-3}$ )
	9335	0.222	0.231	0.00217	2.25
	18994	0.263	0.279	0.00614	0.75
	13247	0.238	0.265	0.00374	1.2
Cumulative	59542	0.222	0.348	0.0198	0.37
Average	--	0.236	0.281	--	--
Uncertainty	--	0.049	0.019	--	--

TABLE VI  
RESULTS OF SIMPLEX SEARCH

Argon/water (dew point 4.0C).

Water concentration;  $(1.96 \pm 0.05) \times 10^{17}$  molecule/cc.

Units of A and B are  $\text{ns}^{-1}$ .

	Count	B	A	C	$\sigma$ ( $\times 10^{-3}$ )
	16041	0.213	0.248	0.00367	1.60
	16082	0.190	0.297	0.00395	0.91
	18296	0.199	0.210	0.00344	1.13
	27417	0.190	0.193	0.0045	1.08
Cumulative	103617	0.213	0.218	0.0164	0.39
Average	--	0.201	0.233	--	--
Uncertainty	--	0.012	0.041	--	--

TABLE VII  
RESULTS OF SIMPLEX SEARCH

Argon/water (dew point -7.0)

Water concentration;  $(0.81 \pm 0.02) \times 10^{17}$  molecule/cc.

Units of A and B are  $\text{ns}^{-1}$ .

	Count	B	A	C	$\sigma$ ( $\times 10^{-3}$ )
	15548	0.066	0.198	0.0048	1.43
	21688	-	0.135*	0.045	1.69
Average	--	0.066	0.167	--	--
Uncertainty	--	0.007	0.03	--	--

\* Result of 314 nm measurement.

TABLE VIII  
RESULTS OF SIMPLEX SEARCH

Argon/water (dew point -16.0C).

Water concentration;  $(0.39 \pm 0.04) \times 10^{17}$  molecule/cc.

Units of A and B are  $\text{ns}^{-1}$ .

	Count	B	A	C	$\sigma$ ( $\times 10^{-3}$ )
	7453	0.0289	0.170	0.00099	2.60
	13772	0.0262	0.156	0.00156	1.66
	20261	0.0274	0.149	0.00242	1.30
	27368	0.0341	0.147	0.00285	0.89
	33486	0.0241	0.135	0.00317	0.70
Cumulative	40441	0.0228	0.123	0.00342	0.56
Average	--	0.0256	0.147	--	--
Uncertainty	--	0.0023	0.016	--	--

TABLE IX  
RESULTS OF SIMPLEX SEARCH

Nitrogen/water (dew point -16.0C).  
Water concentration;  $(0.39 \pm 0.04) \times 10^{17}$  molecule/cc.  
Units of A and B are  $\text{ns}^{-1}$ .

	Count	B	A	C	$\sigma$ ( $\times 10^{-3}$ )
	6245	0.19	2.02	0.0397	4.08
	7016	0.17	1.97	0.0415	2.65
	7017	0.19	1.92	0.0431	2.96
	7049	0.15	2.49	0.048	2.45
	5083	0.17	1.27	0.021	4.29
Cumulative	32409	0.17	1.87	0.179	0.85
Average	--	0.17	1.92	--	--
Uncertainty	--	0.015	0.39	--	--

TABLE X  
RESULTS OF SIMPLEX SEARCH

Nitrogen/2% oxygen/water (dew point -16.0C).  
Water concentration;  $(0.39 \pm 0.04) \times 10^{17}$  molecule/cc.  
Units of A and B are  $\text{ns}^{-1}$ .

	Count	B	A	C	$\sigma$ ( $\times 10^{-3}$ )
	7220	0.40	2.25	0.022	1.98
	7931	0.39	4.49	0.048	1.51
Cumulative	15343	0.40	3.91	0.082	1.08
Average	--	0.40	3.55	--	--
Uncertainty	--	0.006	1.16	--	--

TABLE XI  
RESULTS OF SIMPLEX SEARCH

Nitrogen/5% oxygen/water (dew point -16.0C)  
(See also Figure 23 and accompanying discussion).  
Units of A and B are ns<sup>-1</sup>.

Cumulative Count	B	A	C	$\sigma$ ( $\times 10^{-3}$ )
941	0.45	6.48	0.01	7.01
1830	0.44	5.96	0.017	4.21
2721	0.41	5.30	0.021	3.20
3598	0.40	5.59	0.029	2.90
4573	0.43	5.0	0.035	2.38
5406	0.45	4.39	0.038	2.07
6386	0.49	4.61	0.050	1.79
7181	0.53	3.01	0.040	1.74
8068	0.6	2.31	0.038	1.72
8994	0.55	4.78	0.082	1.45
9906	0.57	2.47	0.048	1.73
10794	0.54	3.15	0.063	1.62
11710	0.56	2.70	0.061	1.54
12627	0.55	5.14	0.124	1.17
13480	0.59	3.38	0.094	1.13
14385	0.56	3.71	0.103	1.11
15288	0.57	2.98	0.090	1.07
16181	0.54	4.09	0.125	0.90
17070	0.52	5.20	0.163	0.83
18005	0.52	4.93	0.161	0.87
Average	0.51	4.26	--	--
Uncertainty	0.06	1.23	--	--



and B as defined in equations 11 and 12, is a normalizing factor, C. This normalizing factor is required because the total count, thus the area, of each curve varies. Figure 19 displays the fluorescence of OH in argon with different water concentrations. Please notice the marked change in the decay rates.

The parameter C is only a mathematical normalization constant. It has no relation to the small letter c defined in equation 23. The value of C can be changed either by changing the total count of the laser profile or the fluorescence profile. To measure c, we need an absolute intensity measurement not statistical counting. The statistical nature of the experimental approach has rendered c inaccessible.

The results shown in Table XI will be used to illustrate the point. It can be shown

$$\text{Area of fluorescence curve} = \text{Area of laser} \times C/AB \quad 52$$

If we plot C/AB versus count ( $\times 0.1$ ) shown in Table XI, a straight line with the reciprocal of the slope equal to the area of the laser profile results, because the same laser profile was used throughout all the simplex analysis shown in Table XI. Figure 23 shows such a plot. The reciprocal of the slope of the straight line is 28944. The actual total count of the laser profile is 28098. The two differ by 3%.

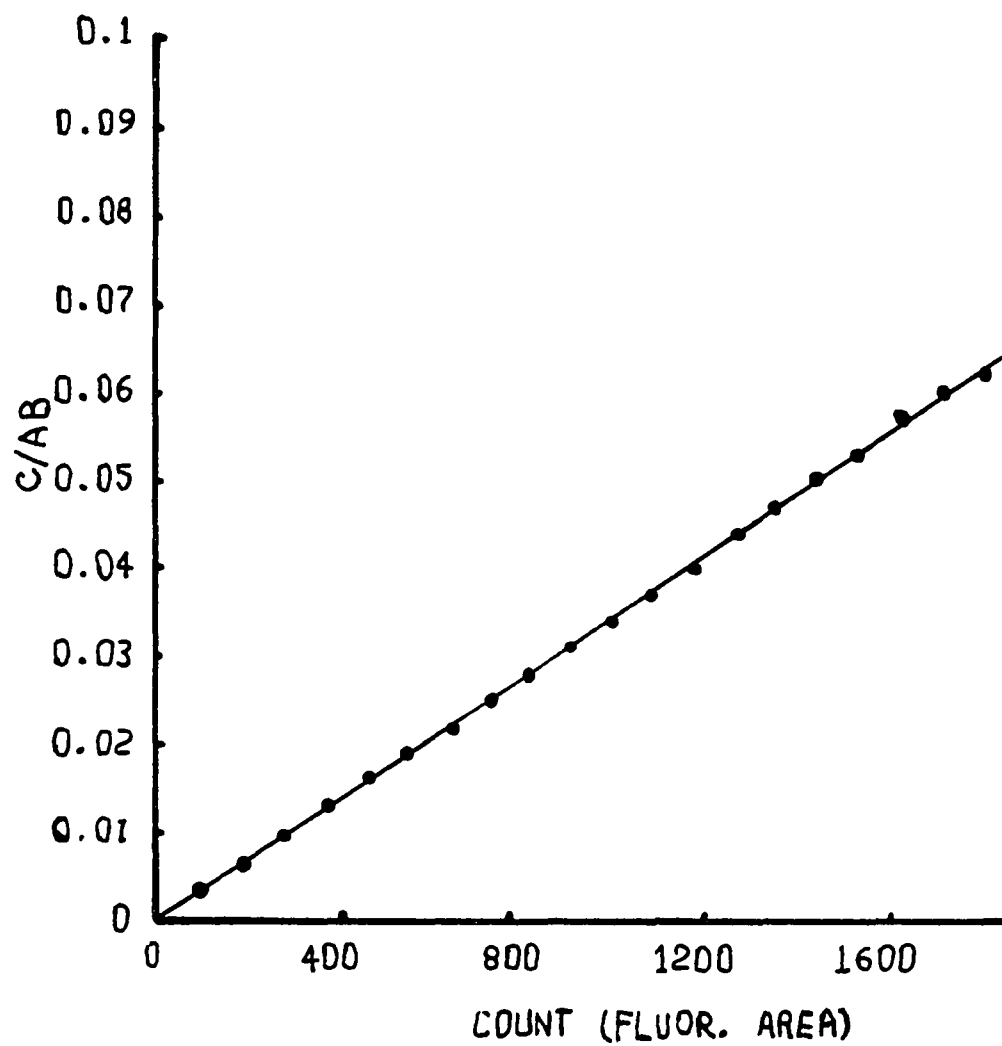


Figure 23 Linear least squares fit of  $C/AB$  versus cumulative count ( $\times 0.1$ ) tabulated in Table XI.

Figure 18 shows the fluorescence decay of OH in argon and water at a concentration around that corresponding to a dew point 19.0C. The result is obviously not satisfactory. Dew point 19.0C was close to the saturation point at room temperature (winter). The room temperature varied over the period of the experiment so it was hard to maintain a constant water concentration. At the time of this experiment, there was no dew point hygrometer available but a simple detector which did not operate too well at high water concentration. In brief, it is preferred not to carry out experiments at dew points close to room temperature. Instead of discarding the result, it is presented here as an illustration of what a bad fit looks like. The other reasonable fits are no coincidences. All the other results indicate that the model is indeed correct.

Due to the statistical nature of the photon counting method, there is no standard on how many counts could be accumulated before an experiment is terminated. By the same token, the result of large total count is an experiment while lesser count result could be considered an individual experiment only with less accuracy. The interesting consequence of this is that we can add all the experiments into a single giant experiment. Table IV to Table X except VII show more than one experimental result for each gas mixture, while Figures 13 to 21 show

collective experimental data representing all the data for each gas mixture. These experiments with smaller counts can be viewed as results from breaking down the giant experiments. On the other hand, each individual experiment can be considered as an independent experiment. Generally, large count experiments are more accurate, so that the collective data should constitute the final results. But this is not always the case as will be discussed in the Convergence Test section of Chapter V, because a large count requires a long experimental time. But, a long experimental time increases other experimental errors due to such factors as changes in room temperature. Eventually these uncontrollable errors are large enough to wipe out the gain by increasing count. As the final decision, the average of all the small count results was taken as the final result for that gas mixture and the standard deviation among the small count results was given as the estimated error.

### Data Analysis

All the evidence indicates that the two parameter model is indeed consistent with the data. The next logical step, as a further check on the tenability of the model, is to analyze A's and B's and compare the results to the available literature values.

Figure 24 shows graphically the linear least squares fits to the the A's and B's of argon plus water as a function of water concentration. Figure 25 shows similar plots for A's and B's of nitrogen and oxygen as a function of oxygen concentration. Table XII summarizes the results of the least squares fits.

Due to the nature of the characteristic response function, A and B are indistinguishable. That is, A and B of equation 19 can be interchanged without affecting the function. This creates the problem of labeling the two values obtained by the simplex search. The problem in the argon/water case can be broken into two parts. One is how to group the experimental results into two groups, A's and B's, and the other is how to identify the two groups.

From each experiment at a water concentration in argon, we obtain a pair of values. After several experiments at different water concentrations, we obtain several pairs of values. A value from each pair is assigned to a group in such a way that the resulting group forms a straight line when plotted against water

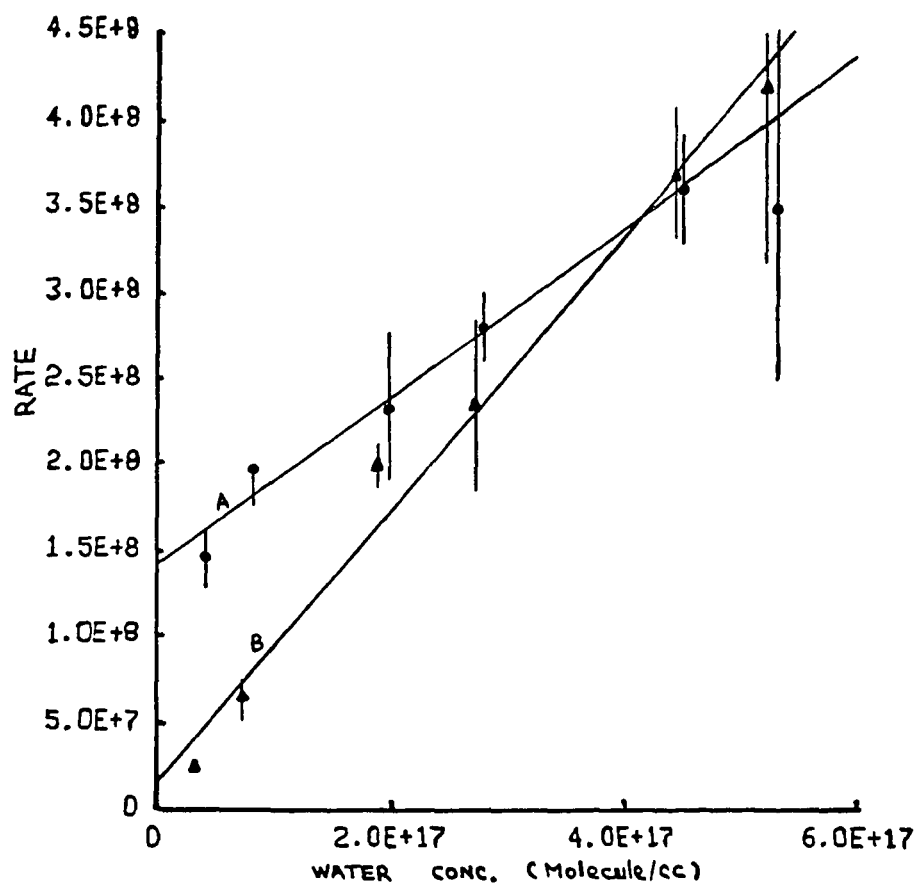


Figure 24 Linear least squares fit to A's and B's in argon as a function of water concentration.

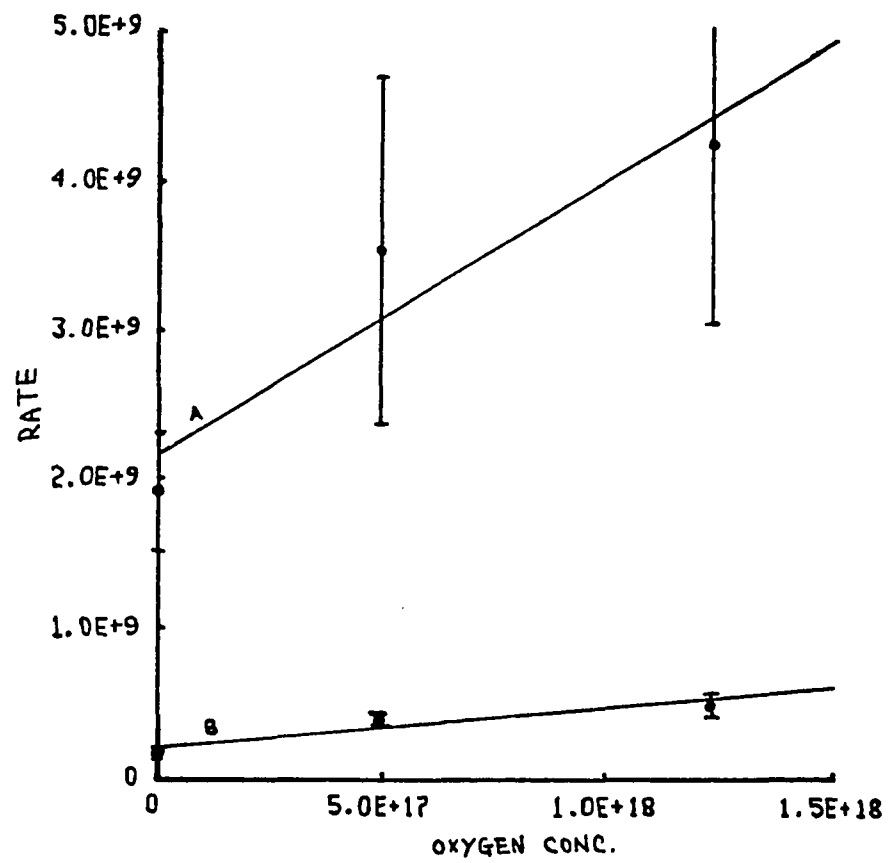


Figure 25 Linear least squares fit to A's and B's in Nitrogen and Oxygen.

TABLE XII  
RESULTS OF LINEAR LEAST SQUARES FITS  
TO A's AND B's

Units of slopes are  $\text{cm}^3 \text{sec}^{-1} \text{molecule}^{-1}$ . Units of intercepts are  $\text{sec}^{-1}$ .

N <sub>2</sub> + O <sub>2</sub>					H <sub>2</sub> O + Ar				
	Slope	Error	Intercept	Error		Slope	Error	Intercept	Error
A	1.83x10 <sup>-9</sup>	0.43x10 <sup>-9</sup>	2.18x10 <sup>9</sup>	0.16x10 <sup>9</sup>		4.88x10 <sup>-10</sup>	0.44x10 <sup>-10</sup>	1.41x10 <sup>8</sup>	0.03x10 <sup>8</sup>
B	2.65x10 <sup>-10</sup>	0.57x10 <sup>-10</sup>	2.06x10 <sup>8</sup>	0.21x10 <sup>8</sup>		7.9x10 <sup>-10</sup>	0.47x10 <sup>-10</sup>	1.17x10 <sup>7</sup>	0.34x10 <sup>7</sup>



concentration, Figure 24. The straight-line criterion results from the linear dependency of A and B on water concentration. The general guideline for grouping is that below water concentration of  $5 \times 10^{17}$  molecule/cc the high values of the pairs belong to one group and the low values belong to the other group.

After grouping the values, the next step is to indentify which group is A and which group is B. Notice that A denotes the relaxation from the  $v'=1$  state. The identification process involves measuring the fluorescence intensity at 309 nm and 314 nm under controlled conditions. The rationale behind this experiment is given by the following arguments.

Based on equation 19 and 27 we can write the fluorescence decay at 309 nm as

$$h(t)_{309} = \int_0^t f(\tau) \frac{k'_{10} c' (e^{-A(t-\tau)} - e^{-B(t-\tau)})}{B - A} d\tau \quad 53$$

The  $c'$  is defined as  $c' = c \cdot k_{F0}$  and  $c$  is defined in equation 23. Based on equation 15 and 27, we have the fluorescence at 314 nm as

$$h(t)_{314} = \int_0^t f'(\tau) c' e^{-A(t-\tau)} d\tau. \quad 54$$

The corresponding integrated fluorescence (I) at 309 nm and 314 nm can be shown to be

$$I(309) = \frac{k'_{10} c'}{AB} \text{Area(Laser)}, \quad s5$$

$$I(314) = \frac{c'}{A} \text{Area(Laser)}. \quad s6$$

The Area(Laser) denotes the integrated area of the laser profile. Therefore, the ratio of I(309) to I(314) is

$$\frac{I(309)}{I(314)} = \frac{k'_{10}}{B}.$$

$k'_{10}$  and B depend on the constituents of the gas. For the argon/water case, we have

$$\frac{I(309)}{I(314)} = \frac{k_{10H_2O} [H_2O] + k_{10Ar} [Ar]}{k_{Q0H_2O} [H_2O] + k_{Q0Ar} [Ar]}. \quad s7$$

The first experiment was to measure the ratio  $k_{10H_2O}/k_{Q0H_2O}$ . Since Helium is the least effective quencher,

$$\frac{I(309)}{I(314)} = \frac{k_{10H_2O} [H_2O] + k_{10He} [He]}{k_{Q0H_2O} [H_2O] + k_{Q0He} [He]}. \quad s8$$

At high enough water concentration equation 57 becomes

$$\frac{I(309)}{I(314)} = \frac{k_{10H_2O}}{k_{Q0H_2O}}.$$

This assumption was checked by measuring the ratios at various water concentrations. The result is shown in Figure 26. The result indeed shows that at dew point 17.0°C, the ratio does approach the limit of  $k_{10H_2O}/k_{QOH_2O}$ . The value is  $0.43 \pm 0.07$ . By fitting equation 57 to the four points shown in Figure 25, we obtain the rough estimate of  $k_{QOH_2} (3.4 \times 10^{-14})$  and  $k_{10H_2} (1.4 \times 10^{-12})$ . Based on the ratio, equation 58, and the least squares fits of A's and B's (Table XII), we have the following two choices:

Choice	1	2
$k_{QOH_2O}$	$7.9 \times 10^{-10}$	$4.88 \times 10^{-10}$
$k_{Q1H_2O}$	$1.48 \times 10^{-10}$	$5.8 \times 10^{-10}$
$k_{10H_2O}$	$3.4 \times 10^{-10}$	$2.1 \times 10^{-10}$
$k_{QOAr}$	$4.76 \times 10^{-13}$	$5.73 \times 10^{-12}$
$k_{Q1Ar} + k_{10Ar}$	$5.73 \times 10^{-12}$	$4.76 \times 10^{-13}$

To decide whether choice 1 or choice 2 is correct, the fluorescence intensity ratio at 309 nm to 314 nm in argon at dew point -14.0°C was measured. The ratio  $I(309)/I(314)$  is  $1.99 \pm 0.25$ . Using this ratio and various  $k$ 's from each choice,  $k_{10Ar}$  can be calculated according to equation 56. It turns out that only choice 1 can produce a reasonable value of  $k_{10Ar}$ . Choice 2 results in a  $k_{10Ar}$  larger than the value of  $k_{Q1Ar} + k_{10Ar}$ . Thus the identity of A and B in Figure 24 is determined.

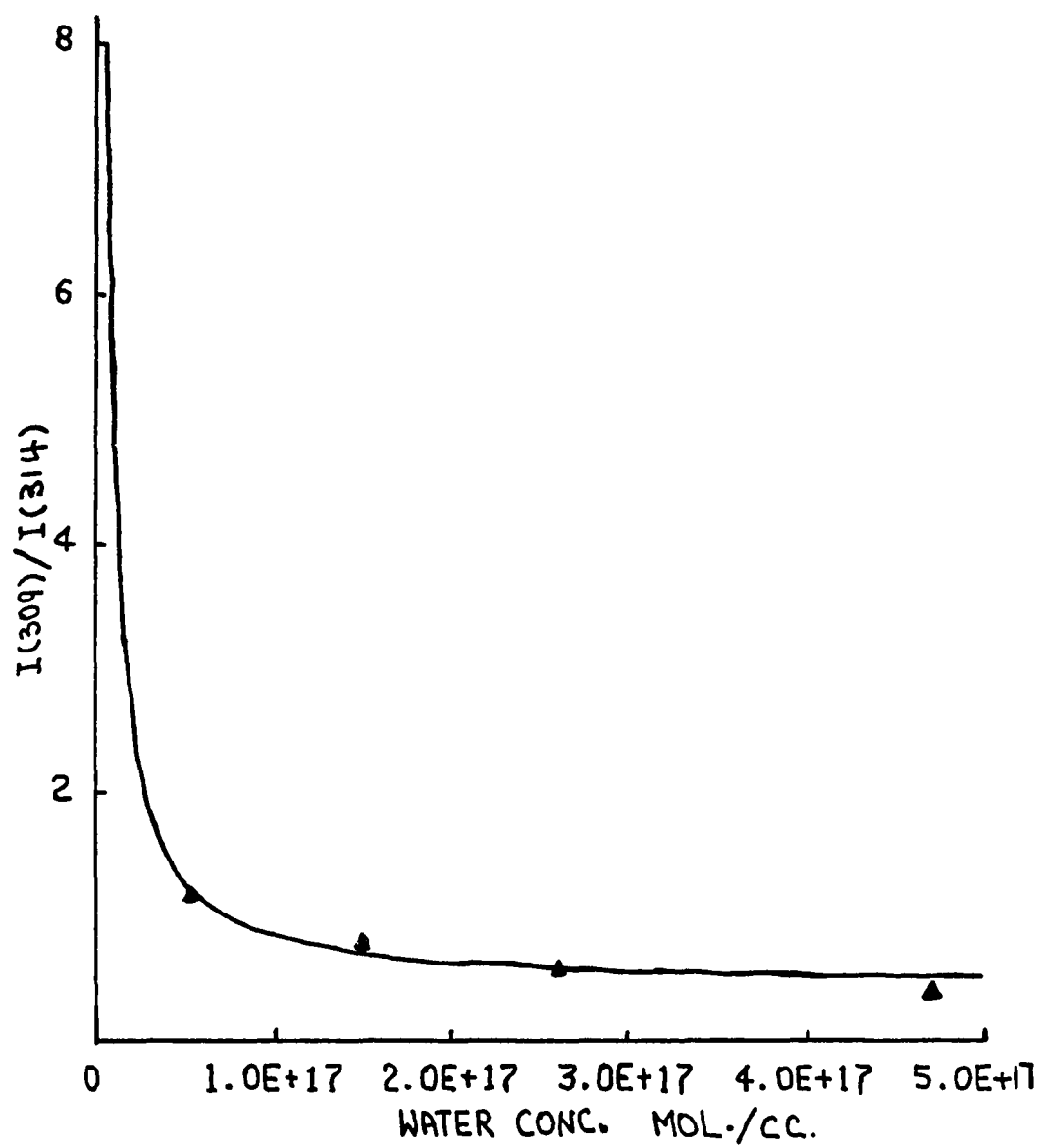


Figure 26 Ratio of fluorescence intensity at 309nm to that at 314nm in helium as a function of water concentration.

To further confirm which is A and which is B, the fluorescence decay at 314 nm in argon at dew point  $-7.0^{\circ}\text{C}$  was measured. Fluorescence at 314 nm is due to the decay from the  $v'=1$  state, therefore the decay constant must be A. The result ( $A=0.135 \times 10^9$ ) indicated that A indeed was the larger of the two values measured at 309 nm (see Table VII).

The analysis of the data follows the logic discussed in the Minor Details section of Chapter II. The deduction falls into two sections: A's and B's of argon plus water and A's and B's of nitrogen plus oxygen.

Argon plus water:

$$\text{B: slope} = k_{QO\text{H}_2\text{O}} = 7.9 \pm 0.47 \times 10^{-10}$$

$$\text{intercept} = k_{QO\text{Ar}}[\text{Ar}] = 1.17 \pm 0.34 \times 10^7$$

$$k_{QO\text{Ar}} = \frac{1.17 \pm 0.34 \times 10^7}{2.46 \times 10^{19}} = 0.48 \pm 0.14 \times 10^{-12}$$

$$\text{A: slope} = k_{Q1\text{H}_2\text{O}} + k_{10\text{H}_2\text{O}} = 4.88 \pm 0.44 \times 10^{-10}$$

Based on the measurement of the fluorescence at 314 nm and 309 nm in Helium, we have

$$k_{10\text{H}_2\text{O}} / k_{QO\text{H}_2\text{O}} = 0.43 \pm 0.07$$

$$\begin{aligned} k_{10\text{H}_2\text{O}} &= 0.43 \pm 0.07 \times 7.9 \pm 0.47 \times 10^{-10} \\ &= 3.4 \pm 0.59 \times 10^{-10} \end{aligned}$$

$$\begin{aligned} k_{Q1\text{H}_2\text{O}} &= (4.88 \pm 0.44 - 3.4 \pm 0.59) \times 10^{-10} \\ &= 1.48 \pm 0.74 \times 10^{-10} \end{aligned}$$

$$\text{intercept} = (k_{Q1\text{Ar}} + k_{10\text{Ar}})[\text{Ar}] = 1.41 \pm 0.03 \times 10^8$$

$$= k_{Q1Ar} + k_{10Ar} = 5.73 \pm 0.12 \times 10^{-12}$$

Based on the measurement of I(309)/I(314) at dew point -14.0C in Argon, we have

$$\frac{k_{10H_2O}[H_2O] + k_{10Ar}[Ar]}{k_{Q0H_2O}[H_2O] + k_{Q0Ar}[Ar]} = 1.99 \pm 0.25$$

$$\text{At dew point } -14.0C, [H_2O] = 0.48 \times 10^{17}$$

$$k_{10H_2O}[H_2O] = 3.4 \pm 0.59 \times 10^{-10} \times 0.48 \times 10^{17} \\ = 1.63 \pm 0.28 \times 10^7$$

$$k_{Q0H_2O}[H_2O] = 7.9 \pm 0.47 \times 10^{-10} \times 0.48 \times 10^{17} \\ = 3.79 \pm 0.23 \times 10^7$$

$$k_{Q0Ar}[Ar] = 4.8 \pm 1.4 \times 10^{-13} \times 2.46 \times 10^{19} \\ = 1.18 \pm 0.34 \times 10^7$$

$$k_{10H_2O}[H_2O] + k_{10Ar}[Ar] = 4.97 \pm 0.34 \times 10^7$$

$$k_{10Ar} = 3.36 \pm 0.59 \times 10^{-12}$$

$$k_{Q1Ar} = 5.74 \pm 0.12 \times 10^{-12} - 3.36 \pm 0.59 \times 10^{-12}$$

$$k_{Q1Ar} = 2.37 \pm 0.6 \times 10^{-12}$$

Nitrogen plus oxygen:

$$B: \text{ slope } = k_{Q0O_2} = 2.65 \pm 0.57 \times 10^{-10}$$

$$\text{intercept} = k_{Q0N_2}[N_2] + k_{Q0H_2O}[H_2O] \\ = 2.06 \pm 0.2 \times 10^8$$

$$\text{At dew point } -16.0C; [H_2O] = 0.4 \times 10^{17}$$

$$k_{Q0H_2O}[H_2O] = 7.9 \pm 0.47 \times 10^{-10} \times 0.4 \times 10^{17} \\ = 3.16 \pm 0.19 \times 10^7$$

$$k_{Q0N_2}[N_2] = (2.06 \pm 0.2 - 0.316 \pm 0.09) \times 10^8 \\ = 1.74 \pm 0.20 \times 10^8$$

$$k_{QON_2} = 0.71 \pm 0.08 \times 10^{-11}$$

A:  $\text{slope} = k_{IOO_2} + k_{QIO_2} = 1.83 \pm 0.43 \times 10^{-9}$

Present results only allow us to obtain

$$k_{IOO_2} + k_{QIO_2} = 1.83 \pm 0.43 \times 10^{-9}$$

$$\begin{aligned} \text{intercept} &= (k_{ION_2} + k_{QIN_2})[N_2] + (k_{IOH_2O} + k_{QIOH_2O})[H_2O] \\ &= 2.18 \pm 0.16 \times 10^9 \end{aligned}$$

At dew point  $-16.0^\circ\text{C}$ ;  $[H_2O] = 0.4 \times 10^{17}$

$$\begin{aligned} (k_{IOH_2O} + k_{QIOH_2O})[H_2O] &= 0.4 \times 10^{17} \times 4.88 \pm 0.44 \times 10^{-10} \\ &= 1.95 \pm 0.18 \times 10^7 \end{aligned}$$

$$\begin{aligned} (k_{ION_2} + k_{QIN_2})[N_2] &= (2.18 - 0.0195) \pm 0.16 \times 10^9 \\ &= 2.16 \pm 0.16 \times 10^9 \end{aligned}$$

$$k_{ION_2} + k_{QIN_2} = 8.78 \pm 0.65 \times 10^{-11}$$

Since  $k_{QIN_2} < k_{ION_2}$ , we assume  $k_{QON_2} = k_{QIN_2}$

$$\begin{aligned} k_{ION_2} &= 8.78 \pm 0.65 \times 10^{-11} - 0.76 \pm 0.08 \times 10^{-11} \\ &= 8.07 \pm 0.65 \times 10^{-11} \end{aligned}$$

### Final Results

The results are tabulated in Tables XIII to XVI together with the available literature values. The literature values are mostly those taken from references 24 and 39.

Rate constants of argon and water are in good agreement with the low pressure literature values.

Nitrogen results are smaller than the more recent reported values. The measured  $k_{\text{QO}}$  ( $0.71 \pm 0.08 \times 10^{-11}$ ) agrees with the values of Kley and Welge(40) and Becker and Haaks(39). These two groups also produced OH radicals by photolysis of water. But, further checking with the values collected by Schofield(24) shows that, since 1974, the reported values, primarily due to German and Lengel and Crosley, have been around  $3.0 \times 10^{-11}$  which is about 4 times larger than our measured value. One possible explanation is that their experiments (23,24,41,44) generated OH by the reaction of  $\text{H} + \text{NO}_2$ . The gas mixtures might be contaminated by untitrated  $\text{NO}_2$  and H and the product NO. The  $\text{NO}_2$  by itself is about 10 times more effective than nitrogen. It only takes 20% of the total pressure to double the quenching rate. The other support to this speculation is that the measurements(39,40) utilizing photolysis of water at low pressure also produce lower values. The low value of the measured vibrational relaxation constant can also be explained by the same



TABLE XIII  
RATE CONSTANTS FOR ARGON ( $10^{-11}$  CC MOLECULE $^{-1}$  S $^{-1}$ )

$k_{QAr}$	Exp. Temp. K	Exp. Pressure	Comment	Ref.
0.02	295	0.5-5.3 kPa.	Photolysis of water	cited in 24
$<2$	850-1500	0.4-0.8 kPa.	C <sub>2</sub> H <sub>2</sub> /O <sub>2</sub> low pressure flames.	3
$<0.007$	295	0.67 kPa.	Flow cell. Kr 123.6 nm photolysis of water.	40
0.1	295	0.013 kPa.	Kr 123.6 nm pulsed photolysis.	39
$<0.6$	298	0.3 kPa.	Discharge flow system. OH from H+NO <sub>2</sub> . OH source induced fluoresc- ence.	41
0.05	295	0.13 kPa.	OH for H+NO <sub>2</sub> . Dye laser fluorescence.	cited in 24
0.034	300	not spec- ified-low	OH from O <sub>3</sub> /H <sub>2</sub> photolysis, dye laser fluorescence.	43
$<0.004$	300	0.27 kPa	121.5 nm pulsed pho- tolysis of water. High rotational levels.	cited in 24
0.048 $\pm$ 0.014	297	101 kPa.	Photolysis of water, dye laser fluorescence.	This work

TABLE XIII CONTINUED

$k_{\text{Q1Ar}}$	Exp. Temp. K	Exp. Pressure	Comment	Ref.
0.4	300	0.27 kPa.	121.5 nm pulsed photolysis of water. High rotational levels.	cited in 24
$0.24 \pm 0.6$	297	101 kPa.	Photolysis of water, dye laser fluorescence.	This work
$k_{\text{10Ar}}$	Exp. Temp. K	Exp. Pressure	Comment	Ref.
0.29	320	0.15 kPa.	OH from $\text{H} + \text{NO}_2$ . Pulsed dye laser.	cited in 24
0.13	300	unspecified	OH from $\text{O}_3/\text{H}_2$ photolysis. Questionable data ( ref. 1)	43
$0.34 \pm 0.06$	297	101 kPa.	Photolysis of water. Pulsed dye laser fluorescence.	This work

TABLE XIV  
RATE CONSTANTS FOR WATER ( $10^{-10}$  CC MOLECULE $^{-1}$  S $^{-1}$ )

$k_{\text{QOH}_2\text{O}}$	Exp. Temp. K	Exp. Pressure	Comment	Ref.
2.9	295	0.67 kPa.	Kr 123.6 nm photolysis of water.	40
3.5	298	0.3 kPa.	OH from $\text{H}+\text{NO}_2$ . OH source induced fluorescence.	41
4.5	295	0.013 kPa.	Kr 123.6 nm pulsed photolysis of water or methanol. Reports $k_{10}+k_{\text{Q1}} = 4.0$	39
5.0	300	$\leq 0.5$ kPa.	Kr 123.6 nm photolysis of water.	42
5.6	300	0.27 kPa.	121.5 nm pulsed photolysis. High rotational levels.	cited in 24
6.1	315	0.007 kPa.	Static system, 200 eV e-beam.	5
9.2	300	0.021 kPa.	Narrow band photolysis of water. High rotational level.	cited in 24
4.0	300	3.3 kPa.	Microwave discharge of water. Pulsed dye laser.	23
$7.9 \pm 0.47$	297	101 kPa.	Photolysis of water. Pulsed dye laser.	This work

TABLE XIV CONTINUED

$k_{Q1H_2O}$	Exp. Temp. K	Exp. Pressure	Comment	Ref.
4.0	295	0.013 kPa.	Kr 123.6 nm pulsed photolysis of water or methanol. $k_{10} + k_{Q1}$ .	39
5.6	300	0.27 kPa.	121.5 nm pulsed photolysis of water. High rotational levels.	cited in 24
9.2	300	0.021 kPa.	Narrow band photolysis of water. High rotational levels.	cited in 24
$1.48 \pm 0.74$	297	101 kPa.	Photolysis of water. Pulsed dye laser.	This work
$k_{10H_2O}$	Exp. Temp. K	Exp. Pressure	Comment	Ref.
$3.4 \pm 0.59$	300	101 kPa.	Photolysis of water. Pulsed dye laser.	This work

TABLE XV  
RATE CONSTANTS FOR NITROGEN ( $10^{-11}$  CC MOLECULE $^{-1}$  S $^{-1}$ )

$k_{\text{QON}_2}$	Exp. Temp. K	Exp. Pressure	Comment	Ref.
0.05	295	0.3-5.3 kPa.	Photolysis of water.	cited in 24
4.0	300	$\leq 0.5$ kPa.	Kr 123.6 nm photolysis of water.	42
0.51	295	0.67 kPa.	Kr 123.6 nm photolysis of water.	40
1.0	295	0.013 kPa.	Kr 123.6 nm pulsed photolysis of water or methanol.	39
1.6	298	0.3 kPa.	OH from H+NO <sub>2</sub> , dye laser fluorescence.	41
4.3	320	0.13 kPa.	OH from H+NO <sub>2</sub> , dye laser fluorescence.	44
2.3	300	unspecified	OH from O <sub>3</sub> /H <sub>2</sub> photolysis, dye laser fluorescence.	43
2.6	295	0.13 kPa.	Flow system, OH from H+NO <sub>2</sub> , dye laser fluorescence.	33
1.6	300	1 kPa.	OH from H+NO <sub>2</sub> . Pulsed dye laser fluorescence.	cited in 24
4.2	320	0.15 kPa.	OH from H+NO <sub>2</sub> . Pulsed dye laser fluorescence.	47
3.1	300	3.3 kPa.	Microwave discharge of water, dye laser fluorescence.	23
$0.71 \pm 0.08$	297	101 kPa.	Photolysis of water. Dye laser fluorescence.	This work

TABLE XV CONTINUED

$k_{10N_2}$	Exp. Temp. K	Exp. Pressure	Comment	Ref.
18.3	320	0.15 kPa.	OH from $H+NO_2$ . Pulsed dye laser fluorescence.	47
15.0	295	0.13 kPa.	OH from $H+NO_2$ . Dye laser fluorescence.	33
$8.07 \pm 0.65$	297	101 kPa.	Photolysis of water. Pulsed dye laser fluorescence.	This work

TABLE XVI  
RATE CONSTANTS FOR OXYGEN ( $10^{-11}$  CC MOLECULE $^{-1}$  S $^{-1}$ )

$k_{QO_2}$	Exp. Temp. K	Exp. Pressure	Comment	Ref.
10.4	295	0.13 kPa.	Flow system, OH from H+NO <sub>2</sub> . Dye laser fluorescence.	33
30	1500-1790 <sup>#</sup>	101 kPa.	H <sub>2</sub> /O <sub>2</sub> /N <sub>2</sub> /Ar atmospheric pressure flames.	6
8.0	800-1500 <sup>#</sup>	0.4-0.8 kPa.	C <sub>2</sub> H <sub>2</sub> /O <sub>2</sub> low pressure flames.	3
9.9	300	3.3 kPa.	Microwave discharge of water. Dye laser fluorescence.	23
26.5±5.7	297	101 kPa.	Photolysis of water. Pulsed dye laser fluorescence.	This work
$k_{Q1O_2}$	Exp. Temp. K	Exp. Pressure	Comment	Ref.
13.0	295	0.13 kPa.	OH from H+NO <sub>2</sub> , dye laser fluorescence.	33
183±43	297	101 kPa.	Photolysis of water. Pulsed dye laser fluorescence. * $k_{elect.}$ + $k_{vibr.}$	This work

<sup>#</sup> Range of applicable temperature.

TABLE XVI CONTINUED

$k_{100_2}$	Exp. Temp. K	Exp. Pressure	Comment	Ref.
1.5	295	0.13 kPa.	Flow system, OH from H+NO <sub>2</sub> , dye laser fluor- escence.	33
183*	297	101 kPa.	OH from photolysis of water. Pulsed dye laser fluorescence. * $k_{100_2} + k_{Q10_2}$	This work



arguments. Of course, the other possibility is the pressure effect.

Wang and Davis measured the ratio of  $k_{\text{QOH}_2\text{O}}$  to  $k_{\text{QON}_2}$  at atmospheric pressure(22). The reported ratio is  $44 \pm 14$ .  $k_{\text{QON}_2}$  can be calculated by taking  $k_{\text{QOH}_2\text{O}}$  to be  $7.9 \pm 0.47 \times 10^{-10}$ . The result is  $1.8 \pm 0.6 \times 10^{-11}$  which is at the lower end of the more recent literature values.

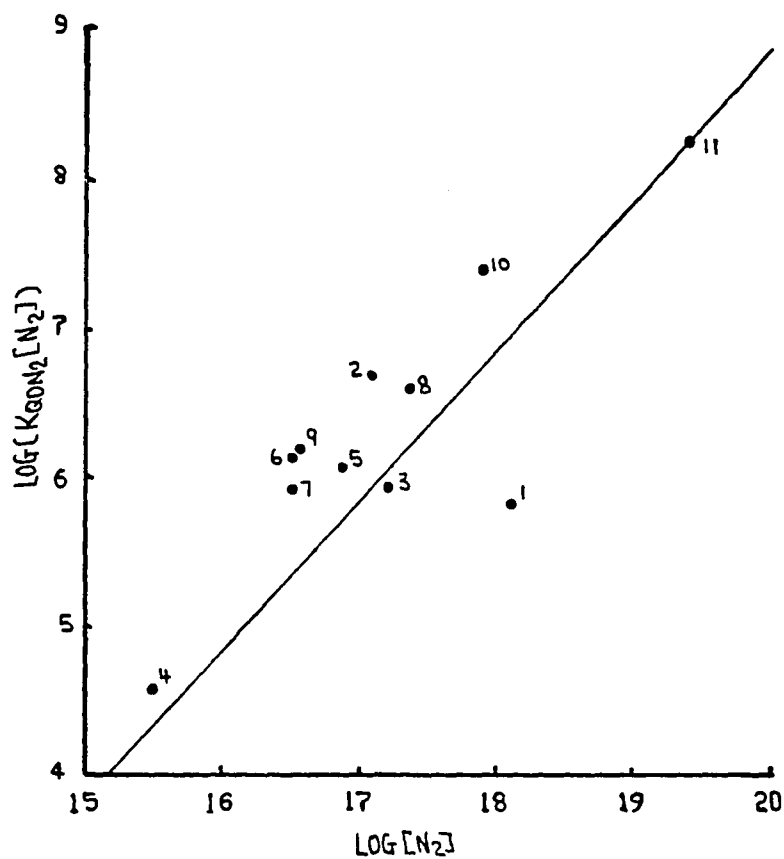
Selzer and Wang(23) remeasured the values for nitrogen again in 1979. This time their experiments were done at low pressure and OH was generated by passing moist gases through a microwave discharge. The reported value of  $k_{\text{QON}_2}$  was  $3.1 \times 10^{-11}$  which agreed with the higher values in the literature. Now here are two experiments performed by the same group at two different pressures and their results disagree. Is it an indication of pressure dependence of the rate constants? At this point in time, it would be naive to draw such a conclusion, but at least such a possibility should be considered.

The rate constants of oxygen as expected, are fast. The value of  $k_{\text{QOO}_2}$  is about twice the literature values and  $k_{\text{QIO}_2} + k_{\text{IOO}_2}$  is about 10 times larger. If we assume  $k_{\text{QI}} = k_{\text{QO}}$ , the  $k_{\text{IOO}_2}$  will be one hundred times larger than the only available literature value! It may be possible that the deactivation by oxygen molecules is more complicated than the simple explanation offered by the hard sphere collision model. Ozone interference was ruled

out by the experiments to be discussed in Chapter VI. Although the rate constants are higher than the hard-sphere collision rate, a rate constant ( $\text{ArF}^* + \text{Xe} \rightarrow \text{XeF}^* + \text{Ar}$ ) as high as  $4.5 \times 10^{-9}$  cc molecule $^{-1}$  sec $^{-1}$  has been reported (21).

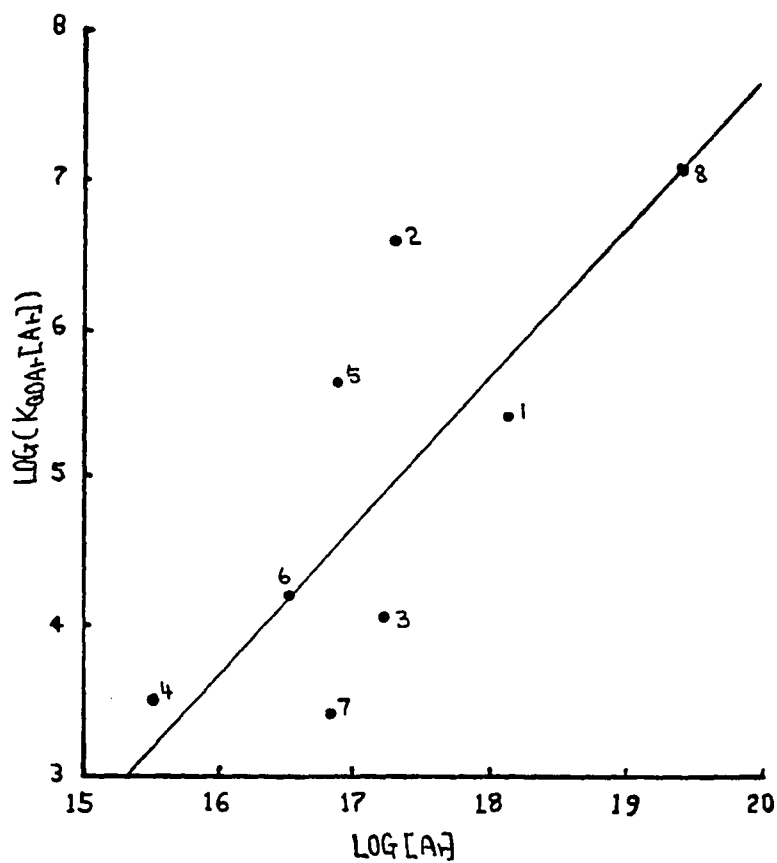
In order to compare our rate constants with the literature values in the context of the pressure under which they are measured, we use a novel way to present the literature values and the measured values graphically. Figure 28 is a plot of  $\log(k_{\text{QOAr}}[\text{Ar}])$  against  $\log[\text{Ar}]$ . Figure 27 is a plot of  $\log(k_{\text{QON}_2}[\text{N}_2])$  against  $\log[\text{N}_2]$ . The  $[\text{N}_2]$  and  $[\text{Ar}]$  refer to the pressure under which the experiment is carried out. The straight line shown has its slope equal to 1 and its intercept equal to  $\log k_{\text{QOAr}}$  or  $\log k_{\text{QON}_2}$  obtained by this experiment. Figures 29 and 30 show similar plots for the  $k_{\text{QO}}$  of water and oxygen. The reason for presenting the values in logarithmic scale is because the range of pressure covered by the values varies over two orders of magnitude. It would be difficult to show all the points clearly in linear scale over such a wide range of pressure. In addition to showing all the points, the plots also show that the three-body collision contribution is not significant at atmospheric pressure. Were the three-body contribution significant, the points would curve upward rather than lie in a straight line.

Since the quantity measured is  $k_{\text{QO}}[\text{M}]$  and we wish to



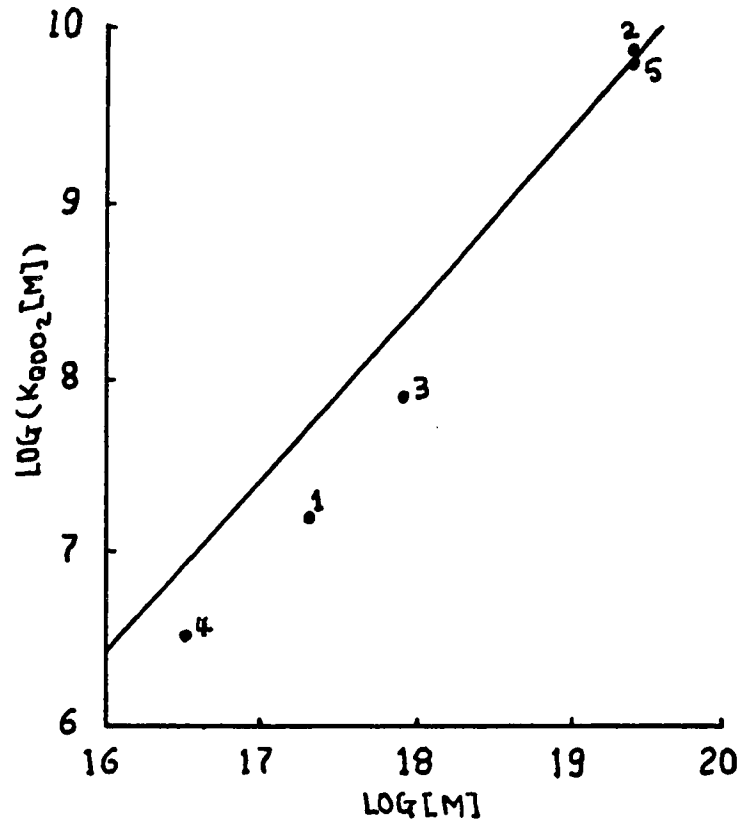
	Ref.		Ref.		Ref.
1	cited in 24	2	42	3	40
4	39	5	41	6	44
7	33	8	cited in 24	9	47
10	23	11	this work		

Figure 27 Plot of  $\log(k_{QON_2}[N_2])$  against  $\log[N_2]$ . The straight line has its slope equal to 1 and its intercept equal to  $\log(k_{QON_2})$  measured in the experiment.



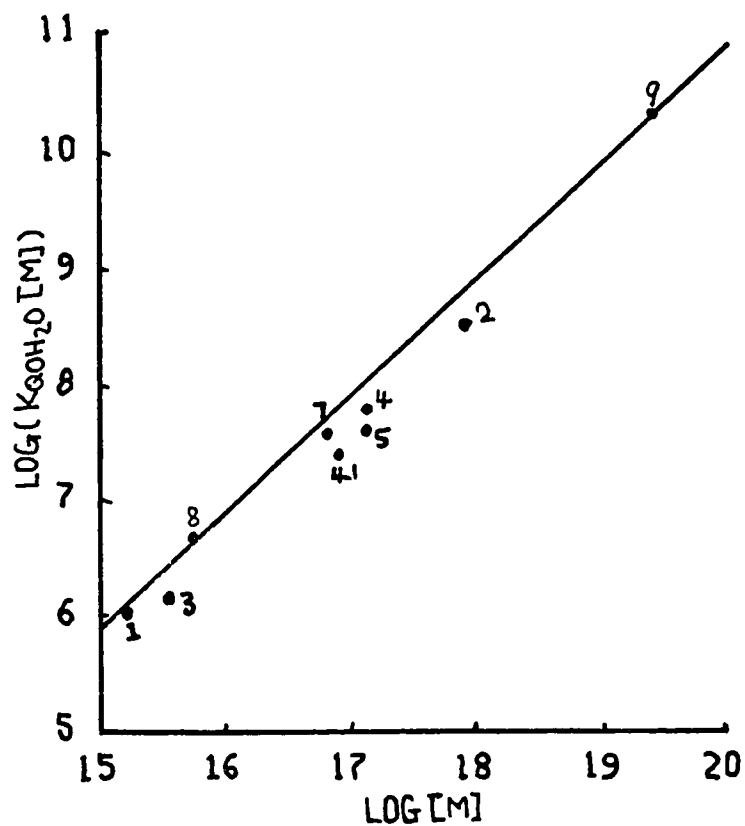
Ref.	Ref.	Ref.
1 cited in 24	2 3	3 40
4 39	5 41	6 cited in 24
7 cited in 24	8 this work	

Figure 28 Plot of  $\log(k_{QOAr}[Ar])$  against  $\log[Ar]$ . The straight line has slope of 1 and intercept of  $\log(k_{QOAr})$  measured in the experiment.



	Ref.		Ref.		Ref.
1	3	2	6	3	23
4	33	5	This work		

Figure 29 Plot of  $\log(k_{QO_2} [M])$  against  $\log[M]$ . The straight line has slope of 1 and intercept of  $\log(k_{QO_2})$  measured in the experiment.



	Ref.		Ref.		Ref.
1	5	2	23	3	39
4	39	5	40	6	41
7	cited in 24	8	cited in 24	9	This work

Figure 30 Plot of  $\log(k_{QOH_2O}[M])$  against  $\log[M]$ . The straight line has slope of 1 and intercept of  $\log(k_{QOH_2O})$  measured in the experiment.

obtain a reliable proportionality constant (e.g. rate constant), it is a common practice to make measurements under practical conditions which are as widely distributed as possible or at least over the range of conditions under which the rate constant is to be utilized. The reason for this is that the errors associated with the dependent parameter are directly proportional to the distance of extrapolation. If we extrapolate the literature values out to atmospheric pressure, the deactivation rate will have large uncertainty. This is one argument for measuring the rate constant at atmospheric pressure. Figure 31 illustrates this point. The figure is a plot of the least squares fit to the literature values,  $k_{\text{OON}_2}[\text{N}_2]$ , in Table XV as a function of their corresponding experimental pressure. We can see that the least squares error due to extrapolation is large. The contribution of our measurement is both to provide a value and to narrow the error at atmospheric pressure.

Finally, let's consider the question of reproducibility of the experimental results. The experiment of argon plus water at dew point  $-7.0^\circ\text{C}$  was done after the experiments of nitrogen and oxygen. That is about one month after the other argon plus water experiments were performed. The question that the low value of nitrogen is due to the change in the detection system can be ruled out, since the last argon plus water

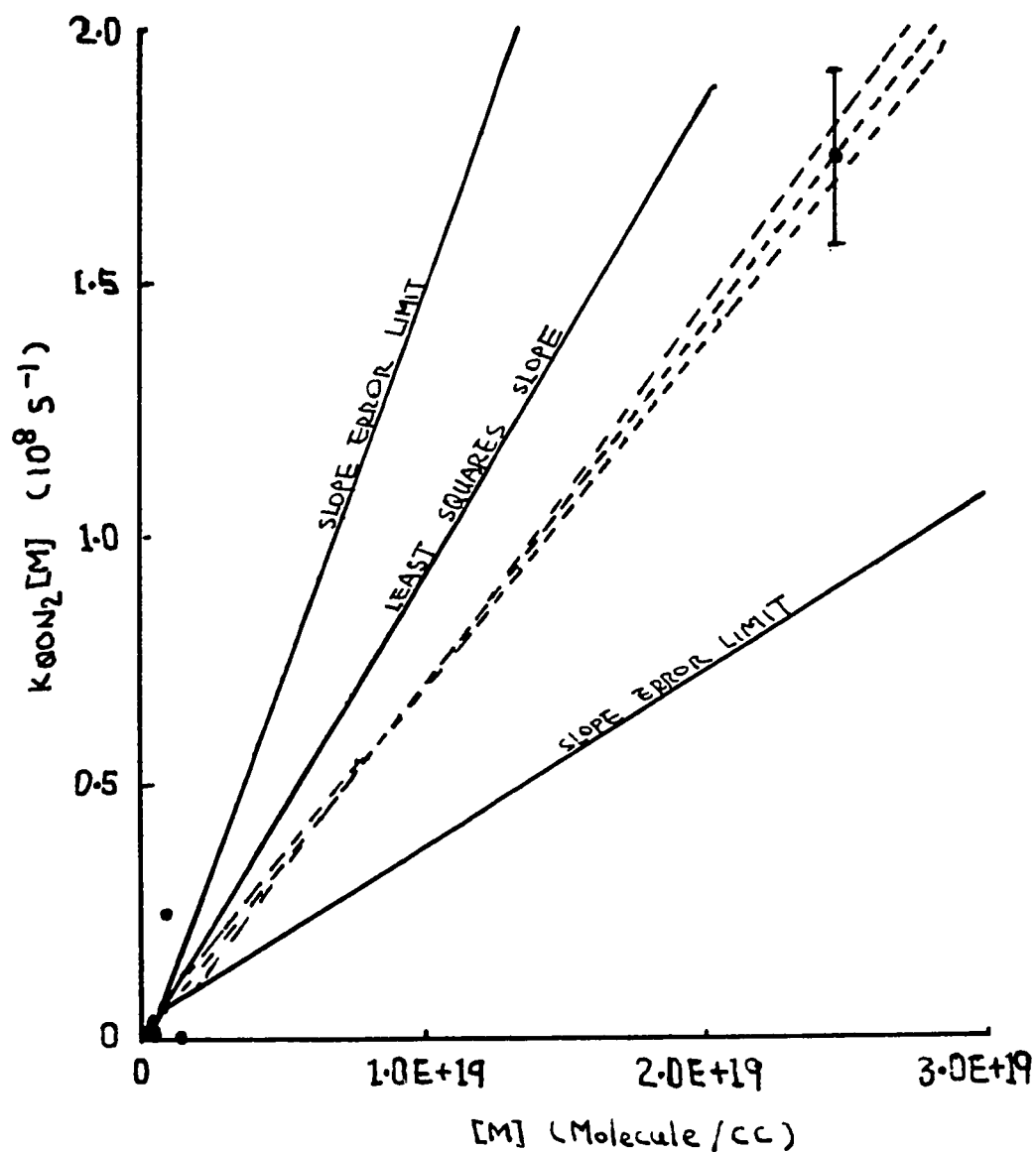


Figure 31 Linear least squares fit to the literature values,  $k_{QON_2}[M]$ , in Table XV as a function of their corresponding experimental pressure. The solid lines do not include our own experimental value. The broken lines include our own experimental result.



at dew point  $-7.0^{\circ}\text{C}$  experiment agreed with the earlier results. In fact, repeated experiments with nitrogen showed no inconsistency with the earlier results.

## CHAPTER V

### ERROR ASSESSMENT

This chapter assesses the uncertainty of our method and the limitation of our instruments. We will discuss the systematic errors due to the approximation by equation 26 and random errors due to the counting statistics. Finally, we will estimate the errors caused by the instability of our instruments.

#### Systematic and Random Errors

The discrete convolution (equation 26) is only an approximation. Its departure from the exact solution (equation 27) has to be reckoned with. Since the accuracy of the approximation depends on the step size (MCA resolution), we assessed the effects of the step size on the accuracy. The adopted strategy to check its accuracy was to simulate the input function by a Gamma function,

$$f(t) = \alpha t^2 \text{EXP}(-0.6t).$$

The value of  $\alpha$  was chosen so that the peak height was about 500, which is similar to real experimental results. Then the convolution was integrated in closed form with  $A=2.0 \text{ ns}^{-1}$  and  $B=0.4 \text{ ns}^{-1}$ . Discrete values with various

step sizes were then obtained for these  $f(t)$  and  $h(t)$ . The simulated discrete data,  $f(t)$  and  $h(t)$ , were evaluated for values of A and B with the simplex program. Table XVII shows the results. Evidently, larger step size introduces larger errors. In actual experiments, the time range of the MCA was chosen for maximum resolution, while capturing the essential features of the decay curve. For values of A and B comparable to Table XVII, 0.1 ns resolution was used. Thus we expect about 1% error as a result of the discrete convolution. This is small relative to the other errors. The idea is demonstrated by the time scales used in Figures 13 to 22.

Effects of random noise on the accuracy of our approximation were also investigated. The method followed the procedure above, except random noise of various amplitudes was added to the discrete data,  $f(t)$  and  $h(t)$ , before they were evaluated by the simplex program. Since counting statistics predicts that the noise is equal to the square root of the count, we varied the amplitude of the noise by changing the count of each channel and took the square root of the count as the noise. Thus we achieved varying noise amplitude while adhering to the square root relation. Results (Table XVIII) show that a minimum signal to noise ratio of 10 (peak count of 100) is required for a reliable evaluation of A and B. In actual experiments, the peak counts are larger than 100. Thus,

TABLE XVII  
EFFECTS OF CHANNEL RESOLUTION  
ON THE ACCURACY OF EQUATION 26

Resolution (ns)	A	% Error	B	% Error
0.25	2.08	+4.0	0.398	-0.4
0.20	2.05	+2.3	0.399	-0.2
0.15	2.02	+1.0	0.3996	-0.1
0.10	2.01	+0.55	0.399	-0.05
True value	2.00	--	0.400	--

TABLE XVIII  
EFFECTS OF SIGNAL/NOISE RATIO ON  
THE ACCURACY OF EQUATION 26

noise/ signal at the peak channel	A	% Error	B	% Error
5/25	*	*	*	*
10/100	1.94	-3.0	0.403	+0.75
20/400	1.99	-0.1	0.401	+0.25
30/900	2.01	+0.5	0.399	-0.25
True Value	2.00	--	0.400	--

\* Simplex program does not converge.

less than 3% error was introduced by limiting the length of the experiment.

#### Convergence Test

The idea behind the convergence test was to see how many counts had to be accumulated to give A and B with acceptable errors and what was the maximum count beyond which little was gained due to the errors of the other sources.

The strategy was to sample the fluorescence profile after every 1000 additional counts had been added. the experiment was carried out on the case of nitrogen plus 5% oxygen. The A's and B's were extracted from these 20 progressively growing fluorescence profiles and plotted as a function of increasing counts in Figure 32.

The results show that initially the values do approach a certain value as the count increases. Beyond a surprisingly low 10,000 counts, the convergence is overwhelmed by the fluctuation due to other error sources. Notice that the values of A and B are comparatively large in this experiment.

Figure 32 also shows similar plots of A's and B's for argon with water concentration at dew point about -16.0C. From this figure, it appears that the values of A don't converge. In the case where the A and B values are small, the fluorescence curve has a large area. For a large area, more counts are needed to reach the point

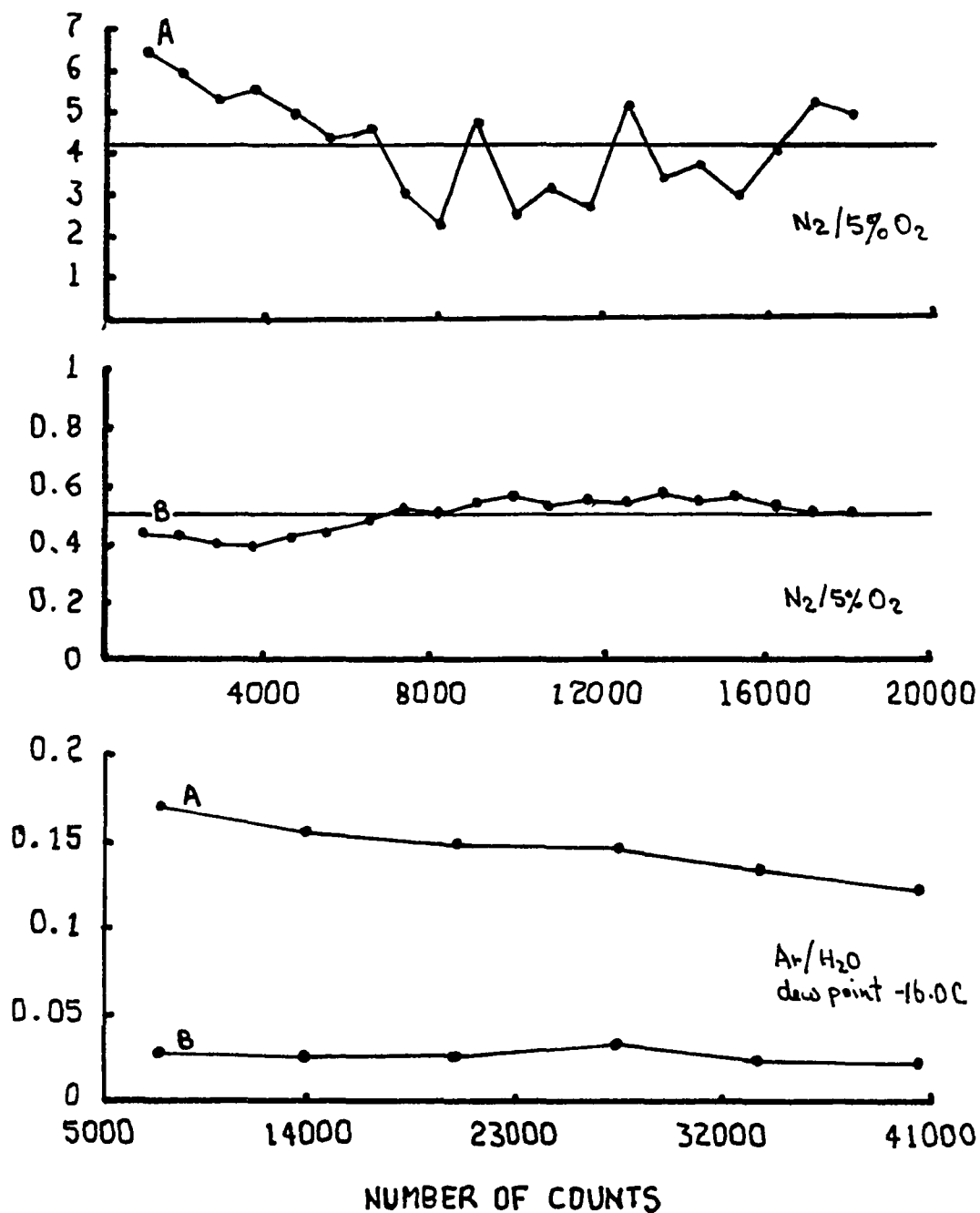


Figure 32 Values of A's and B's as a function of cumulative count in nitrogen/5% oxygen and argon/water a dew point  $-16.0C$ .

where the other fluctuations take over. Apparently this curve shows that the experiment has not passed the critical point yet.

Figure 33 is a plot of  $\log(\text{error})$  against  $\log(\text{count})$  of the results in Table XI. According to counting statistics, such a plot should result in a straight line with slope equal to  $-0.5$ . Due to the way of defining the error ( $\sigma$ ), the error is equal to  $1/\sqrt{N}$ , where  $N$  is the count. A linear least squares fit produces a slope of  $-0.674$ , which is somewhat greater than  $-0.5$ . No good explanation can be offered at the present time, but at least the error does decrease as the count increases.

### Timing Errors

There are two sources of timing errors: the inherent timing uncertainty and the long term drift of the detection system. The inherent uncertainty refers to the uncertainty in the timing circuits of the MCA and the jitters in the start and stop pulses. The constant fraction discriminator is supposed to have minimized the jitters in the stop pulses. The largest errors are attributed to the high-speed photodiode that generated the start pulses.

To check the timing uncertainty of the MCA, a pulse was generated by a photodiode and fed into the start input of the MCA. The same pulse was delayed by a fixed length of cable (approximately 40 ns) which terminated at the

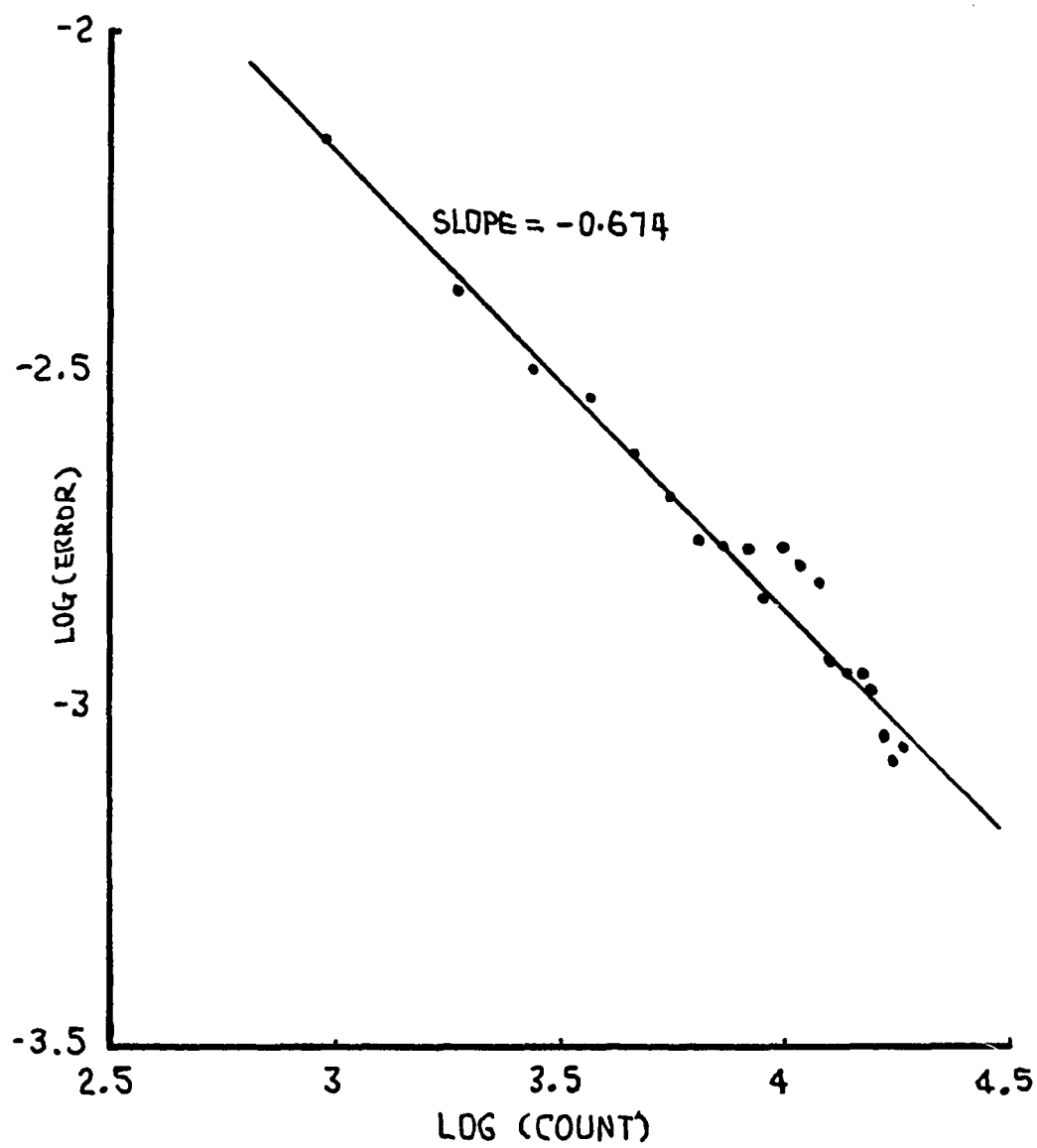


Figure 33 Plot of  $\log(\text{error})$  versus  $\log(\text{count})$  of the experiment on OH fluorescence in nitrogen.



stop input. After 1,550 pulses, the spread of the delay times recorded by the MCA was analysed to have a standard deviation of about 0.08 ns. Figure 34 shows the result as it was displayed on an oscilloscope.

To check the uncertainty of the photodiode, two similar photodiodes looked at the same reflection of the laser. One photodiode generated a start and the other generated a stop pulse into the MCA. The stop pulse was routed through a longer cable to create a delay. After 18,000 laser pulses, the spread of the delay was analysed to have a standard deviation of about 0.2 ns (Figure 35). Since 0.2 ns is much larger than the 0.08 ns, the overall timing uncertainty of the detection system was estimated to be 0.2 ns.

Due to the low repetition rate of the laser system, usual experiments took several days while long experiments took over a week to complete. This long experimental time introduced errors due to the long-term detection system drift. The system drift essentially refers to the change in the timing circuits. For example, if we apply a fixed delay between the start and the stop pulse, the time circuits may measure the delay to be 3.3 ns. A few days later, the same delay may be measured to be 3.0 ns. This kind of drift will shift the whole laser, because the start pulse is always triggered by the laser itself. The response of the system to daily room temperature change

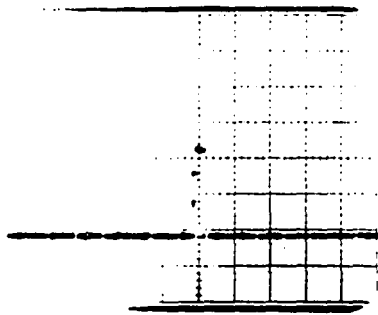


Figure 34 Uncertainty check of the MCA. Time scale is 0.1 ns per channel.

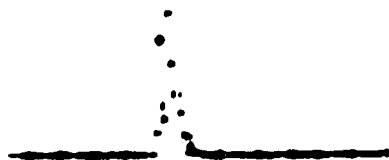


Figure 35 Uncertainty check of the high-speed photodiode.  
Time scale is 0.1 ns per channel.

was one aspect of such kind of long-term drift.

The long term drift was tested by measuring the laser profile over a period of 12 days. Then the misalignment of the recorded laser profiles was attributed to the drifting of the whole detection system. Whether these errors were due to the constant fraction discriminator, the MCA or the photodiode were unknown, although it was most likely the photodiode. The misalignment is shown in Figures 36 to 38.

After the detection system has warmed up for three days, the spread of the half-heights is about 0.7 ns. The results indicate that the system, after the first three days of warming up, does not drift toward one direction but rather shifts back and forth. This led to the conclusion that the fluctuation is 0.3 ns and to the policy of leaving the detection system on continuously. It was most likely that the shifts were due to the effects of change in room temperature on the photodiode. In Figure 38, the variation of the laser half-width is also shown. The variation of the laser half-width is not as significant as the time shift.

The next logical step is to estimate the maximum effect of this 0.3 ns shift on the values of A and B. As expected, the errors due to this shift depended on the sizes of A and B. Thus the testing procedure used the practically observable extreme values of A and B.

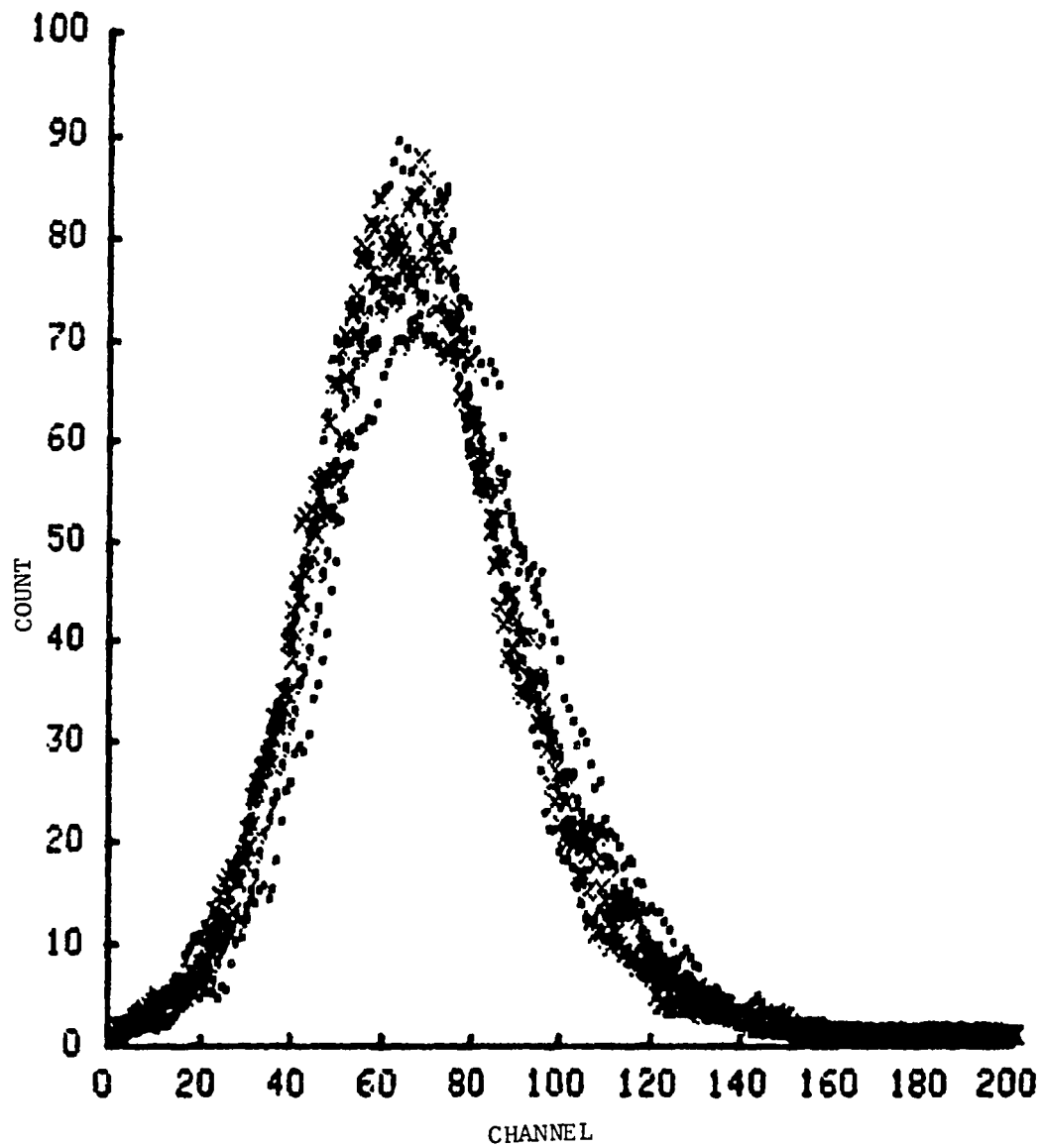


Figure 36 Misalignment of the laser profiles showing the drift of the detection system.

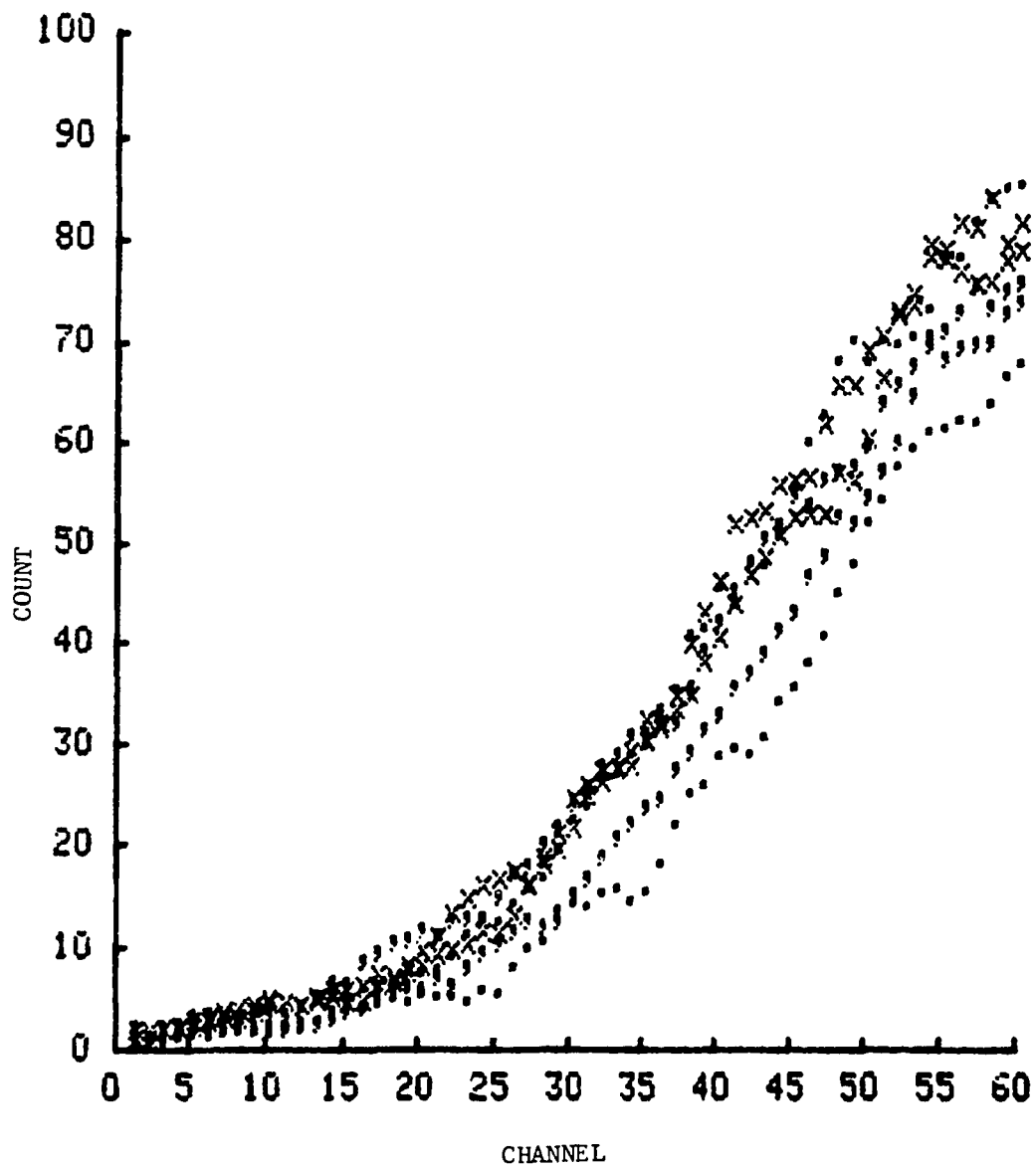


Figure 37 Misalignment of the laser profiles showing the rising portions of the profiles.

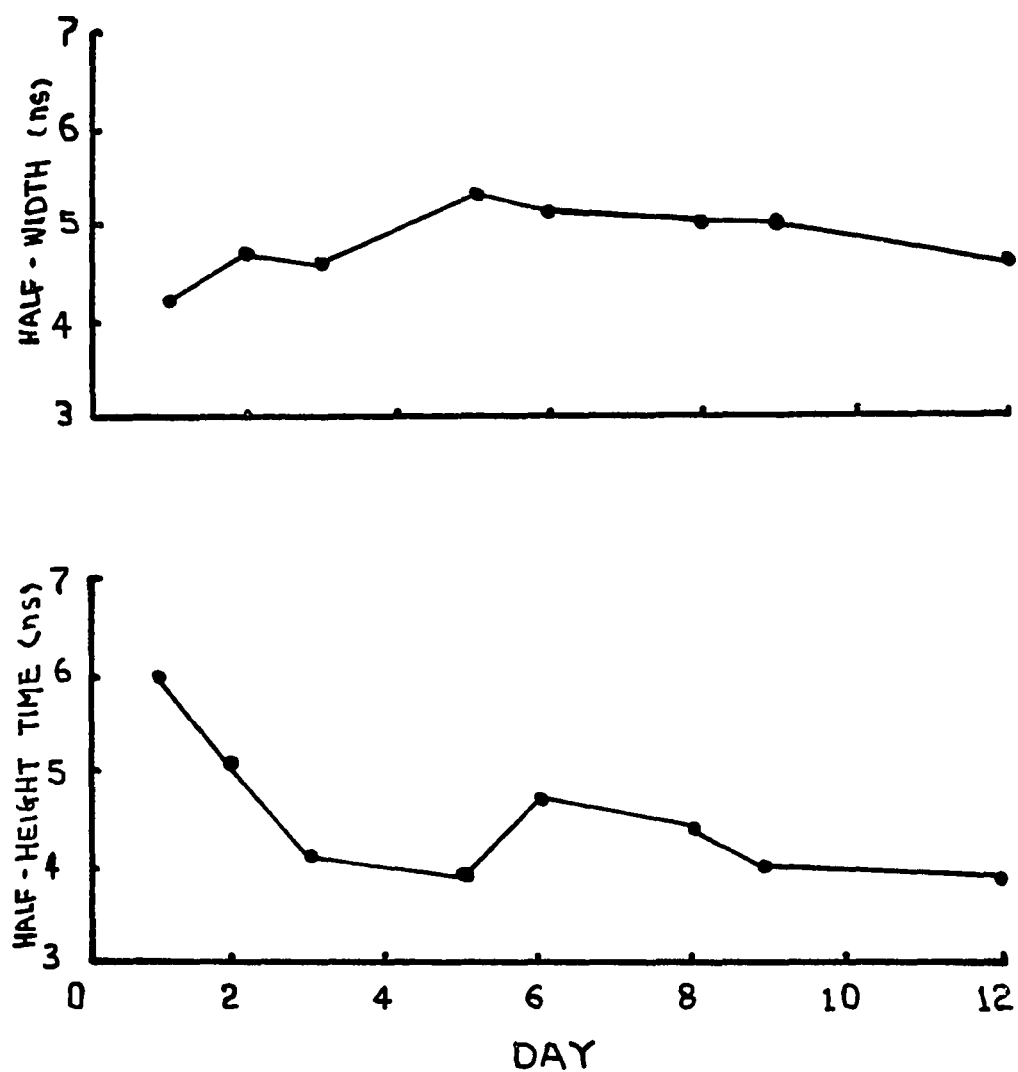


Figure 38 Plot of the half-widths and half-height times of the laser profiles as a function of days of operation.

The testing started with a simulation of the laser profile of approximate shape and half-width. The function,

$$f(t) = \alpha t^2 \text{EXP}(-0.6t),$$

was chosen. The convolution was generated by this simulated profile with various A's and B's. After the fluorescence profile had been shifted 0.3 ns to the right, both the shifted fluorescence profile and the unshifted laser profile were fed into the simplex program for calculating A's and B's. The results of such trials of the selected extreme values of A's and B's are shown in Table XIX. The errors of this source can be as large as 30% when values of A and B, similar to the case of nitrogen plus 5% oxygen, are large.

Large errors for large values of A and B are intuitively logical. Large values of A and B mean short decay times. Given an instrument, it is harder to measure a short decay than a long decay. If we take a simple view that the reciprocal of A is the lifetime, when A is  $6 \times 10^{10} \text{ sec}^{-1}$ , the lifetime is about 0.17 ns, as compared to a laser half width of 7 ns, and a potential timing uncertainty of 0.3 ns!



TABLE XIX  
ESTIMATION OF THE ERRORS DUE TO -0.3  
ns SHIFT OF THE LASER PROFILE SIMULATION

	True Value	Simplex Value	Percent Error
A	6.0	7.81	+30.2%
B	0.6	0.723	+20.5%
A	0.2	0.208	+4.0%
B	0.02	0.0198	+1.0%

## CHAPTER VI

### DISCUSSION

#### Limits on A and B

How large can the values of A and B be before our method ceases to provide answers with acceptable uncertainty? The limits on A and B are controlled by factors such as the resolution of the MCA, the jitters of the start pulse and other uncertainty factors discussed in Chapter V. We will look at the effects of the laser half-width on the limits on A and B.

The manifestation of reaching the limits of A and B is that beyond certain values of A and B, a large change in the values of A and B does not produce a significant change in the errors of the least squares fit. Thus, there is large uncertainty associated with the values of A and B, because the simplex may result in a wide range of values.

In general, for narrower laser half-width, larger A and B can be resolved. This is because with a narrow laser half-width, comparatively large A and B can still produce an output function that differs significantly from the input function. This effect can be illustrated with our experimental results of OH in nitrogen.

In the early experiments, when the dye laser was

tuned by a diffraction grating, the laser half-width was about 7 ns. With 7 ns half-width, we resolved the fluorescence of OH in nitrogen successfully. However, when the tuning mechanism was changed to a mirror to increase output power, the laser half-width was broadened to about 10 ns and the laser profile looked like two peaks overlapping each other with their peak maxima separated by about 5 ns (see Figure 39). Since then, we could not evaluate A and B from the fluorescence in nitrogen. The results are shown in Figure 39.

Actually, the experiments of OH fluorescence in  $N_2/2\% O_2$  and  $N_2/5\% O_2$  had already been close to the limits of our instrument even with 7 ns laser half-width. This is evident from the error bars associated with each result shown in Figure 25. With a laser half-width of 10 ns, such large values of A and B make the deconvolution impossible.

#### Photolytic Interference

Photolytic interference is caused by the generation of OH radicals by the laser. This, in effect, changes the OH concentration within the duration of the laser pulse and perturbs the linear system assumption.

To study the photolytic effects of ozone is a major project in its own right. We will touch upon the problem but will not provide a detailed solution to the problem. Essentially, we will show that the high values of the rate constants by oxygen are not due to ozone interference.

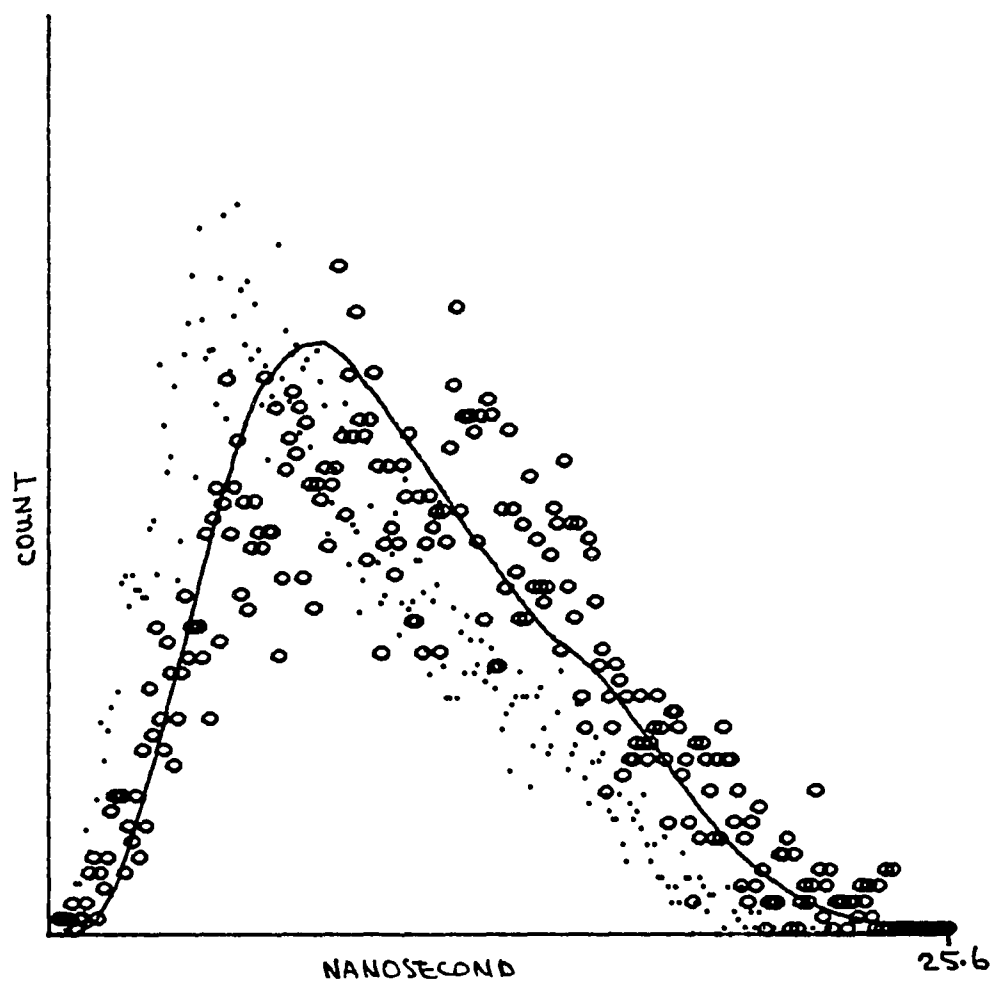
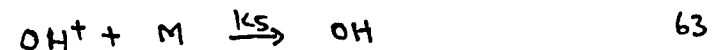
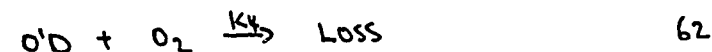
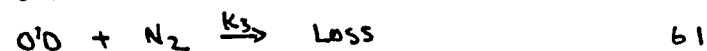
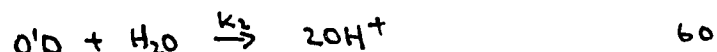
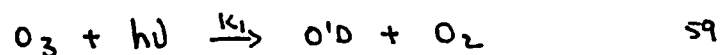


Figure 39 Fluorescence of OH in nitrogen due to the excitation by a 10 ns half-width laser. o - fluorescence, . - laser, solid line - least squares fit.

Photolytic interference by ozone is due to the photodecomposition of ozone into oxygen and  $O^1D$ . The  $O^1D$  subsequently reacts with water to produce rotationally excited OH ( $OH^+$ ), which eventually cascades down to the ground state. In effect, this increases the OH concentration within the duration of the excitation laser pulse.

The processes can be represented by the following equations:



We can write the rates of change of  $O^1D$  and  $[OH^+]$  as:

$$\frac{d[O^1D]}{dt} = -[O^1D](K_1[H_2O] + K_3[N_2] + K_4[O_2]) \quad 64$$

$$\frac{d[OH^+]}{dt} = 2[O^1D][H_2O]K_2 - K_5[OH^+][M] \quad 65$$

In equation 64 we assume that there is an initial concentration of  $O^1D$  ( $[O^1D]_0$ ) just as we assume that there is an initial concentration  $[OH^+]_0$  in Chapter II. Later, we can replace the  $[O^1D]_0$  with a time dependent input function related to the laser profile. If we solve

equations 64 and 65, we will obtain an double exponential decay as in the case of  $[\text{OH}^*]$  cascading into  $[\text{OH}^{**}]$ . The relaxation of  $\text{OH}^\dagger$  into  $\text{OH}$  is one more step that modifies the double exponential decay a bit. Then we can use the laser as an input function and the modified response function to find out how the concentration of the spurious  $\text{OH}$  changes as a function time. One complication is that we have to know the absolute concentration of the ozone, the laser intensity and the quantum yield of  $\text{O}^1\text{D}$  at 282 nm in order to assess the final effect on the fluorescence decay curve. In general, this spurious  $\text{OH}$  will distort the true fluorescence curve. Figure 40 shows an approximate spurious fluorescence curve as compared to the true fluorescence.

Another photolytic source is two-photon photolysis of  $\text{H}_2\text{O}(22)$ . The two-photon dissociation process was minimized by keeping the laser energy low and the beam diameter large (about 0.3 cm). Still another source of spurious  $\text{OH}$  is by photolysis of  $\text{H}_2\text{O}_2$  generated by the reaction of  $\text{OH}+\text{OH}$ . Since its absorption has not quite tailed out near 280 nm,  $\text{H}_2\text{O}_2$  still can be photolysed by the laser. But notice that the detection zone is always illuminated by the mercury lamps. Any  $\text{H}_2\text{O}_2$  will be quickly photolysed by the lamps. Under experimental conditions, production of  $\text{H}_2\text{O}_2$  is not favored. Hence, photolysis of  $\text{H}_2\text{O}_2$  by the laser to  $\text{OH}$  is minimized.

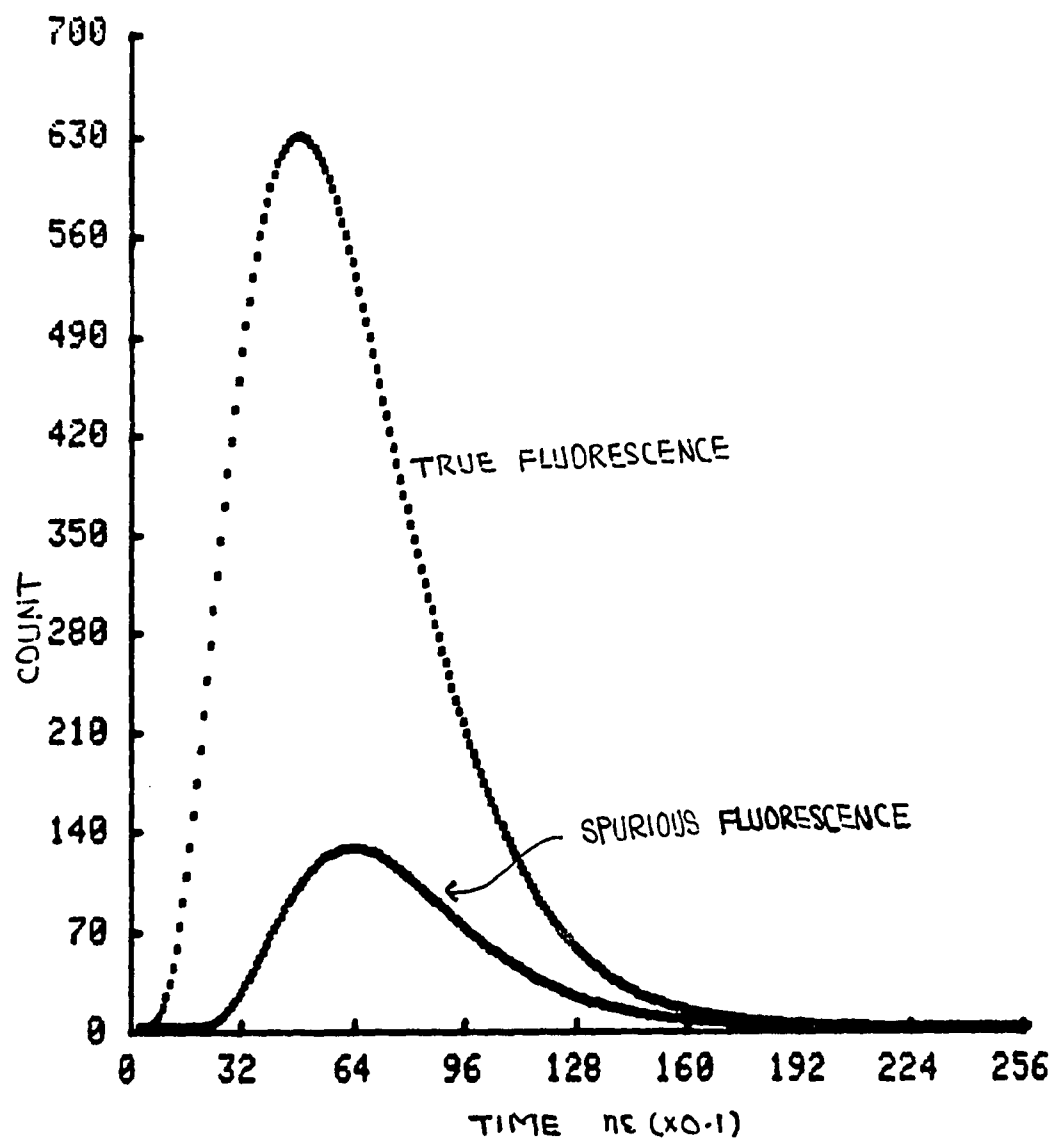


Figure 40 Time dependency of spurious OH fluorescence signal as compared to the true fluorescence signal.

The effects of spurious fluorescence on the true fluorescence were checked with simulations. Spurious fluorescence of various amplitudes was added to the simulated fluorescence curves and these corrupted fluorescence curves were analyzed for A and B by the simplex program. The results are shown in Table XX. The results show that the spurious fluorescence can only reduce the values of A and B and therefore cannot explain the high results.

#### Improvement

The biggest problem is the long term drift of the detection system described in Chapter V. An immediate improvement is to use a laser with higher repetition rate. High repetition rate shortens the experimental time which minimizes the drift due to the change in room temperature or the drift of the instruments. A high repetition rate also makes a larger count feasible. This again decreases the errors. One suitable candidate is the XeBr laser.

The other timing errors can be reduced by a fast and less temperature sensitive photodiode. Enclosing the photodiode in a constant temperature oven is another approach to the temperature problem. A shorter rise time definitely reduces the time jitter. A Laser with narrower pulse width will also allow larger values of A and B to be measured.

Another improvement that can be made is to use two



TABLE XX  
EFFECTS OF OZONE INTERFERENCE ON  
THE VALUES OF A AND B

Amplitude*	A	B
0	2.0	0.40
0.1	1.59	0.384
0.2	1.27	0.380
0.3	1.01	0.389
0.4	0.82	0.41
0.5	0.89	0.37

\* Amplitude refers to the ratio of the peak height of the spurious signal to the true fluorescence signal.

detection systems. One detector monitors the laser scattering while the other measures the fluorescence. This will minimize the effects due to the change of the laser profile.

#### Effects of The New Rate Constants

What are the effects of the new rate constants on the reported ambient OH concentration? According to equation 52, the integrated fluorescence intensity at 309 nm is inversely proportional to the product of A and B and directly proportional to  $k'_{10}$ . We will consider the correction by the rate constant of water alone and by all measured rate constants. For comparison, the rate constants recommended by Scholfield will be used. We will assume  $k_{10H_2O}$  to be  $1 \times 10^{-9}$  cm molecule<sup>-1</sup>sec<sup>-1</sup>, since it is quoted as "fast".

For the case of the rate constant of water alone, it results in an 32.5% increase in the reported values. For the case of all the rate constants, it results in and 31.2% increase. In essence, our experimental results agree with the reported OH measurements within the instrumental uncertainty.

## REFERENCES

- 1 R.K. Lengel and D.R. Crosley, J. Chem. Phys. 64, 3900 (1976).
- 2 J.A. Coxon, Can. J. Phys. 58, 933 (1980).
- 3 T. Carrington, J. Chem. Phys. 41, 2021 (1964).
- 4 V.N. Kondrat'ev, Chem. Kinetics of Gas Reaction (Pergamon Press Inc., N.Y. 1964).
- 5 B.G. Bunnett and F.W. Dalby, J. Chem. Phys. 40, 1414 (1964).
- 6 H.P. Hooymayers and C.Th.J. Alkemade, J. Quant. Spectry. Radiative Transfer 7, 495 (1967).
- 7 C.C. Wang, L.I. Davis Jr., C.H. Wu, S. Japar N. Niki and B. Weinstock, Science 189, 797 (1975).
- 8 D.D. Davis, W. Heaps and T. McGee, Geophys. Res. Lett. 3, 331 (1976).
- 9 P.J. Crutzen and J. Fishman, Geophys. Res. Lett 4, 321 (1977).
- 10 H. Levy, Science 173, 141 (1971).
- 11 S.C. Wofsy, J.C. McConnel and M.B. McElroy, J. Geophys. Res. 77, 4477 (1972).
- 12 W.L. Chameides and J.C.G. Walker, J. Geophys. Res. 78, 8751 (1973).

- 13 J.A. Logan, M.J. Prather, S.C. Wofsy and M.B. McElroy,  
J. Geophys. Res. 86, 7210 (1981).
- 14 J.G. Anderson, Geophys. Res. Lett. 3, 165 (1976).
- 15 C.R. Burnett, Geophys. Res. Lett. 3, 319 (1976).
- 16 D. Perner, D.H. Ehhalt, H.W. Patz, U. Platt, E.P. Roth  
and A. Volz, Geophys. Res. Lett. 3, 466 (1976).
- 17 M.J. Campbell, J.C. Sheppard and A.F. Au, Geophys.  
Res. Lett. 3, 175 (1979).
- 18 E.L. Baardsen and R.W. Terhune, Appl. Phys. Lett.  
21, 209 (1972).
- 19 C.C. Wang, L.I. Davis Jr., P.M. Selzer and R. Munoz,  
J. Geophys. Res. 86, 1181 (1981).
- 20 D.D. Davis, W.S. Heaps, D. Philen, M. Rodgers, T. McGee,  
A. Nelson and A.J. Moriarty, Rev. Sci. Instrum.  
50, 1505 (1979).
- 21 M. Rokni, J.H. Jacob, J.A. Mangano and R. Brochu,  
Appl. Phys. Lett. 31, 79 (1977).
- 22 C.C. Wang and L.I. Davis Jr., J. Chem. Phys. 62, 53  
(1975).
- 23 P.M. Selzer and C.C. Wang, J. Chem. Phys. 71, 3786  
(1979).
- 24 K. Schofield, J. Phys. Chem. Ref. Data 8, 763 (1979).
- 25 J. Yguerabide, Methods of Enzymology XXVI, 498 (1972).
- 26 V.J. Koester and R.M. Dowden, Rev. Sci. Instrum.  
49, 1186 (1978).

- 27 C.C. Davis and T.A. King, Rev. Sci. Instrum. 41, 407 (1970).
- 28 C.C. Davis and T.A. King, J. Phys. A3, 101 (1970).
- 29 D.E. Donohue and R.C. Stern, Rev. Sci. Instrum. 43, 791 (1972).
- 30 P.B. Coates, J. Phys. E1, 878 (1968).
- 31 D.A. Gedcke and W.J. McDonald, Nucl. Instrum. Methods 58, 253 (1968).
- 32 ORTEC Model 270 Constant Fraction Timing Photomultiplier Base Operating Manuel.
- 33 K.R. German, J. Chem. Phys. 64, 4065 (1976).
- 34 Z. Bay, Phys. Rev. 77, 419 (1950).
- 35 Z. Bay, V.P. Heuri and H. Kanner, Phys. Rev. 100, 1197 (1955).
- 36 W.P. Helman, Inst. J. Radiat. Phys. Chem. 3, 283 (1971).
- 37 I. Isenberg and R.D. Dyson, Biophys. J. 9, 1337 (1969).
- 38 R. Schuyler and I. Isenberg, Rev. Sci. Instrum. 42, 813 (1971).
- 39 K.H. Becker, D. Haaks, Z. Naturforsch 28a, 249 (1973).
- 40 D. Kley and K.H. Welge, J. Chem. Phys. 49, 2870 (1968).
- 41 M.A.A. Clyne and S. Down, JCS Faraday Trans. II 70, 253 (1974).

- 42 M.Kaneko, Y. Mori and I. Tanaka, J. Chem. Phys. 48, 4468 (1968).
- 43 P. Hogan and D.D. Davis, J. Chem. Phys. 64, 3901 (1976).
- 44 R.K. Lengel and D.R. Crosley, Chem. Phys. Lett. 32, 261 (1975).
- 45 J.A. Nelder and R. Mead, The Computer J. 5, 308 (1965).
- 46 L.C.W. Dixon, Nonlinear Optimisation (Crane, Russak and Co. Inc., N.Y. 1972).
- 47 R.K. Lengel and D.R. Crosley, J. Chem. Phys. 68, 5309 (1978).

## APPENDICES

## APPENDIX A

### SIMPLEX SEARCH

The current accepted Simplex optimization technique is that due to Nelder and Mead(45). The following is mostly based on Dixon(46).

A simplex consists of a pattern of at least  $n+1$  points enclosing a non-zero volume in  $n$  dimensional space. The simplex search is now commonly used for minimizing a mathematical function of several variables. In our case, this function will be the variance or the standard deviation.

Let  $n+1$  points of the simplex be denoted by  $x^i$ ,  $i=1,\dots,n+1$ . The initial simplex is normally formed by making an estimate  $x^1$  and then taking a step along each axis  $e^i$ ,  $i=1,\dots,n$  so that

$$x^{1+i} = k x^i \quad A1$$

for some selected values of  $k$ . In this program,  $k$  is 0.5. The function values (standard deviations),  $f_i$ ,  $i=1,\dots,n$ , of each point  $x^i$  are calculated. The values  $f_i$  are sorted into

$$f(x^h) = \text{maximum } f_i, \quad A2$$



$$f(x^g) = \text{second maximum } f_i, \quad A3$$

$$f(x^l) = \text{minimum } f_i. \quad A4$$

Of the points of the simplex,  $x^h$  now has the worst function value. It is therefore the point to be replaced.

To determine the new point, the centroid  $x^c$  of the remaining points is calculated:

$$x^c = ((\sum_{i=1}^{n+1} x^i) - x^h) / n. \quad A5$$

Then the reflection point of  $x^h$  about the centroid,

$$x^r = 2x^c - x^h \quad A6$$

and its function value  $f(x^r)$  are calculated. Then this function value is checked for improvement. If we have

$$f(x^r) \geq f(x^h) \quad A7$$

too large a step has been taken, and a contraction,  $x^n$ , is made according to the definition:

$$x^n = 0.3 x^h + 0.7 x^c. \quad A8$$

If the  $x^r$  is an improvement based on the criterion:

$$4f(x^r) - f(x^h) < f(x^l), \quad A9$$

then there is a possibility that a larger step in the same direction may be beneficial, i.e.

$$x^e = 4x^r - 3x^c. \quad A10$$

If the extension is successful, i.e.

$$f(x^e) \leq f(x^r), \quad A11$$

then we replace the  $x^h$  by  $x^e$ . If  $x^e$  is not successful, then we replace  $x^h$  by  $x^r$ .

If the contraction results in

$$f(x^n) \geq f(x^h) \quad A12$$

then a massive contraction is made on the simplex by

$$x^i = (2x^i + x^l)/3. \quad A13$$

The process is terminated as soon as

$$\sum_{i=1}^{n+1} (f(x^i) - f(x^l))^2 < \epsilon \quad A14$$

where  $\epsilon$  is some preset small number called the convergence factor.

The above description is intended to introduce the terminology used in the flow chart (Figure 41). For the details on the iteration procedure, please consult the

flow chart in Figure 41. A FORTRAN program of the flow chart can be found in Table XXI. Any ventures into the forbidden values by the program e.g. negative A and B are discouraged by returning an artificially large function value.

The biggest defect of the simplex method is that sometimes it does not converge on the true minimum but terminates itself in local minimum.

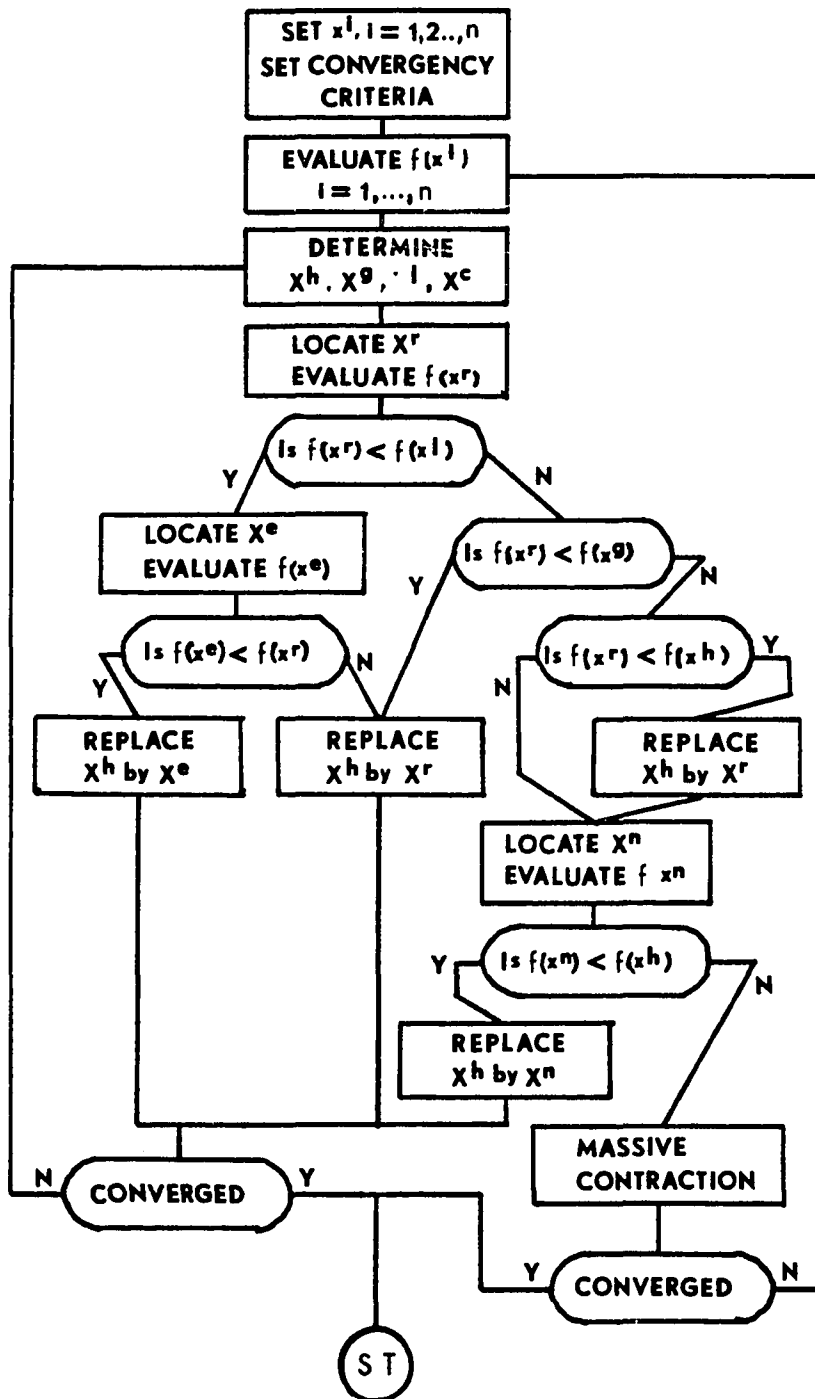


Figure 41 Flow chart of the simplex iteration procedure.

TABLE XXI

## SIMPLEX PROGRAM WITH THE CONVOLUTION SUBROUTINE

```

C N IS THE NUMBER OF VARIABLES TO BE SOUGHT.
C N+3 IN THIS CASE. Y8 IS THE RETURNED
C FUNCTION VALUE TO BE MINIMIZED
10 IMPLICIT REAL (A-Z)
20 INTEGER I,J,K,K1,K2,K3,J1,L1,N
25 N=3
30 DIMENSION V(N),H(256),L(256),D(256),D1(256)
35 DIMENSION B(N,N+2),C(N),R(N),Y9(N+2)
C TRIAL COUNT
40 L1=0
C READ DATA FROM PERMANENT FILES TO MATRICES D AND D1
50 K=0
60 DO 35 I=1,64
70 K1=K+1
80 K2=K1+1
90 K3=K2+1
100 K=K3+1
110 READ (22,33)D(K1),D(K2),D(K3),D(K)
120 READ (23,33)D1(K1),D1(K2),D1(K3),D1(K)
130 35 CONTINUE
140 33 FORMAT(F8.3,10X,F8.3,10X,F8.3,10X,F8.3)
C CONVERGENCE FACTOR
150 CF=1.0E-5
C STARTING VARIABLES GUESSES, CHANGE ACCORDING TO N
160 B(1,1)=40
170 B(2,1)=.18
180 B(3,1)=1.3
C CALCULATE THE OTHER VERTICES, 0.5 OF ORIGINAL VALUES
190 DO 1 I=2,N+1
200 DO 2 J=1,N
210 IF(I-1.EQ.J) GOTO 100
220 B(J,I)=B(J,1)
230 GOTO 2
240 100 B(J,I)=0.5*B(J,1)
250 2 CONTINUE
260 1 CONTINUE
270 50 DO 3 I=1,N+1
280 DO 4 J=1,N
290 4 V(J)=B(J,I)
300 CALL CALC (Y8,V,D,L,H,D1,L1)
310 Y9(I)=SQRT(Y8)
320 3 CONTINUE
C SORTING, B(X,1) IS THE SET (X) WITH LARGEST VARIANCE
330 60 DO 5 I=1,N
340 DO 6 J=I+1,N+1
350 IF (Y9(I)-Y9(J).GT.0) GOTO 6
360 Y9(N+2)=Y9(J)
370 Y9(J)=Y9(I)
380 Y9(I)=Y9(N+2)
390 DO 7 K=1,N
400 B(K,N+2)=B(K,J)
410 B(K,J)=B(K,I)
420 7 B(K,I)=B(K,N+2)
430 6 CONTINUE
440 5 CONTINUE
C CALCULATE THE CENTROID
450 DO 8 I=1,N
460 C(I)=0
470 DO 9 J=1,N+1
480 9 C(I)=C(I)+B(I,J)
490 C(I)=(C(I)-B(I,1))/N
500 8 CONTINUE
C CALCULATE THE REFLECTION POINT
510 DO 10 I=1,N
520 10 R(I)=2*C(I)-B(I,1)
C CALCULATE THE VARIANCE OF THE REFLECTION POINT
530 DO 11 I=1,N
540 11 V(I)=R(I)
550 CALL CALC (Y8,V,D,L,H,D1,L1)
560 PRINT, 'NUMBER OF TRIALS:', ' ',L1
570 PRINT, 'LEAST VARIANCE:', ' ',Y9(4)
580 PRINT, 'VARIABLE 1','VARIABLE 2','VARIABLE 3'
590 PRINT, B(1,4),B(2,4),B(3,4)
600 PRINT, 'CONVERGENT FACTOR',' ',T
610 PRINT, '****'
620 R1=SQRT(Y8)

```

## TABLE XXI CONTINUED

```

C IMPROVEMENT CHECK
625 Y=4*R1-Y9(1)
630 IF (Y.LT.Y9(N+1)) GOTO 22
C
640 IF (R1.LT.Y9(2)) GOTO 20
C
650 IF (R1.GT.Y9(1)) GOTO 13
660 DO 12 I=1,N
670 12 B(I,1)=R(I)
680 Y9(1)=R1
C NO IMPROVEMENT; CONTRACTION
690 13 DO 14 I=1,N
700 14 V(I)=0.3*B(I,1)+0.7*C(I)
710 CALL CALC (Y8,V,D,L,H,D1,L1)
720 C1=SQRT(Y8)
C
730 IF (C1.LT.Y9(1)) GOTO 18
C NO IMPROVEMENT, EVEN AFTER CONTRACTION; MASSIVE CONTRACTION
740 DO 15 I=1,N+1
750 DO 16 J=1,N
760 16 B(J,I)=(2*B(J,I)+B(J,N+1))/3
770 15 CONTINUE
C CHECK FOR CONVERGENCE
780 T=0
790 DO 17 I=1,N
800 17 T=T+(Y9(I)-Y9(N+1))**2
810 T=T/N
820 IF (T.LT.CF) GOTO 80
830 GOTO 50
C IMPROVEMENT MADE, REPLACE
840 18 DO 19 I=1,N
850 19 B(I,1)=V(I)
860 Y9(1)=C1
870 GOTO 70
C IMPROVEMENT MADE, BETTER THAN THE NEXT WORST, REPLACE
880 20 DO 21 I=1,N
890 21 B(I,1)=R(I)
900 Y9(1)=R1
905 GOTO 70
C IMPROVEMENT OF REFLECTION, EXTENSION
910 22 DO 23 I=1,N
920 23 V(I)=4*R(I)-3*C(I)
930 CALL CALC (Y8,V,D,L,H,D1,L1)
940 E1=SQRT(Y8)
C
950 IF (E1.LT.R1) GOTO 26
C NO IMPROVEMENT, REPLACE THE REFLECTION POINT
960 DO 25 I=1,N
970 25 B(I,1)=R(I)
980 Y9(1)=R1
990 GOTO 70
C IMPROVEMENT ON EXTENSION, REPLACEMENT
1000 26 DO 27 I=1,N
1010 27 B(I,1)=V(I)
1020 Y9(1)=E1
C CONVERGENCE CHECK
1030 70 T=0
1040 DO 28 I=1,N
1050 28 T=T+(Y9(I)-Y9(N+1))**2
1060 T=T/N
1070 IF (T.GT.CF) GOTO 60
C CONVERGENCE FOUND, PRINT RESULTS
1080 80 PRINT, 'CONVERGENCE HAS BEEN OBTAINED'
C CAHNGE ACCORDINGLY
1090 DO 29 I=1,N
110 PRINT, 'V1', 'V2', 'V3'
1110 PRINT, B(1,I),B(2,I),B(3,I)
1120 29 CONTINUE
1130 PRINT, 'CENTROID', 'BEST ESTIMATE'
1140 PRINT, 'VARIABLE', 'VARIABLE 2', 'VARIABLE 3'
1150 PRINT, C(1),C(2),C(3)
1160 PRINT, 'LEAST VARIANCES:',Y9(N+1)
1180 STOP
1190 END

```

## TABLE XXI CONTINUED

```

1200 SUBROUTINE CALC (Y8,V,D,L,H,D1,L1,Y9)
1210 IMPLICIT REAL (A-Z)
1220 INTEGER K1,J1,K2,L1
1230 DIMENSION V(3),D(256),D1(256),L(256),H(256)
1240 L1=L1+1
C CHANGE ACCORDINGLY
1250 A=V(1)
1260 B=V(2)
1270 C=V(3)
1271 IF(A.LT.0)GOTO 26 83
1272 IF(B.LT.0)GOTO 26 83
1273 IF(C.LT.0) GOTO 26 83
1310 DO 2445 K1=1,256
1320 H(K1)=0
1330 2445 CONTINUE
1340 DO 2530 K1=1,256
1350 J1=K1-1
1360 A1=J1*A*0.1
1370 B1=J1*B*0.1
1380 IF(A1.GT.60) GO TO 2500
1390 IF(B1.GT.60) GO TO 2520
1400 L(K1)=EXP(-A1)-EXP(-B1)
1410 GO TO 2530
1420 2500 IF (B1.GT.60) GOTO 2510
1430 L(K1)=-EXP(-B1)
1440 GO TO 2530
1450 2510 L(K1)=0
1460 GOTO 2530
1470 2520 L(K1)=EXP(-A1)
1480 2530 CONTINUE
1490 R1=1/(B-A)
1500 DO 2600 K1=1,256
1510 Q1=D(K1)*R1
1520 K2=1-K1
1530 DO 2600 J1=K1,256
1540 H(J1)=H(J1)+Q1*L(J1+K2)
1550 2600 CONTINUE
1560 DO 2640 K1=1,256
1570 H(K1)=H(K1)*C
1580 2640 CONTINUE
1590 Y8=0
1600 DO 2680 K1=1,256
1610 2618 Y8=Y8+(H(K1)-D1(K1))**2
1620 2680 CONTINUE
1622 GOTO 120
1623 26 83 Y8=Y9*2
1630 120 RETURN
1640 END
$:EXECUTE
$:LIMITS:10,,,3K
$:PRMFL:23,R,S,RCHMS001/AR90N
$:PRMFL:22,R,S,RCHMS001/SCACS
$:ENDJOB

```

## APPENDIX B

### AIM-65 TO LeCroy 3001QVT MCA INTERFACE

The interface adaptor allows the AIM-65 microcomputer to communicate with the LeCroy 3001QVT MCA. It enables the memory contents of the MCA to be read by the AIM-65. The microcomputer can also alter the memory of the MCA. It also provides controls such as start, stop and clear.

Figure 42 gives the schematics of the interface adaptor. The adaptor essentially provides a 16 bit bidirectional buffer for data transfers between the MCA and the microcomputer. It also has a 10 bit address counter and various one-shots to provide different addresses of the MCA memory and controls.

The adaptor communicates with the microcomputer through two VIA's(6522). The 16 bit data are transmitted through the 16 I/O pins (PA0 to PA7 and PB0 to PB7). Table XXII summarizes the logic sequences to execute the desired commands. This logic is implemented by the assembly codes shown in Table XXIII. The commands are structured so that each command becomes a BASIC multi-statement. Table XXIV lists the BASIC statements that execute the desired operations. Finally, Table XXV shows the locations of the microcomputer memory containing the contents of the MCA.



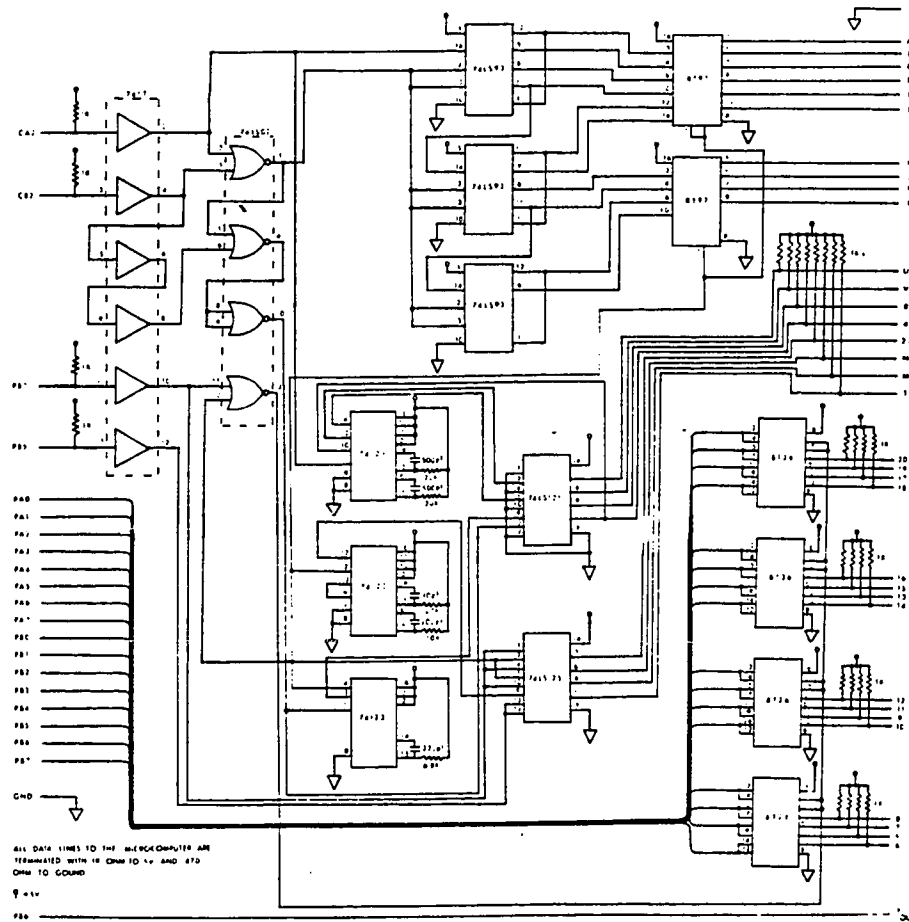


Figure 42 Schematics of the MCA to AIM-65 interface adaptor. Labels on the left side of the figure refer to the VIA on the AIM-65. Labels on the right refer to the rear connector of the MCA.

TABLE XXII  
LOGIC SEQUENCES FOR EXECUTING COMMANDS TO  
CONTROL THE MCA THROUGH THE INTERFACE  
ADAPTOR BY THE AIM-65

To Clear the MVA - Clear 1: write zeros.  
Clear 2: bring PB5 low for 100 ms.

To clear address counter - Bring CA2 and CB2 low.

To advance address - Bring CB2 high and toggle CA2 (4 low's for quadrant mode).

To read - Set PB7 high and toggle CB2 once to read one channel.  
Read I/O ports when CB2 is low.

To write - Set PB7 low and toggle CB2 one to write one channel.  
Always return PB7 high after writing. Set up output data before bringing CB2 low.

To count pulse - Set T2 to count pulse from PB6 (BUSY from the MCA).

To stop MCA - Advance one address when CA2 is low.

To start MCA - Set PB7 high and bring CB2 low once.

```

5290 A9 LDA #A0
5292 8D STA 9802
5295 A9 LDA #80
5297 8D STA 9800
529A A0 LDY #21
529C A2 LDX #E0
529E CA DEX
529F D0 BNE 529E
52A1 88 DEY
52A2 F0 BEQ 52A7
52A4 4C JMP 529C
52A7 A9 LDA #A0
52A9 8D STA 9800
52AC 60 RTS

```

TABLE XXIII CONTINUED

## Write

```

50CD 20 JSR 50D0
50D0 A9 LDA #FF
50D2 8D STA 9002
50D5 8D STA 9003
50D8 8D STA 9000
50DB 8D STA 9001
50DE A9 LDA #A0
50E0 8D STA 9800
50E3 8D STA 9802
50E6 20 JSR 5000
50E9 A9 LDA #EE
50EB 8D STA 900C
50EE A9 LDA #58
50F0 8D STA 4003
50F3 A9 LDA #59
50F5 8D STA 4004
50F8 AD LDA 4001
50FB F0 BEQ 5102
50FD A9 LDA #04
50FF 8D STA 4002
5102 AD LDA 0000
5105 48 PHA
5106 AD LDA 0001
5109 48 PHA
510A AD LDA 0002
510D 48 PHA
510E AD LDA 0003
5111 48 PHA
5112 A9 LDA #00
5114 8D STA 0000
5117 8D STA 0002
511A A0 LDY #00
511C AD LDA 4003
511F 8D STA 0001
5122 AD LDA 4004
5125 8D STA 0003
5128 B1 LDA (00),Y
512A 49 EOR #FF
512C 8D STA 9001
512F B1 LDA (02),Y
5131 49 EOR #FF
5133 8D STA 9000
5136 A9 LDA #20
5138 8D STA 9800
513B A9 LDA #CE
513D 8D STA 900C

```

```

5140 A9 LDA #EE
5142 8D STA 900C
5145 A9 LDA #A0
5147 8D STA 9800
514A 20 JSR 5006
514D C8 INY
514E D0 BNE 5128
5150 AD LDA 4001
5153 F0 BEQ 5169
5155 CE DEC 4002
5158 F0 BEQ 5169
515A EE INC 4003
515D EE INC 4003
5160 EE INC 4004
5163 EE INC 4004
5166 4C JMP 511A
5169 68 PLA
516A 8D STA 0003
516D 68 PLA
516E 8D STA 0002
5171 68 PLA
5172 8D STA 0001
5175 68 PLA
5176 8D STA 0000
5179 60 RTS

```

## Clear 1

```

517D 20 JSR 5180
5180 A9 LDA #FF
5182 8D STA 9002
5185 8D STA 9003
5188 8D STA 9000
518B 8D STA 9001
518E A9 LDA #A0
5190 8D STA 9802
5193 8D STA 9800
5196 20 JSR 5000
5199 A9 LDA #EE
519B 8D STA 900C
519E A9 LDA #58
51A0 8D STA 4003
51A3 A9 LDA #59
51A5 8D STA 4004
51A8 AD LDA 4001

```

```

51AB F0 BEQ 51B2
51AD A9 LDA #04
51AF 8D STA 4002
51B2 AD LDA 0000
51B5 48 PHA
51B6 AD LDA 0001
51B9 48 PHA
51BA AD LDA 0002
51BD 48 PHA
51BE AD LDA 0003
51C1 48 PHA
51C2 A9 LDA #00
51C4 8D STA 0000
51C7 8D STA 0002
51CA A0 LDY #00
51CC AD LDA 4003
51CF 8D STA 0001
51D2 AD LDA 4004
51D5 8D STA 0003
51D8 A9 LDA #20
51DA 8D STA 9800
51DD A9 LDA #CE
51DF 8D STA 900C
51E2 A9 LDA #EE
51E4 8D STA 900C
51E7 A9 LDA #A0
51E9 8D STA 9800
51EC 20 JSR 5006
51EF C8 INY
51F0 D0 BNE 51D8
51F2 AD LDA 4001
51F5 F0 BEQ 520B
51F7 CE DEC 4002
51FA F0 BEQ 520B
51FC EE INC 4003
51FF EE INC 4003
5202 EE INC 4004
5205 EE INC 4004
5208 4C JMP 51CA
520B 68 PLA
520C 8D STA 0003
520F 68 PLA
5210 8D STA 0002
5213 68 PLA
5214 8D STA 0001
5217 68 PLA
5218 8D STA 0000
521B 60 RTS

```

TABLE XXIII CONTINUED

5270	A9	LDA	#EC	Stop
5272	8D	STA	900C	
5275	4C	JMP	527D	
5278	A9	LDA	#CE	Start
527A	8D	STA	900C	
527D	A9	LDA	#EE	
527F	8D	STA	900C	
5282	60	RTS		

TABLE XXIV  
COMMANDS FOR CONTROLLING THE MCA  
IN BASIC STATEMENTS

```
READ:
    POKE4,37 : POKE5,80 : X=USR(W)

WRITE:
    POKE4,205 : POKE5,80 : X=USR(W)

START:
    POKE4,120 : POKE5,82 : X=USR(W)

STOP:
    POKE4,112 : POKE5,82 : X=USR(W)

CLEAR 1:
    POKE4,125 : POKE5,81 : X=USR(W)

CLEAR 2:
    POKE4,144 : POKE5,82 : X=USR(W)

COUNT WX PULSES:
    INPUT WX
    POKE4,48 : POKE5,82 : X=USR(WX)
    ( To check if the WX pulses have already in:
      Y=PEEK(16389)
      IF Y 0 THEN ..."count is up")

POKE16385,0 = QUADRANT MODE
POKE16385,1 = 1 K MODE
```

TABLE XXV  
MEMORY MAP OF THE COPIED MCA CONTENTS

QUADRANT MODE

MCA	Addresses in AIM-65
Channel 1	22784(H.8 bits);22528(L.8 bits)
Channel 2	22785(H.8 bits);22529(L.8 bits)
.	.
.	.
Channel 256	23039(H.8 bits);27783(L.8 bits)

1 K MODE

MCA	Addresses in AIM-65
Channel 1	22784(H.8 bits);22528(L.8 bits)
Channel 2	22785(H.8 bits);22529(L.8 bits)
.	.
.	.
Channel 256	23039(H.8 bits);22783(L.8 bits)
Channel 257	23296(H.8 bits);23040(L.8 bits)
.	.
.	.
Channel 512	23551(H.8 bits);23295(L.8 bits)
Channel 513	23808(H.8 bits);23552(L.8 bits)
.	.
.	.
Channel 1024	24875(H.8 bits);24139(L.8 bits)

## APPENDIX C

### LASER POWER MONITOR

The laser power monitor provides a means of monitoring the energy of each individual laser pulse. It is composed of two main parts: a vacuum photodiode and a peak detector. Figure 43 illustrates the organization of the monitor. Figure 44 is a schematic of the peak detector.

A portion of the UV laser pulse illuminates the vacuum photodiode and produces an electrical pulse. The peak detector captures the peak voltage from the vacuum photodiode and the analog-to-digital converter (A/D) digitizes the captured peak voltage. The digitized voltage can be acquired by the AIM-65 microcomputer. The same analog peak voltage from the peak detector is sent to a LED bar graph (NSM 3914) for visual display. The LED display provides visual feedback for tuning the laser for optimum energy output.

The peak detector automatically updates its digital output whenever a new laser pulse is detected. Its EOC output goes high to indicate that a new conversion has been completed. Its input TRI-STATE has to be held high before the valid data are presented at the data pins. Clock rate of the A/D is one MHz. Conversion time is about 100



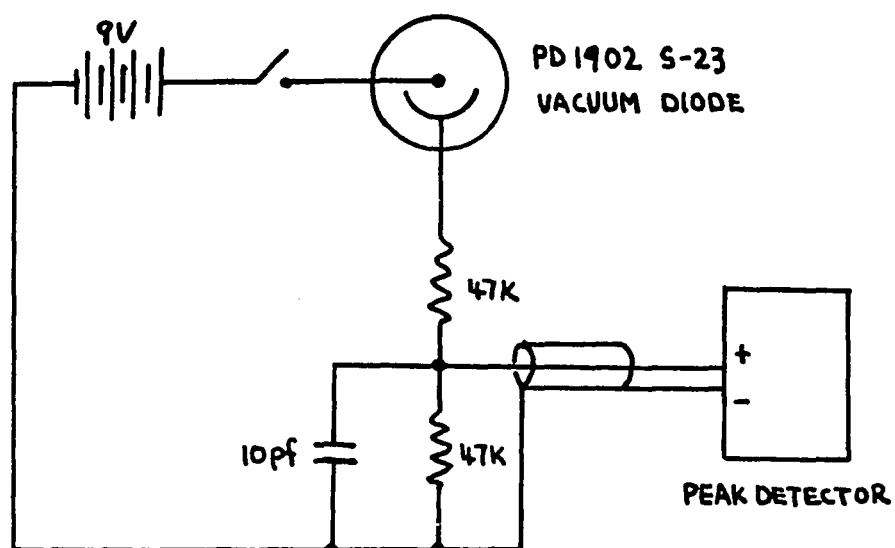


Figure 43 Laser power monitor. Details of the peak detector is shown in Figure 37.

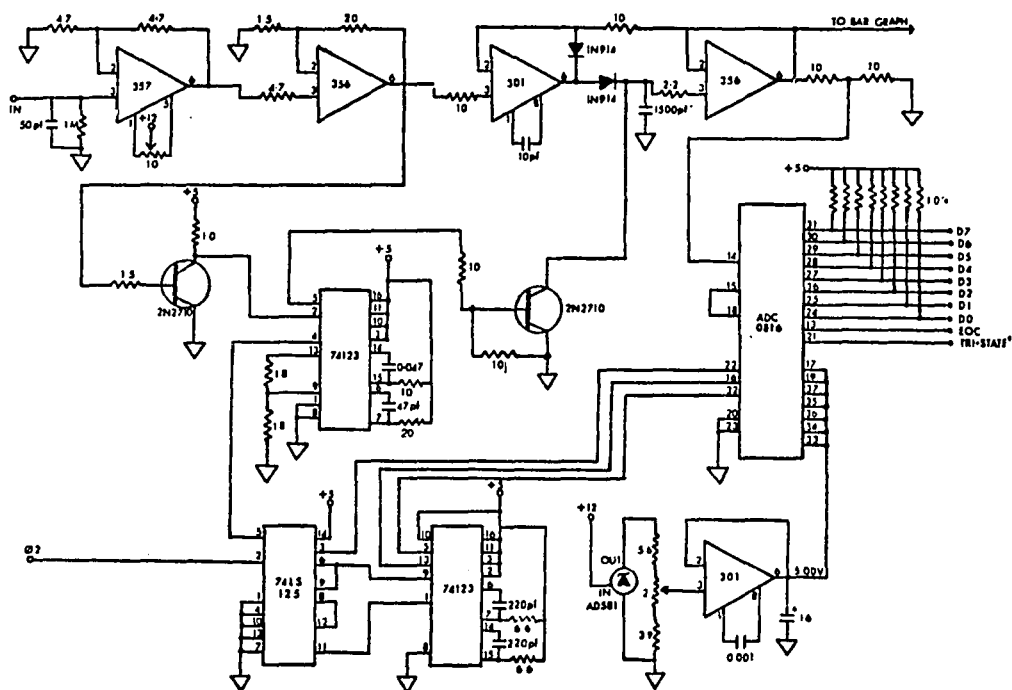


Figure 44 Schematics of the peak detector.  $\phi 2$  refers to the master clock of the AIM-65. All resistors are in K-ohm except as indicated. All capacitors are in microfarad except as indicated (\*-silver mica).  $V_{CC}$  and  $V_{EE}$  of all operational amplifiers are connected to  $+12V$  and  $-12V$ .

microseconds. The AIM-65 communicates with the peak detector through the EOC which is connected to the CA1 and the TRI-STATE which is connected to the CA2. The 8 bit A/D output takes up a portion of the unused I/O pins of the two VIA's on the DRAM expansion board. The peak detector can be used concurrently with the MCA interface adaptor.

The program listed in Table XXVI allows the integrated photomultiplier current (Q-mode) obtained by the MCA to be normalized against the laser power. The program duplicates the contents of the MCA onto the (HEX)5800 and (HEX)5900 blocks of memory. 5800(L.B.) and 5900(H.B.) correspond to the first channel of the MCA. When a laser pulse is detected, the BUSY output from the MCA decrements a count of the T2 of the VIA through the PB6 pin and at the same time interrupts the microcomputer through the CBI pin. The interrupt service program compares the duplicate and the new contents of the MCA channel by channel until a mismatch is located. A count is then added to the mismatched channel to update the duplicate. The mismatched channel number is then stored together with the laser power from the peak detector. The channel numbers and the peak detector outputs are stored in memory locations from (HEX)6400 upward. For example, location 6400 contains the peak detector output and 6401 contains the corresponding channel number. The purpose of this program is that when the MCA is used in Q-mode, the

TABLE XXVI  
ASSEMBLY CODES FOR THE LASER POWER MONITOR  
AND THE MCA

52FF A2 LDX #10	5370 8D STA 9808
5301 8D LDA 0000,X	5373 AD LDA 00AC
5304 43 PHA	5376 8D STA 9809
5305 A9 LDA #00	5379 A9 LDA #80
5307 9D STA 0000,X	537B 8D STA 9800
530A E3 INX	537E A0 LDY #20
530B E0 CPX #1A	5380 A2 LDX #E0
530D D0 BNE 5301	5382 CA DEX
530F A9 LDA #00	5383 D0 BNE 5382
5311 8D STA 9002	5385 88 DEY
5314 8D STA 9003	5386 F0 BEQ 538B
5317 8D STA 9803	5388 4C JMP 5380
531A 8D STA 4006	538B A9 LDA #A0
531D A9 LDA #A0	538D 8D STA 9800
531F 8D STA 9802	5390 A9 LDA #CE
5322 8D STA 9800	5392 8D STA 900C
5325 A9 LDA #EE	5395 A9 LDA #EE
5327 8D STA 900C	5397 8D STA 900C
532A A9 LDA #58	539A A9 LDA #0C
532C 8D STA 0011	539C 8D STA 980C
532F A9 LDA #59	539F A0 LDY #00
5331 8D STA 0013	53A1 98 TYA
5334 A9 LDA #62	53A2 91 STA (10),Y
5336 8D STA 0015	53A4 91 STA (12),Y
5339 A9 LDA #63	53A6 C8 INY
533B 8D STA 0017	53A7 D0 BNE 53A2
533E A9 LDA #64	53A9 58 CLI
5340 8D STA 0019	53AA AD LDA 4000
5343 A9 LDA #7F	53AD F0 BEQ 53AA
5345 8D STA 980E	53AF A9 LDA #7F
5348 8D STA 980D	53B1 8D STA 980E
534B A9 LDA #B0	53B4 AD LDA 0019
534D 8D STA 980E	53B7 AC LDY 4006
5350 A9 LDA #00	53BA 20 JSR 00D1
5352 8D STA 4000	53BD A2 LDX #19
5355 AD LDA 980B	53BF 68 PLA
5358 29 AND #DF	53C0 9D STA 0000,X
535A 18 CLC	53C3 CA DEX
535B 69 ADC #20	53C4 E0 CPX #10
535D 8D STA 980B	53C6 D0 BNE 53BF
5360 A9 LDA #D0	53C8 68 PLA
5362 8D STA A400	53C9 8D STA 0010
5365 A9 LDA #53	53CC 60 RTS
5367 8D STA A401	
536A 20 JSR BEFE	
536D AD LDA 00AD	

TABLE XXVI CONTINUED

53D0 43 PHA	5420 8D STA 900C	5479 AD LDA 980D
53D1 8A TXA	5423 A9 LDA #EC	547C 29 AND #02
53D2 48 PHA	5425 8D STA 900C	547E F0 BEQ 547A
53D3 98 TYA	5428 A9 LDA #EE	5480 A9 LDA #0E
53D4 48 PHA	542A 8D STA 900C	5482 8D STA 980C
53D5 A9 LDA #EC	542D A9 LDA #EC	5485 AD LDA 9801
53D7 8D STA 900C	542F 3D STA 900C	5488 91 STA (18),Y
53DA AD LDA 980D	5432 A9 LDA #EE	548A A9 LDA #0C
53DD 29 AND #20	5434 8D STA 900C	548C 8D STA 980C
53DF F0 BEQ 53EC	5437 A9 LDA #EC	548F EE INC 4006
53E1 A9 LDA #20	5439 8D STA 900C	5492 D0 BNE 544E
53E3 8D STA 980D	543C A9 LDA #EE	5494 EE INC 0019
53E6 EE INC 4006	543E 8D STA 900C	5497 4C JMP 544E
53E9 4C JMP 54A1	5441 A9 LDA #EC	549A A9 LDA #FF
53EC A9 LDA #CC	5443 8D STA 900C	549C 91 STA (18),Y
53EE 8D STA 900C	5446 A9 LDA #EE	549E 4C JMP 548F
53F1 A0 LDY #14	5448 8D STA 900C	54A1 63 PLA
53F3 A9 LDA #EE	544E C3 INY	54A2 A3 TAY
53F5 8D STA 900C	544C D0 ENJ 5407	54A3 63 PLA
53F8 A2 LDX #50	544E A9 LDA #10	54A4 AA TAX
53FA A9 LDA #EC	5450 3D STA 980D	54A5 63 PLA
53FC 8D STA 900C	5453 A9 LDA #CE	54A6 40 RTI
53FF A9 LDA #EE	5455 8D STA 900C	
5401 3D STA 900C	5458 A9 LDA #EE	
5404 CA DEX	545A 8D STA 900C	
5405 D0 BNE 53FA	545D 4C JMP 54A1	
5407 A9 LDA #CE	5460 B1 LDA (10),Y	
5409 8D STA 900C	5462 18 CLC	
540C AD LDA 900C	5463 69 ADC #01	
540F 49 EOR #FF	5465 91 STA (10),Y	
5411 D1 CMP (12),Y	5467 B1 LDA (12),Y	
5413 D0 BNE 5460	5469 69 ADC #00	
5415 AD LDA 9001	546B 91 STA (12),Y	
5418 49 EOR #FF	546D 98 TYA	
541A D1 CMP (10),Y	546E AC LDY 4006	
541C D0 BNE 5460	5471 91 STA (13),Y	
541E A9 LDA #EE	5473 EE INC 4006	
	5476 AC LDY 4006	

channel number is proportional to the integrated photomultiplier current. Thus the program keeps a record of the integrated current and its corresponding laser power. This record can be used to normalize the detected fluorescence intensity.

The program only works when the MCA is in quadrant mode. Whenever a laser pulse is fired, but its power is not high enough to trigger the peak detector, (HEX)FF will be stored as the laser power next to the channel number. In most cases, the channel corresponding to zero photomultiplier current is not the first channel of the MCA. This zero channel have to be set at the program location (53F3). For the listed program, content of memory location 53F3 is (HEX)14 which indicates that channel 20 is the zero channel. The memory location at 53F9 has also be changed to 4 times that of 53F3 i.e. (HEX)50 in this case.

The program operates on base of a predetermined number of laser pulses. The program can be called up by the BASIC multi-statement:

```
POKE4,255:POKE5,82:X=USR(W)
```

The variable W is the number of laser pulses to be recorded. Variable X is the address (in decimal) of the top of the recorded channel-laser power pairs. Once the machine program is invoked, program execution will continue in the machine program until the count is up. Any

disruptions of the machine program will cause the zero  
page registers of the BASIC interpreter to be destroyed.  
The consequence is disastrous!